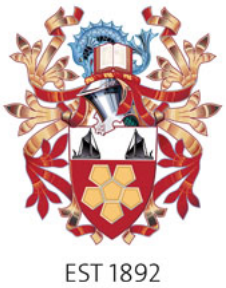

London South Bank University

Microwave Imaging for Diagnostic Application

by

Banafsheh Khalesi

A thesis submitted in partial fulfilment of the requirements of London South Bank University for the degree of Doctor of Philosophy

School of Engineering
Division of Electrical Electronic Engineering
London South Bank University
London, United Kingdom

Supervisor: Prof. Mohammad Ghavami

September 2020

Abstract

Imaging of the human body makes a significant contribution to the diagnosis and succeeding treatment of diseases. Among the numerous medical imaging methods, microwave imaging (MWI) is an attractive approach for medical applications due to its high potential to produce images of the human body safely with cost-efficiency.

A wide range of studies and research has been done with the aim of using the microwave approach for medical applications.

The focus of this research is developing MWI algorithms, which is the Huygens Principle (HP) based and to validate the capability of the proposed MWI algorithm to detect skin cancer and bone lesion through phantom measurements.

The probability of the HP procedure for skin cancer detection has been investigated through design, and fabrication of a heterogeneous phantom simulating the human forearm having an inclusion mimicking a skin cancer. Ultrawideband (UWB) MWI methods are then applied to the phantom. The S21 parameter measurements are collected in an anechoic chamber environment and processed via HP technique. The tumour is successfully detected after applying appropriate artefact removal procedure.

The ability to successfully apply HP to detect and locate a skin cancer type inclusion in a multilayer cylindrical phantom has been verified.

The feasibility study of HP-based MWI procedure for bone lesion detection has also been investigated using a dedicated phantom. Validation has been completed through measurements inside the anechoic chamber in the frequency range of 1–3 GHz using one receiving and one transmitting antennas in free space. The identification of the lesion's presence in different bone layers has been performed on images. The quantification of the obtained images has been performed by introducing parameters such as the resolution and signal-to-clutter ratio (S/C). The impact of different frequencies and bandwidths (in the 1–3 GHz range) in lesion detection has been investigated. The findings showed that the frequency range of 1.5–2.5 GHz offered the best resolution (1.1 cm) and S/C (2.22 on a linear scale). Subtraction between S21 obtained using two slightly displaced transmitting positions has been employed to remove the artefacts; the best artefact removal has been obtained when the spatial displacement was approximately of the same magnitude as the dimension of the lesion.

Subsequently, a phantom validation of a low complexity MWI device (based on HP) operating in free space in the 1-6.5 GHz frequency band using two antennas in free space has been applied. Detection has been achieved in both bone fracture lesion and bone marrow lesion scenarios using superimposition of five doublet transmitting positions after applying the rotation subtraction method to remove artefact. A resolution of 5 mm and the S/C (3.35 in linear scale) are achieved which is clearly confirming the advantage of employing multiple transmitting positions on increased detection capability.

The finding of this research verifies the dedicated MWI device as a simple, safe and without any X-ray radiation, portable, and low complexity method, which is capable of been successfully used for bone lesion detection.

The outcomes of this thesis may pave the way for the construction of a dedicated bone imaging system that in future could be used as a safe diagnostic device even in emergency sites.

Acknowledgements

Undertaking this PhD has been a truly life-changing experience for me and it would not have been possible to do without the support and guidance that I received from many people. I am very grateful for the chance that was given to me to do my PhD studies at the BIMEC group of LSBU. I wish to acknowledge everyone whose help, support, and guidance over the years has been instrumental in the completion of this dissertation.

First and foremost, I would like to express my sincere gratitude to my principal supervisor, Prof. Mohammad Ghavami for his guidance, feedback and encouragement throughout my research. His constant support helped me significantly in my PhD journey.

I would like to express my deepest appreciation to my committee technical supervisor, Dr. Gianluigi Tiberi for his patience, encouragement, motivation and for the immense knowledge that he has imparted throughout this project. This work would not have been possible without his guidance and persistent help. His continued mentoring and invaluable advice, on both research and thesis, over the years has allowed me to learn the necessary skills to become a better research scientist. I believe that my success in the research and the completion of my dissertation would not have been practicable without the support and nurturing of Dr. Gianluigi Tiberi.

I'm deeply indebted to Dr. Navid Ghavami for his guidance, feedback, and constant support through this project and thesis.

I would also like to extend my deepest gratitude to Prof. Sandra Dudley for her advice and also for her technical support. I wish to express my special appreciation for Dr. Perry Xiao for providing the permittivity measurements device which greatly assisted the fabrication of the artificial phantoms for my research.

I am also grateful to my friends, co-workers, and office-mates, Behnaz Sohani, Bilal Khalid, Mahreen Riaz, Robert Brown , and James Puttock that made life at the university as good as it could be.

Last but not least, I would also like to say a heartfelt thank you to my parents and my sisters for always believing in me and encouraging me to follow my dreams, and a very special thank you to my lovely husband for helping in whatever way they could during this challenging period.

- Financial support

I gratefully acknowledge the financial supports received towards my PhD from UBT Company. I greatly appreciate the support I received from the collaborative work I undertook with the UBT team.

Publications

- **Banafsheh Khalesi**, Behnaz Sohani, Navid Ghavami, Mohammad Ghavami, Sandra Dudley, and Gianluigi Tiberi, "A Phantom Investigation to Quantify Huygens Principle Based Microwave Imaging for Bone Lesion Detection." *Electronics*, 8, no. 12 (2019): 1505.

- Behnaz Sohani, **Banafsheh Khalesi** , Navid Ghavami, Mohammad Ghavami, Sandra Dudley, Amir Rahmani, and Gianluigi Tiberi. "Detection of haemorrhagic stroke in simulation and realistic 3-D human head phantom using microwave imaging." *Biomedical Signal Processing and Control*, 61 (2020): 102001.

- **Banafsheh Khalesi** , Gianluigi Tiberi, Navid Ghavami, Mohammad Ghavami, and Sandra Dudley, "Skin cancer detection through microwaves: Validation on phantom measurements." In *2018 IEEE International Conference on Imaging Systems and Techniques (IST)*, pp. 1-6. IEEE, 2018.

- Gianluigi Tiberi, **Banafsheh Khalesi** , Behnaz Sohani, Sandra Dudley, Mohammad Ghavami, and Navid Ghavami, "Phase-weighted UWB Imaging through Huygens Principle." In *2019 PhotonIcs & Electromagnetics Research Symposium-Spring (PIERS-Spring)*, pp. 949-952. IEEE, 2019.

- **Banafsheh Khalesi**, Behnaz Sohani, Navid Ghavami, Mohammad Ghavami, Sandra Dudley, and Gianluigi Tiberi, "Free space operating microwave imaging device for bone lesion detection: a phantom investigation." *IEEE Antenna and wireless Propagation letters.*

- James Puttoc, Behnaz Sohani, **Banafsheh Khalesi**, Gianluigi Tiberi, Mohammad Ghavami, "UWB Microwave Imaging for Stroke Detection: Methodology for Comparing Artefact Removal Algorithms", EAI BODYNETS 2020 (2020).

- Behnaz Sohani, James Puttock, **Banafsheh Khalesi**, Navid Ghavami, Mohammad Ghavami, Sandra Dudley and Gianluigi Tiberi. "Developing Artefact Removal Algorithms to Process Data from a Dedicated Microwave Medical Imaging Device allowing Stroke Detection." *Sensors* 20, no. 19 (2020): 5545.

List of Abbreviation

2D	Two-Dimensional
3D	Three-Dimensional
ABS	Acrylonitrile Butadiene Styrene
ACS	American Cancer Society
BCC	Basal Cell Carcinoma
CT	Computed Tomography
MI	Medical Imaging
MRI	Magnetic Resonance Imaging
MWI	Microwave Imaging
OUT	Object Under test
ROI	Region of Interest
SC	Stratum Corneum
SCC	Squamous Cell Carcinoma
S/C	Signal to Clutter Ratio
UWB	Ultra-Wideband
VNA	Vector Network Analyser
WHO	World Health Organization

List of Symbols

ε_r	Dielectric constant
σ	Conductivity
f	Frequency
I	Intensity
N_{PT}	Number of observation points
Δs	Spatial sampling
k_1	Wave number
G	Greens' function
λ	Wavelength
tx	Transmitting antenna
rx	Receiving antenna

List of Figures

List of Tables

Contents

Chapter 1

Introduction

The theoretical background and the underlying impetus of Microwave imaging (MWI) system is demonstrated in this chapter.

1.1 Background and Research Motivation

Medical imaging (MI) plays an important role in the diagnosis and treatment of various diseases. MI techniques provide a visual representation of the interior of a body for clinical analysis, which can assist the diagnosis and treatment of patients. Monitoring the treatment process and tracking any ongoing issues is the other benefit of using MI.

There are many different types of MI techniques. The most common MI applications are ultrasound imaging, X-ray screening, magnetic resonance imaging (MRI) scanning, computed tomography (CT) scans, which can create a detailed image of the inside of the body.

Although, the current MI techniques can generate the images with high resolution and accuracy, however, each technique suffers from its negative aspect and its limitation. For instance, these are expensive medical equipment and they are not available in all hospitals. According to the World Health Organization (WHO) more than half of the population in the world does not have access to diagnostic imaging [1]. Time–consuming, using ionising radiation, and uncomfortable examination procedure are other major shortcomings that limit the use of these techniques.

The limitations of the current imaging techniques, motivate researchers to find a low–cost, safe, accurate, and cost-effective/efficient imaging system that can be used as an alternative technique for detecting various of diseases. Among the various diseases, cancer is one of the serious problems that threaten human life. The high percentage of annual mortality rate caused by cancer shows the importance of developing MI techniques to detect cancer at an early stage.

For instance, lung cancer leads to more than one million annually of death in the

world [2]. Breast cancer is also the most common type of cancer in the world that needs to be diagnosed in the early stages to increase the chance of successful treatment.

Therefore, there is a lack of reliable screening tools for early-stage detection of such diseases. Furthermore, current imaging techniques such as X-rays and CT involve ionized radiations, which cannot be used for frequent screenings particularly for infants and pregnant patients. Moreover, techniques also are not suitable for some diseases that need regular monitoring such as acute lung injuries, lung cancer [3].

In addition, the existing imaging methods are not helpful in emergency sites where the fast diagnosis is critical to save the life of patients. For instance, in the case of brain injuries that might be caused by a fall, a road accident, and stroke, fast diagnosis is essential because millions of brain cells die every second after the onset of symptoms [4]. In the case of stroke, which is the third common cause of death, also fast diagnosis is urgent. The ischemic and haemorrhagic are two main types of stroke that despite having the same symptoms, their treatment is quite different. Now, CT and MRI are the best imaging technique that helps the doctors for the distinction between ischemic and haemorrhagic. Since in the event of such injuries, the clinical decision should be made within 3 hours of the onset of symptoms, so, a fast and portable diagnosis system is demanded.

Bone fracture is a medical condition that can occur in any part of the bone in the body. Nearly 16 million fractures cases have reported in the United States every year, which is the result of accidents or bone weakness [5]. X-ray is the fastest method for detecting bone fracture; however, using ionizing radiation is the main concern in the frequent use of this method particularly at the stages of pregnancy and infants. Moreover, the X-ray is not able to detect the fracture in some cases (such as wrist fractures, hip fractures). Besides this, the X-ray cannot give enough information about muscle, tendons, or joints [6]. In contrast, CT and MRI can identify the damaged tissues surrounding the bone fracture. However, the ionising radiation of CT and the high cost of purchasing and maintaining the MRI device cause the restrictions of using these methods. In addition, some cases of bone fracture required emergency treatment since the delay in the fracture repair might lead to occur infection.

Accordingly, achieving alternative MI manner that can be used as a reliable, safe, inexpensive, portable, and accurate technique is the priority.

1.2 Microwave Medical Imaging

In recent years, there has been a wide range of efforts to develop MI techniques using Ultra-Wideband (UWB) [7], [8]. Using MWI technique in medical applications has been known as a promising method that has the potential to produce images in a low cost and safe manner and is suitable for diagnosis and monitoring of the treatment. Specifically,

MWI techniques has become a very great approach for early-stage cancer detection.

The significant difference in dielectric properties between healthy tissue and unhealthy tissue at microwave frequencies is the basis of microwave MI. In fact, this difference can be used as an indicator for microwave MI [9]. These properties comprise relative permittivity and electrical conductivity.

For instance, the malignant tissue has high permittivity and conductivity values in comparison with the healthy surrounding tissues. This considerable difference in dielectric properties between healthy and unhealthy tissues caused the contrast in the images and lead to rapidly identify the disease. Fig. 1.1 shows an example of the contrast between dielectric properties of healthy tissue and cancerous tissue in the case of breast cancer [9]. Moreover, it is clear from Fig. 1.1(a) that the malignance tissue (presenting in the black line) has a highest values of permittivity compare to the fat tissue, muscle, and fibro glandular. Fig. 1.1(b) shows the same behaviour for the conductivity.

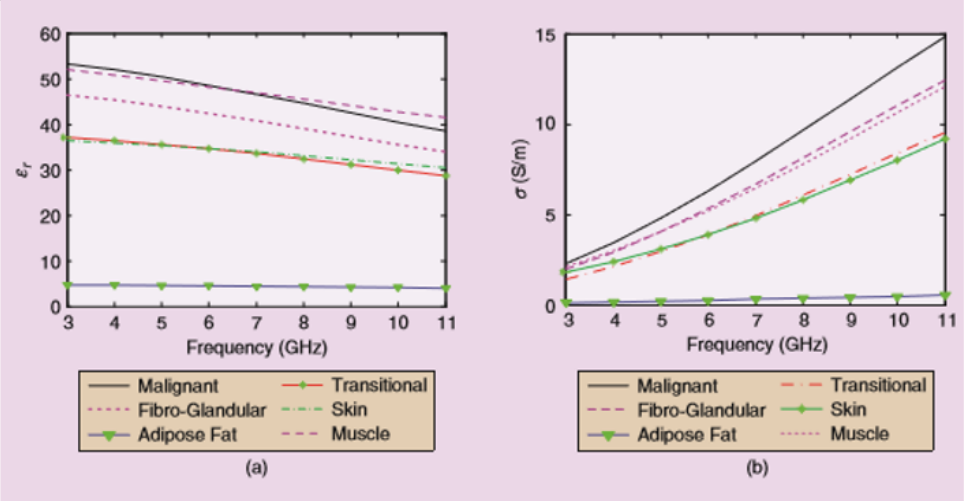

Figure 1.1: Dielectric properties of various breast tissues.

There is also a significant difference between dielectric properties of healthy tissues and bleeding tissues which lead to contrast in the microwave medical images [10]. Fig. 1.2 shows the dielectric properties of bleeding tissue in injured human head and it confirms that the bleeding tissue has the highest values of permittivity and conductivity in comparison to the other normal tissues.

When human tissues are exposed to an electromagnetic wave at microwave frequency, the behaviour of the unhealthy tissue leads to reflection back of a high portion of electromagnetic wave to the source. The reflected signals indicate the discovering of location or/and dielectric properties of abnormality tissues. For this purpose, a MWI system is required for sending the eclectromagnetic wave to the imaged object and receiving the reflection signal from the target.

In recent years, a wide range of studies has been performed with the aim of devel-

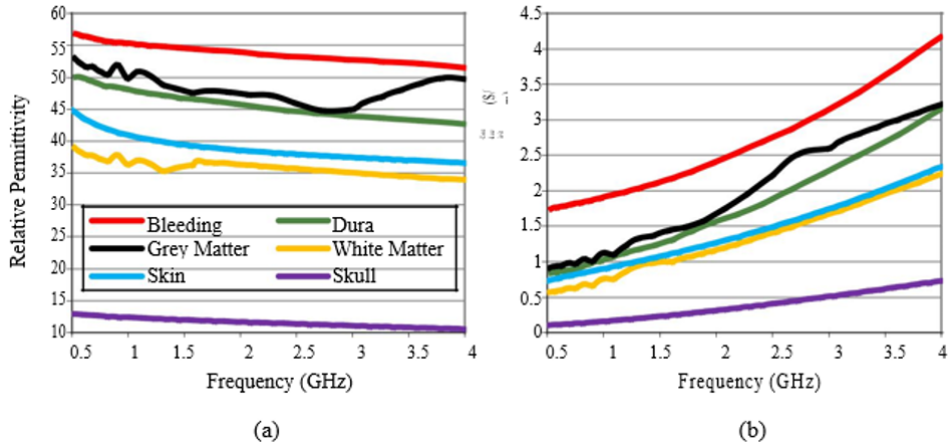

Figure 1.2: Dielectric properties of human head.

oping the MWI system for medical applications including breast imaging [11, 12] brain stroke detection [13–15], and bone fracture imaging [16, 17]. Although, in the past few years, successful studies have been performed in term of design and construction for MWI medical applications particularly for breast cancer detection, however, achieving a safe, simple, and portable microwave MI device is still challenging. In addition, since the imaging algorithm has an important role in capability of the MWI system, so, achieving a fast and accurate MWI algorithm suitable for medical application is another challenge.

This research focuses on the optimization of MWI algorithms for medical applications. In this work, the investigation of the capability of MWI algorithm for skin cancer detection and bone lesion detection will be performed.

1.3 Aim of this Thesis

This work focuses on investigating the possibility of a proposed MWI technique based on the HP for skin cancer and bone lesion detection. Design and fabrication suitable phantoms for microwave experiments is another part of this research. The validation of the proposed MWI algorithm is performed through phantom measurements inside an anechoic chamber and also using a dedicated MWI device.

1.4 Original Contribution

1- Design and fabrication complex phantoms simulating human forearm and human bone layers through the following steps:

- Discovering the appropriate material to mimic different layers of human forearm and bone layers having similarity in dielectric properties with human tissue and suitable

for performing microwave experiments.

- Designing and modelling the multilayer phantoms emulating human forearm and bone lesion appropriate for investigating skin cancer and bone lesion detection.
- Finding out the applicable container in terms of shape and size to keep the similarity in geometric characteristics with the human forearm.
- Construction and preparation of the forearm and bone lesion phantoms suitable for microwave measurement setup.

2- Improving the proposed MWI system to provide a more accurate measurement procedure.

- Designing and constructing the graded phantom holder with the aim of increasing the accuracy of the measurement process.

3- Development of MWI algorithm suitable for skin cancer detection, bone lesion detection including:

- Improving the MWI algorithm to perform proper artefact removal procedure.
- Improving the MWI algorithm to quantify the obtained microwave images.

4- Investigation of the capability of the proposed MWI method to detect skin cancer and bone lesion using phantom measurements.

1.5 Thesis Structure

This thesis is organized into 7 main chapters as follows:

- Chapter 1:
  Covers a brief summary of the research background and motivations, microwave MI, the aim of the research, and original contributions.
- Chapter 2:
  Deals with the literature review. This chapter discusses the current MI systems, their limitation, and restrictions. The basis of the MWI technique, the different MWI approaches, the physical principle governing MWI, the historical view of developing the MWI techniques for breast cancer, skin cancer, and bone imaging, have been discussed in this chapter.

- Chapter 3:
  Presents the block diagram of the proposed frequency domain MWI system, introducing the proposed methodology and MWI algorithm based on the HP. Additionally, chapter 3 explains the experimental setup and measurement equipment and validates the proposed methodology through phantom measurements in the anechoic chamber to illustrate the capability of the proposed MWI technique to detect the presence and location of lesion inside the imaged objects. Moreover, this chapter demonstrates the dedicated MammoWave MWI device, performing the validation of the dedicated device through phantom measurements to detect the presence of lesion inside the objects.

- Chapter 4:
  Presents the investigation of the possibility of the MWI technique for skin cancer detection. Design and fabrication of multilayer human forearm phantom considering the appropriate recipe, performing MWI experimental setup and phantom measurements, applying imaging algorithm to process the data, employing artifact removal technique, generating microwave images, and conclusion are reported in this chapter.

- Chapter 5:
  Exhibits the possibility of the MWI technique for bone lesion detection. Design and fabricating multilayer human bone phantoms, performing experiments setup and phantom measurements in the anechoic chamber, employing MWI algorithm to remove the artefact and generating the microwave images, analysing the obtained images, investigating the impact of different frequencies and different bandwidths in removing the artefact, discussion and conclusion are all indicated in chapter 5.

- Chapter 6:
  Demonstrates the capability of the MammoWave device for bone lesion detection. Introducing the new MWI device, improving the prefabricated bone lesion phantom to be more realistic, performing phantom measurements, applying MWI algorithm to generate the microwave images, performing the image quantification, comparing the obtained results using MWI device with the obtained results in the anechoic chamber, discussion, and conclusion have been presented in this chapter.

- Chapter 7:
  The conclusion of this research has been provided in this chapter. In addition, promising suggestions and recommendations have been addressed in the future work section.

Chapter 2

Literature Review

2.1 Introduction

This chapter includes the overview of the current imaging techniques for biomedical applications is provided. The limitations of each technique are presented. The fundamental principles of the MWI technique are explained, followed by a review of various studies on the dielectric properties of breast tissues. Additionally, the historical evolution of MWI technology and the challenges of existing MWI systems are discussed.

2.2 Current Imaging Diagnostic techniques

In recent decades, the development of imaging techniques has received significant attention, particularly in medical applications. Currently, different MI technologies are used to produce well-defined images of organs or tissues inside the body. Ultrasound, X-ray based Computed tomography (CT), and magnetic resonance imaging (MRI) are the most commonly used clinical diagnostic method in medical examinations. The overview of the performance, merit, and shortcomings of the mentioned methods and their drawbacks are explained as follows:

2.2.1 The Ultrasound Scanner

Ultrasound imaging system (Fig. 2.1) [18] is a safe screening tool which uses the innocuous wave frequency range, from 1 MHz to 15 MHz to determine whether the area under consideration consists of normal or abnormal tissue. Ultrasound is a very cost-effective imaging technique, however, it suffers from contrast problems and inability to image objects with large acoustic impedance differences such as air spaces and bones [19, 20]. This medical technique is popular to use in the case of frequently screening such as monitoring pregnancy and also in tumour detection [21].

Figure 2.1: Ultrasound device.

2.2.2 X-ray Based Computed Tomography

This MI technique uses X-rays as the examination wave to pass through the tissues and makes the distinction between different anatomical structures (see Fig. 2.2). This technique is able to produce the image of high-contrast subjects with excellent quality. However, the high levels of ionizing radiation in this technique are harmful to patients [22, 23]. CT is able to provide high-resolution images from any part of the body to identify the presence of a tumour. For breast cancer, CT provides accurate information about the presence, size, and location of the tumour.

Figure 2.2: X-ray computed tomography device.

For breast cancer, CT provides accurate information about the presence, size, and location of the tumour. This type of MI technique is also able to identify abnormalities in

the brain. In fact, CT is an essential tool for assessing brain stroke disease, particularly at the emergency site. However, the large amount of ionizing radiation used in CT scan is the main concern in the case of frequent use [24].

2.2.3 Magnetic Resonance Imaging

MRI (Fig. 2.3), is a very valuable medical diagnostic technique that is able to provide more details than CT scan [18]. This device is able to produce high resolution images to identify the presence of a very small tumour. Furthermore, in the case of brain injuries, MRI is an effective method to distinguish between ischaemic and haemorrhagic strokes, exceptionally in emergencies. Nevertheless, the high cost of purchase and maintaining the device, and the time-consuming are the main drawbacks of this imaging method [25].

Figure 2.3: Magnetic resonance imaging device.

As aforementioned, the major problems of current diagnosis methods can be classified as safety, cost, and accuracy. The restrictions of the current MI techniques have motivated research to develop the more effective, non- ionizing, and low-cost diagnosis approach for cancer detection.

2.3 Microwave Imaging Technique

In the past few years, MWI technique has attracted the attention of many research teams because of having the potential to provide the cost-effective and non-ionising imaging system with high accuracy. The reason for this is that malignant tissue, blood clot, and lesion make the great dielectric contrast at microwave frequencies [9], [13], and [26]. Accordingly, the MWI technique can be known as alternative imaging tools.

The MWI technique has been classified into two main categories, microwave tomography [27–32] and radar-based MWI [33–47]. Microwave tomography techniques are often suitable to a single frequency or narrow-band multi-frequency signals due to its time consuming nature, while radar-based MWI techniques require wide-band signals to produce accurate images.

2.3.1 Microwave Tomography

Microwave tomography estimates the dielectric permittivity map of the specific tissues using the collected measured signals recorded by the antenna surrounding the tissues [48]. Tomography reconstructs the spatial distribution of dielectric properties within the object using inverse scattering algorithm. In fact, the forward and the reverse electromagnetic field problem is solved in microwave tomography reconstruction to enable the detection and localisation of the unhealthy tissue in the images.

The tomography techniques generally are suitable for single or multi-frequency measurement setups that generally employ the matching medium for decreasing the reflection of the skin. Some researchers have applied single-frequency tomography for MI, for instance, authors in [28], [30] employed single-frequency at 2.45 GHz with the aim of head and heart imaging, respectively. The promising results of the homogeneous head models have been obtained particularly in the differential imaging area. The microwave tomography technique has been proposed for breast scanning by authors in [27] which is capable of performing in various frequency ranges between 300-1000 MHz.

According to the above-mentioned, microwave tomography-based approaches are time consuming due to need solving the complicated non-linear reverse scattering problem. Hence, cannot be suitable for medical applications, particularly in the medical emergency sites where rapid diagnosis is essential.

2.3.2 Microwave Beamforming Technique

The radar-based technique solves a simpler computational problem by seeking only to identify the location of the dielectric contrast due to the presence of a scatterer in the imaging domain [35,36], [39,40], and [43]. In the UWB radar-based technique, an antenna or array of antennas is employed for transmission and receiving a short pulse from various positions. The information about the presence, location, and size of the target can be obtained through the existing time delay between transmitted and scattered signals and also the amplitude of the scattered signal. The area with increased backscattering can be considered as abnormal tissue location (target location). This approach focuses only on the imaging the abnormality rather than the whole tissue. In fact, the aim of this imaging approach is providing the information on the shape, size and the location of the

abnormality within tissue.

In contrast to tomography, radar-based imaging avoid complex image reconstruction algorithm, means that the signal processing is much easier and faster than in microwave tomography approach. In addition, the radar-based imaging technique employs the Ultra-wideband Pulse which includes of low to high frequencies. It is worthwhile to mention, the low-frequency band secures penetration with adequate depth while the high-frequency band secures sufficient resolution of the obtained images.

Consequently, The UWB radar technique is capable to identify the presence and location of the target with a high amount of scattered signal as an abnormality.

2.4 Physical Principles Governing Microwave Imaging

2.4.1 Electrical properties

Among various MI techniques, the MWI technique is recognised as a promising method due to its high potential to produce the image of the human body in a safe manner. This technique is based on the electrical properties of biological tissues that can be used as an indicator for diagnostic purposes. The electrical properties of the tissues include two main parameters called relative permittivity and conductivity. The significant difference in dielectric properties between healthy tissue and abnormal tissue leads to the contrast in the image and contributes to cancer detection. In fact, the presence of tumour, blood clots, and bleeding tissue in the body causes a large dielectric contrast in medical images.

As previously mentioned, microwave images for medical applications are maps of dielectric properties contributions in the body with the help of electromagnetic fields at microwave frequencies of 300 MHz to 30 GHz. Hence, the large difference in electromagnetic properties between healthy tissue and malignance tissue is the fundamental of MWI for diagnostic purposes such as tumour detection in breast cancer.

In general terms, a tumour [49, 50] is a mass of tissue that is the result of abnormal growth of the cells called cancerous cells. Commonly, the immune system is able to destroy a small number of cancerous cells, however, when the growth of cells are out of control, the immune system is not able to destroy them and a lump of tissue is formed and grows uncontrollably. The tumours can be divided in two categories [50], benign tumour and malignant tumour. The growth of the benign tumour is controllable and does not destroy surrounding cells. In contrast, malignant tumours grow in a high rate, spread to surrounding cells, and destroy the tissues.

The difference between the malignant and benign tumour is vital and should be addressed. Tumour morphology is another way to discriminate between malignant and

benign tumour in terms of size, surface, and density [51, 52]. Irregular surface and clustered margin are characteristic of malignant tumours, whereas, the benign tumours have a smooth surface and are approximately spherical in shape. However, previous cancer detection research [42], [53, 54], has assumed that the tumour has uniform shapes such as a sphere or ellipsoid.

On the other hand, the amount of water inside the tumour determines whether the tumour is benign or malignant [51, 52], [55]. Many studies have reported the impact of the water content in relative permittivity values [56–63]. Increasing the water content in malignant tissues lead to significant increase in both the dielectric constant and the conductivity values [51]. This difference in dielectric properties between malignant tissue and normal tissue is the basis of MWI technique for cancer detection. In fact, in microwave tomography technique, the amount of scattered energy is important. Malignant tumour has high amount of water as compared to normal fatty breast tissues. The high amount of water in the malignant tissue causes a large amount of scattering. On the other hand, the low amount of water in fatty tissues, implies the low absorption coefficient. Hence, the amount of back scattered signals from malignant and healthy breast tissue give the good physical interpretation of the dielectric properties of biological substance [64].

It is worthwhile to point out that, the normal breast tissues have dielectric properties approximately equivalent to fat tissue, whereas the dielectric properties of the malignant breast tissues are similar to muscle tissues [64]. Biological substances with high content of water such as tumour have higher permittivity than tissues with low content of water [64] and [65]. In agreement with the diverse sources, the dielectric properties of the normal breast tissues is around $\varepsilon_r = 9$ and $\sigma = 0.4$ S/m for conductivity, whilst the dielectric properties of malignant tissues is about ε_r=50 and σ=3 S/m [64]. The bone, fatty tissue, and lung have the lowest dielectric values while the blood and muscle have a highest permittivity values due to having plenty of water [66].

Accordingly, the MWI technique relies on significant differences in electromagnetic properties of biological matter (between healthy and malignant tissues) to detect the cancer [64, 65]. The several studies [56–60] that have investigated the electromagnetic properties of breast tissue in various frequency ranges, confirming that the differences in the relative permittivity are enough for MWI. The contrast for relative permittivity and conductivity between the normal and malignant breast tissue in frequency ranges of 3 MHz to 3 GHz has been reported to be 4.7:1 and 5:1 respectively [62]. The results of dielectric properties measurements of normal, benign, and malignant tissues in the frequency range of 500 MHz to 20 GHz have been reported in [63].

2.5 Phantoms for Imaging Systems

One of the essential components for the development of MWI systems in medical applications is the phantom. Since testing the validation of the MWI system is performed through phantom measurements, so, the development of the phantom is important for improving the MWI system. In the process of constructing the phantom, some items should be attention including the similarity of dielectric properties of those phantoms with the properties of human tissues, and the similarity of the geometrics characteristics of those phantoms with human tissue. Moreover, phantom fabrication should be performed using readily available materials, with stable properties in the long term, and low-cost. A variety of breast phantom with different designs has been reported such as cylindrical model [35] and hemispherical model [42], [67]. The next part of this chapter presents the testing of some candidate materials that can be used in the phantoms fabrication.

The following section reports the dielectric constant measurement of some candidate materials that are suitable for phantom fabrication.

2.5.1 Dielectric Constant Measurement of Materials Appropriate for Fabrication Phantom

Over the past years, a wide range of research has been implemented to introduce the natural materials suitable for mimicking tissues and fabricating the phantom with the purpose of testing the validation of the imaging system based on microwave technique [68–70]. One of the aims of such research is to assess the known organic materials to choose safe and low-cost materials appropriate for mimicking the electrical properties of the real human tissues. Another effort of those researchers was producing new mixtures by mixing more than one material that has similar dielectric properties to the dielectric properties of specific tissues.

Different research groups confirm that corn syrup is a suitable, cost-effective material that can be used for imitating the human tissues in the phantom fabrication [70–72]. Moreover, the mixture of corn syrup with water in different ratio gives the material with very low permittivity and conductivity that can be used to represent the various types of tissues for breast imaging using microwaves.

Further material that can be frequently used in the MWI system to mimic human tissue is the vegetable oil having a low permittivity value [58].

In [68] the mixture of oil-in-gelatine with different ratios is introduced as an excellent candidate to construct the variety of human heterogeneous phantoms with stability for a long time over the microwave frequency band. Other materials that are suggested for phantom fabrication are agar and gelatine which are suitable for microwave-based imaging

systems [68, 69], and [72].

2.6 Introduction to Cancer

2.6.1 Breast Cancer

According to the definition of the American Cancer Society (ACS), cancer is described as "a group of diseases characterized by uncontrolled growth and spread of abnormal cells" [73, 74] which is the second common cause of mortality in the world. Regarding the worldwide statistics, each year approximately 7.1 million of populations which is almost 12.6 % of universal mortalities die of cancer. Moreover, in 2018, the report of the "Cancer Research UK" announced that cancer caused 9.6 million deaths of people in the world [75]. Amongst all types of cancer, the most common cancer deaths are related to the lung, liver, stomach, and bowel [75]. However, any organs of the human body such as breast, brain, skin, bone, liver, lung, bone marrow, and colon can be involved with cancer. It is also possible to be engaged with cancer at any age. It is worthwhile to note that, in all types of cancers, the probability of such disease caused by genetic is very low and is around 10%. Moreover, a healthy diet and healthy style can prevent the occurrence of this disease and decrease the rate of deaths to 1/3 [73].

Breast cancer is one of the most common cancers that initiates in the breast tissue. As abovementioned, when the breast cells grow abnormally, tumour is formed in the body. If tumour remains within the normal boundaries of the tissues with a low rate of growth, is called a benign tumour whereas a malignant tumour exceeds normal tissue boundaries and spreads to other parts of the body [76]. Despite the type of breast cancer, the breast tissues that are involved with cancer show particular features in comparison to the normal breast tissues. Such characteristics are demonstrated through different imaging techniques and are the basis for breast cancer detection. Among these, dielectric properties are one of the characteristics that distinguish between the normal breast tissue and cancerous breast tissue and consequently lead to the detection of breast cancer using MWI techniques. The subsequent section discusses the dielectric properties of the breast tissue and its background.

2.6.2 Dielectric Properties of Breast Tissues

As mentioned before, the dielectric properties indicate the interaction between the electromagnetic waves and biological tissues. In the year 1949-1950 England with Sharples [77,78] and in 1951 Cook [79] reported their preliminary studies of the dielectric properties of human tissues at microwave frequencies. Since then, various investigations have been performed to measure a variety of healthy and malignant breast tissues [9], [58], [61].

Although, all studies have confirmed the contrast in the dielectric properties between normal and malignant breast tissues, the reported permittivity and conductivity values have differed in various studies [80]. In particular, this contrast varied form %200 and 500% [80]. Ward et. al attributed these contradictions to differences in experimental methods and the heterogeneity of breast nature. Differences in dielectric properties of tumour tissue can be related to the different stages of tumour in different malignant samples. The dielectric property values of the malignant tissue samples containing largely normal cells are different from malignant tissue samples with the prevalence of malignant cells. Considering all uncontrollable conditions, all studies attributed the lower mean permittivity and conductivity to fat tissues, while malignant tissues have higher permittivity and conductivity values than normal breast tissues.

In 2007, Lazebnik et. al performed a wide range of studies of the dielectric properties of normal breast tissue over the frequency range between 0.5 to 20 GHz with the aim of addressing the above-discussed discrepancies [62]. Lazebnik et.al divided the breast tissues into three groups in the term of the amount of adipose tissues in the samples (see Fig. 2.4.

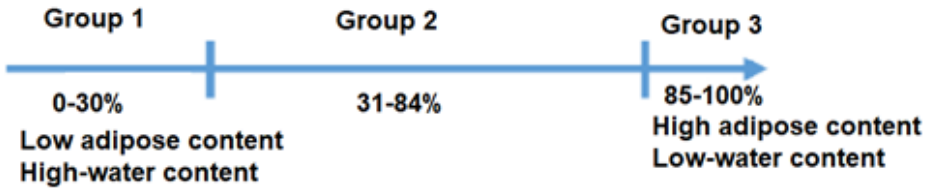

Figure 2.4: Normal breast tissue characterisation based on percentage of adipose content.

The wide range of studies consists of the variation of dielectric properties of breast tissues between the high adipose content group and the low adipose content group that reveal the consistent trend of a decrease in dielectric properties is directly related to the increased increase in the adipose content. The minimum dielectric properties values are related to Group 3 with the high adipose content tissues and the maximum dielectric properties values are related to Group 1 with the low adipose content tissues. The minimum variation is related to Group 3 due to the prevalence of adipose in the tissue and also due to the homogeneity of the breast tissue. In contrast, the largest variation belongs to both group 1 and group 2 since these two groups contain a heterogeneous mixture of fibroconnective, glandular, and some adipose tissue. In general terms, this wide-ranging study determined that the composition of normal breast tissue and the corresponding dielectric properties are considerably more heterogeneous across the microwave range than stated earlier in the majority of the studies, excluding Campbell et. al [58].

Additionally, Lazebnik et. al also has reported the results of the investigation on

the dielectric properties of normal, benign, and malignant breast tissue derived from cancer surgeries and biopsy [9]. The differences in the properties of all tissue groups were observed between the two studies. However, there were small differences in properties between two studies from group 1 and group 3 whereas there were large differences in the properties of group 2 are large. These differences were attributed to the characterisation of normal tissue samples between the two studies. At the next stage, the comparison between dielectric properties of malignant tissue and normal tissue was performed. The dielectric properties of cancerous tissue samples were compared to the dielectric properties of normal tissue samples with a maximum of 10% adipose content. Although the difference between the dielectric properties of cancerous tissues and normal tissues led to contrast, however, this contrast was extremely lower than was reported in previous studies. This study reported that there is an 8% contrast in the dielectric constant between normal and malignant tissues, and there is a 10% contrast in the conductivity between normal and malignant tissues.

In brief, the dielectric properties of malignant tissue reported by Lazebnik et. al were in excellent agreement with the earlier research, [56], [58], [81]. Nevertheless, the contrast in dielectric properties between the malignant tissue and normal tissue was not different more than 10% to the 300-500% contrast reported by Chaudhary et. al [61] and 200-500% contrast reported by Joines et. al [56]. Lazebnik et. al has performed these two studies citeLazebnik2007, [62] which are the most complete ex-vivo investigations about the breast tissue's dielectric properties. After that, a large number of studies was performed on dielectric properties of the breast including [82–87]. However, the most comprehensive studies to date belong to Lazebnik studies, and the results of dielectric properties reported in these studies are still used as the references and standard to develop microwave breast imaging and treatment applications.

2.7 Developmental History of the Microwave Imaging System

2.7.1 Microwave Imaging System for Breast Cancer

The initial work in the area of MWI for biomedical applications was performed by Larsen and Jacobi in the late 1990s. They developed a system with the aim of imaging the internal structure of a canine kidney using a developed antenna which was immersed in water [88–90]. They succeeded to describe clearly the various internal tissues by producing the two-dimensional (2D) images using the developed antennas immersed inside water [91]. Since that date, a wide variety of medical applications of MWI reported in the literature, ranging from brain injuries, bone injuries to breast cancer, and lung cancer. The most

important development over the past 10 years is breast cancer detection and a recent interest has been shown in the detection of brain abnormalities.

Over the past few years, a number of experimental systems have been developed for microwave breast imaging. In the year 2000, the imaging system comprising an array of antennas encircling the breast was used to detect the spherical tumour [92]. The dipole antennas were chosen to form the array due to its small size and low cost with reasonable bandwidth, however, low efficiency and directivity were the disadvantages of this model of antennas. In this system, both the array and the breast were immersed in two different matching medium, one having dielectric properties similar to breast tissue and one with dielectric properties similar to the skin tissue. The successful detection was achieved for both couplings.

In addition, in 2006, the University of Queensland designed the mechanical scanning platform with the purpose of investigation the planar and cylindrical configurations of their MWI system. The probe antenna was used for transmitting the signal and receiving the scattered signal reflected from the breast phantom and the imaged object. A cylindrical shape container was used for constructing the breast phantom filled with the low dielectric materials mimicking the normal breast tissue. A small object with high reflection was placed inside the breast emulating the tumour [93].

Moreover, in 2010, the development of the UWB MWI system incorporating a circular scanning system with the ability to mechanically rotate the sub-system was performed to obtain more scanning angles [94]. A breast phantom and a tapered slot antenna have formed the scanning system. A cylindrically shaped container was filled up with oil to emulate the fat tissue and a small plastic circular cylinder was filled up with water to simulate the tumour. The obtained images was generated using the novel reconstruction algorithm.

In the year 2012, the new UWB MWI system in circular shape was designed to image a heterogeneous breast phantom [95]. The four tapered slot antennas were used with the ability to utilised the monostatic and bistatic modes of operation. The experiments were performed using breast phantom mimicking the real breast tissue (including both low and high dense tissue) at microwave frequency. An object with dielectric properties close to the real tumour was placed in the phantom to mimic the real tumour. To generate the images of the proposed breast phantoms, a monostatic mode employing one antenna with an electrical stepper motor was used to rotate the phantom and obtain a minimal scanning angle of 0.72° angle [95].

In 2012, the development of a tissue sensing adaptive radar (TSAR) prototype of radar-based breast imaging system has been performed by the research team in university of Calgary [96]. The patient lies on the table in prone position whilst the breast is immersed in the immersion liquid. The select group of patients have been scanned using the

prototype [37]. Employing the monostatic technique and also filtering the skin reflection are the difference of this system compared to Bristol university method. Promising result were achieved where the restored images were similar to clinical results.

Moreover, in 2016, some studies were performed to investigate the effect of the complexity in the breast model on the MWI signals [97]. Extensive research was carried out attempting to develop a MWI techniques with the aim of achieving the safe breast imaging method. During these years, the research team of London South Bank University in cooperation with the UBT Srl, University of Perugia, Italy, studied the development of a microwave breast imaging system which eventually led to the design and construction of the MammoWave, a novel microwave breast imaging device [98], [99].

In 2019, researchers of London South Bank University in collaboration with UBT Srl presented MammoWave [100]. The device consists of an aluminium cylindrical hub containing two antennas operating in free space. The device also includes a cup that holds the breast of the patient when she lies on the examination bed in the prone position.

The validation of the MammoWave has been performed through phantom measurements having inclusions with different dielectric constants. Then, the performance of the dedicated device has also been verified through performing other sets of the clinical examinations on 51 breasts consisting of 22 healthy breast tissue and 29 unhealthy breast tissue (having the lesion) [100, 101]. The obtained clinical results verified that the microwave breast imaging device is able to produce high-quality images and provide a clear detection of the breast lesion in a safe condition without using ionizing radiation and any breast crushing.

2.7.2 Microwave Imaging System for Brain Stroke

Another application of the MWI system is brain stroke evaluation. Since the shape of the brain is similar to the breast, the researchers were interested to investigate the applicability of the MWI technique for brain stroke detection based on the difference in dielectric properties between healthy tissue and injured tissue [102]. Although the brain and breast are similar in terms of shape and are close to spherical shapes, however, each organ comprises of different layers. The breast organ consists of the skin and fat layers, while the human head comprises of skin, fat, bone, and white matter layers [63]. According to the electromagnetic theory, the great reflections of the incident electromagnetic wave is due to the discontinuities of the boundaries [42], [53, 54]. The reflection level strongly relies on dielectric properties. For instance, as mentioned previously, the difference in dielectric properties between the tumour and the fat in breast cancer detection reaches 10:1 [43]. In brain stroke detection, the difference between the dielectric properties of the blood tissues and the white matter tissue can be used. Although the difference in dielectric properties in the brain is significantly lower than the breast, however, it is still

noticeable.

A wide range of studies has performed to develop the MWI system for human brain abnormalities. In 2008, the possibility of using microwave tomography for brain stroke detection was investigated by Serguei et al, [13] at the Keele University school of medicine. The 2-D human head model was used to investigate the brain-injured detection through simulation. The head model consisted of different layers such as the skin, skull, cerebrospinal fluid, and grey and white matter layers. The direct problem-solver technique was applied in the frequency range of 0.5-2.5 GHz to reconstruct the images of the stroke.

Also, in 2008, brain monitoring was performed to stroke detection by simulation antenna arrays. A head model consisted of muscle phantom in a cylindrical-shape and a haemorrhage stroke area in a spherical shape with a radius of 0.5-3 cm. This head model was surrounded by the eight antenna elements and the gap between antenna and head model was filled with a high permittivity matching medium. According to the obtained results, there is the difference in return loss of up to 3 dB, between the case of with and without the stroke which is the demonstration of the ability of the proposed system for stroke detection [103].

In 2008, the possibility of brain stroke detection was investigated through simulation [104]. In the simulation, the set-up system consisted of 16 antenna elements in an elliptical shape that were placed around the head model as transmitters. The head model used in simulation was derived from the MRI scan data. The dielectric properties of different types of tissues and a stroke area were defined from [13], [37], [105]. The possibility of detecting the stroke area with 15 mm radius was illustrated through the simulation results.

In 2011, another MWI system consisted of three Vivaldi tapered slot antenna array was proposed and tested for brain cancer detection. The antennas were designed to be suitable for use in the frequency range between 5 GHz to 10 GHz. A multilayer sphere with a radius of 60 mm was used to represent the head phantom in the simulation. A sphere with a radius of 5 mm played the role of a tumour inside the phantom. The results derived from the simulation illustrated the backscattered signals of the target when placed in various positions. The simulation results showed that the weak scattering observed when the position of the target is far from the antenna array. Consequently, employing rotating the array around the head phantom could be improved the results. [106].

Further studies of the MWI system for brain stroke detection was reported in [107, 108]. One of the most important prototypes of MWI that has recently been studied by the research team at Chalmers University, called "Stroke-finder" was presented in [107], [109]. The mentioned MWI prototype was employed for the detection, classification and discrimination between two sorts of intracranial bleedings (brain haemorrhage and brain ischemia) in order to diagnose patients at the early onset of stroke. Another critical

research that has been done in the field of brain stroke, is the "BRIM G2" developed for brain scanning at EMTensor [108]. The "BRIM G2" is developed to exhibit brain stroke tomography. Their proposed MWI system aims to detect haemorrhagic brain stroke in the human head. Despite achieving successful results in brain stoke disease, the use of 177 antennas in their proposed device [108] makes it very complex and reduces its popularity. However, research in this area is ongoing.

2.7.3 Microwave Imaging for Skin Cancer

Another application of the MWI system is skin cancer detection. The human skin can be introduced as the largest organs and skin cancer is one of the most common cancers with a high percentage of prevalence in the world. In general, there are three kinds of skin cancers including basal cell carcinoma (BCC), squamous cell carcinoma (SCC), and malignant melanoma [73, 74].As mentioned previously, the composition of the tumour tissue is different from healthy tissue. If the malignant tumour forms in the skin tissues cause an increase in water content in skin layers [56]. Therefore, the high content of water in skin tissue is evidence of the malignant tumour's presence. In skin cancer, the amount of water in the epidermis layer reaches up to 81% [110]. The changing of water content in skin tissue leads to a variation in the value of tissue's permittivity. The contrast between normal tissue and malignant tissue at the microwave frequency is an indicator of skin cancer detection.

This is a fact that, in the majority of cancer cases particularly in skin cancer, it can be completely cured with detection in early stage [111]. Some MI methods such as dermoscopy and standard camera images are available as a suitable tool for diagnosing skin cancer at early stages. On the other hand, currently, the biopsy technique is the most common method used for skin cancer diagnosis. In the biopsy method, a small lesion of skin is removed and tested in the laboratory [112] and the results come up after approximately one week but the accuracy of the results is not guaranteed. In addition, another diagnosis technique that is used for skin cancer is the reflectometer method [112], which exploits the millimetre waveguides for distinguishing between the normal lesion and malignant lesion [113]. Nevertheless, there are some limitations and drawbacks corresponding to each of them. Although the expression of the limitations of the current tools, is beyond the scope of this thesis, however, the need for achieving a safe, fast, and reliable system with the capability of diagnosing skin cancer at an early-stage is addressed.

Limited studies have performed using a microwave technique for skin cancer detection. Over the past years, several skin models have been employed to simulate the different skin layers by considering the specific electrical properties. For instance, the simulation of the skin layers is proposed by employing a variety of uniform multi-layered models. In the proposed models each layer distinguished by a set boundary and specific permittivity and

conductivity [114], determined by those of free water content [115]. The authors in [114] performed modeling the skin using the forearm and palm data through simulation. The proposed skin model consisted of two different layers which each layer was distinguished by boundaries.

In 2016, the simulation study aiming to investigate the possibility of skin cancer detection was reported in [111]. The research team of London Southbank University proposed the MWI technique based on the HP that was initially performed for breast cancer detection. They applied HP imaging algorithm to multi-layered skin model with an inclusion representing a tumour. Consequently, the capability of MWI technique to skin cancer detection have verified through analytical simulation.

2.7.4 Microwave Imaging for Bone Health Monitoring

Another application of the MWI system is bone disease detection and evaluation. Many research groups have started working on microwave-based systems for bone imaging. According to the studies of researchers, there is an inter-correlation between the dielectric properties and mechanical properties of human /animal bone at microwave frequency up to 5 MHz (300kHz-3MHz) [116, 117]. The results of researches also demonstrate "bone fat and collagen contents are strongly related to relative permittivity while water content is significantly related to conductivity" [118]. Since the mechanical properties of bone are determined by bone mineral density, tissue trabecular structure, and organic composition [118], therefore, dielectric properties can be used as an indicator for bone health investigation.

Some studies have performed to investigate the possibility of MWI technique for bone disease monitoring. For instance, in [119] a preliminary study on the possibility of using the Tissue Sensing Adaptive Radar (TSAR) microwave technique [53] for the investigation of knee anatomy and pathology, focusing on meniscal tears, was performed. The results, both numerical and experimental, suggested that radar-based MWI has potential for knee imaging.

Further research of this approach has been done to investigate the capability of the TSAR system in detecting multiple tears and its resolution when applied to the analysis of meniscal injuries [120]. Afterward, the authors continued their research on the potential of the radar-based microwave approach to imaging the knee joint, in particular for the detection of meniscal tears of the ligaments and tendons using a tank of canola oil as a matching liquid. The results were reported in [121].

In addition, some researchers worked on the feasibility study of using the MWI technique for Osteoporosis detection. Among these, in 2010, the authors in [122] begun imaging the heels of injured patients to assess bone health. The study's results were promising as a first step towards developing a microwave tomography system that leads

to diagnosing the bone health problem.

In 2011, a pilot study for MWI of the heel was proposed by the research team of Dartmouth College applying a simple adaptation of the existing breast imaging system [27]. The same group carried out the investigation of Microwave tomography for bone imaging based on a principle that shows there is a strong correlation between the dielectric properties and clinically important mechanical properties of bone. The primary results from simulation experiments reported in [117].

In the year 2012, the authors in [123] obtained 2D and 3D calcaneus bones images using microwave tomographic technique to evaluate the relation of the microwave properties with X-ray density measures. This investigation was performed on two volunteer patients. The results show that there is a good relationship between permittivity and conductivity and the computed tomography-derived density measures. The outcome of this research was the first 3D clinical models of microwave tomography images of the calcaneus bones.

In 2016, the authors in [16] proposed a Microwave scanning system for bone imaging. The proposed imaging system was based on dielectric contrast between the target and surrounding tissues. The MWI system comprised of two antipodal Vivaldi antennas for collecting the signals in a multi-monostatic fashion, operating in a frequency range of 0.5-4GHz. The multi-layer phantom consists of skin, muscle, fat, and bone tissues were used for microwave experiments. The 3D images of the tibia and fibula were reconstructed using the non-coherent migration method (in the time domain) which is a version of the beamforming procedure, after applying an average trace subtraction strategy to remove the artefact. The finding of this research was promising in bone imaging using a multi-layer complex limb-mimicking phantom.

2.8 Ultra Wideband vs. Narrowband

UWB is a unique communication technology with the ability to achieve high data rates up to 1Gbps (Giga-bite per second). Concerning the various studies that have been performed to investigate the capability of microwave techniques for MI, it is important to point out that employing Ultrawideband has more beneficial compared with the narrowband. Using UWB in medical application is promising and reasonable because it uses a very low power pulses and is also appropriate for short-distance applications [124, 125]. Since UWB is power efficient and is able to provide accurate results can be introduced as a good candidate for medical applications. In addition, the UWB system does not suffer from fading problems which is the main drawback of narrowband systems because of using short pulses which results in high multi-path resolution. In the UWB system, the distribution of power is performed over a wide range of frequencies, which leads to a very low level of power at each frequency. Therefore, less interference with other RF (Radio frequency)

systems is predicted. Another advantage of using UWB in comparison to narrowband for medical applications is, UWB system does not require any complicated modulation and demodulation which used for conventional continuous-wave transmission systems. The non-complex components in the UWB system make it cost effective, design simplicity, and easy to perform. Therefore, the UWB system is more simple and faster than the narrowband system. Besides these, since UWB signals cover the large bandwidth and allow the very high resolution in the images, can be used as a top priority in healthcare applications and MI.

UWB uses a very large band and its advantage is can achieve both good penetration and high resolution, whereas, narrowband uses a small band that can gives good penetration but cannot obtain high resolution. This is the capability of the UWB compared with the narrowband that leads to obtain more accurate results in terms of resolution and signal to clutter [126].

Concerning using microwave techniques in medical applications particularly, in bone lesion imaging, the UWB radar technique seeking only the presence and location of the high scattered signal rather than reconstructing the entire dielectric properties of the tissue which is the aim of microwave tomography. Therefore, the UWB radar technique is less computationally complex and non-time-consuming in comparison with tomography. Accordingly, compared to microwave tomography using narrowband, the UWB can be more suitable for medical applications, particularly in medical emergency sites.

Capabilities of the UWB includes better penetration within the different mediums, obtaining high resolutions, low electromagnetic radiations, consuming much less power, and being faster. Since the UWB receivers are able to transmit pulses in a few thousand billions of seconds makes it more popular to use in the MI systems rather than the narrowband system [127].

2.9 Research Gap and Proposed Research

Over the past decades, MWI has been known as a promising method in medical applications. The MWI has the potential to revolutionise the current diagnostic medical methods due to its various advantages. Using non-ionizing radiation, low cost, portable system, low complexity, and fast imaging is the benefit of the MWI system. As already stated, over the last decades, the MWI systems have been developed by the efforts of many researchers. Different MWI systems have been proposed for medical applications, particularly for breast cancer detection. However, achieving a reliable, inexpensive, simple, fast, portable, and safe imaging system is still demanded. In addition, there is no microwave clinical imaging system suitable for use in the emergency site. On the other hand, to date, very limited studies have been performed on skin cancer as well as on bone lesion

detection using the MWI technique. Accordingly, the investigation of the possibility of MWI techniques for skin cancer detection and on bone lesion detection is still challenging. Consequently, the extension of MWI techniques for other diagnostic applications such as skin cancer and bone lesions is the aim of this research.

Over the past years, many research teams have been performed phantom development and have used it in MWI experiments. However, the majority of these phantoms were very simple and did not meet the real shape of human parts. Performing microwave experiments using a more complex realistic phantom that emulates the dielectric properties of human tissues is still a challenge. Therefore, the objective of this research is also to develop the phantoms to mimic real tissues.

2.10 Summary/Conclusion

This chapter discussed the different types of current imaging techniques, suitable for medical purposes. X-rays, Ultrasound, CT scan, and MRI imaging are the prevalent imaging methods with the potential to produce valuable images of the inner human organs. However, each of these imaging approaches suffers from its own drawbacks such as the risk of ionising radiation, time-consuming, non-portable, and expensive. Therefore, achieving a clinical imaging system that can be overcome such limitations and be able to detect cancer in the early-stage is the top priority of researchers. In contrast, the MWI technique is recognised as a promising method due to its high potential to produce the image of the human body in a safe manner. This technique is based on the electrical properties of biological tissues that can be used as an indicator for diagnostic purposes. The significant difference in electrical properties between normal and malignant tissues at microwave frequency leads to contrast in the images and helps to diagnose the disease. This contrast is the basis of MWI techniques for cancer detection. This contrast is the basis of MWI techniques for cancer detection. Hence, MWI transformed into a promising technique for early-stage cancer detection in a safe manner (non-ionizing radiation). The MWI Techniques are classified into two types named microwave tomography and radar-based imaging technique. Each technique has benefits and limitations. For instance, compared to microwave tomography, the radar-based imaging technique is much simpler and easier in terms of signal processing and is able to overcome some limitations. Various research teams have been focused on the development of MWI techniques for medical applications, particularly for breast cancer and brain injury detection. The aim of these researches was to find an appropriate imaging approach with the features of safe, low-cost, and portability with the ability to assess medical problems rapidly. Moreover, some research groups have performed preliminary studies of the MWI technique for skin cancer and bone imaging. This research is aimed to develop the MWI radar-based technique for diagnostic

applications such as skin cancer detection and bone lesion detection.

Chapter 3

Methodology

3.1 Introduction of Technical Approach

The perspective of this research is the development of a novel, fast, and precise UWB MWI method for medical applications. This research aims to investigate the capability of MWI for skin cancer and bone lesion detection. The current chapter discusses the proposed methodology.

This chapter consists of two sections; the first section discusses the following parts; illustrating the block diagram of the proposed method, demonstrating the frequency domain experimental setup, explaining all hardware components, describing all relevant physical fundamentals, introducing the proposed MWI algorithm, performing validation of proposed imaging algorithm through simple phantom measurements in the anechoic chamber. Then, introducing the MammoWave imaging device, demonstrating the measurements setup, and performing the validation of the MammoWave device based on the HP imaging algorithm through simple phantom measurements is presented.

3.2 The Frequency-domain Experimental Setup in Anechoic Chamber

The experimental setup has been established in an anechoic chamber requiring simple hardware to perform all the microwave measurements at the LSBU laboratory. Some hardware equipment is needed for performing MWI measurements. The UWB frequency-domain measurements have been performed using the Vector Network Analyser (VNA) to acquire the transfer function (S21) at the desired frequency band. Two wideband dipoles omnidirectional antennas (one used as a transmitting and the other used as a receiving antenna, both of them connected to the VNA device), vertically polarised, and have been used in free space. For each set of measurements, the transmitting antenna has been fixed

on the turntable with a 10 cm distance from the center of the object (phantom), and the receiver antenna is approximately 6.5 cm away from the center of the phantom. The phantom has been placed on a computer-controlled turntable stand with 6° of angular resolution.

3.2.1 Block Diagram of Experimental Setup

The majority of UWB microwave systems for MI are based on frequency domain measurements technology. The proposed frequency-domain MWI system consists of two main parts; (i) hardware, containing some pieces of equipment to perform and to complete the measurements procedure, and (ii) Software or image-processing that is responsible for reconstructing the image, detecting the lesion inside the object [128] (see Fig. 3.1). The basis of the microwave measurements procedure is that the generator produces the microwave signals which illuminating the object and then reflected. The list of required Hardware is as follows:

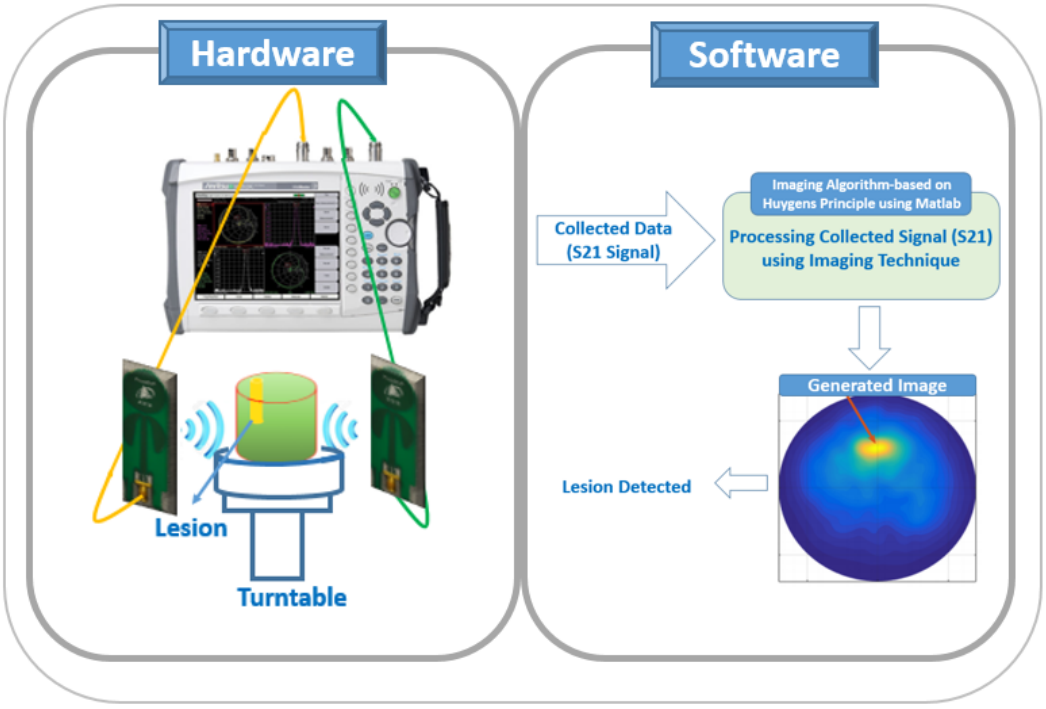

Figure 3.1: Block diagram of experimental setup

3.3 The Required Hardware Equipment

The list of the required hardware for performing the measurements in the anechoic chamber is as follows:

- UWB PulsON P200 Antenna

One of the substantial elements in both MWI tomography and radar-based technique is the antenna which acts as a transmitting and receiving sensor. The transmitting antenna is responsible for sending the microwave signals toward the object under test (OUT) whereas, the receiving antenna is responsible to collect the scattered signals from the OUT. Selecting a suitable antenna that has features such as high gain, small size, be able to transmit a wide variety of frequencies with higher efficiency, be able to operate in both low and high-frequency ranges, is very important in the performance of the MWI system. The UWB antenna is known well-suited using in MWI systems for medical applications. The PulsOn BroadSpec P200 omnidirectional antennas which are small, inexpensive, and high-efficiently, have been used for this research (see Fig. 3.2).

Figure 3.2: The UWB PulsOn P200 antennas

This antenna is the planar elliptical dipoles that allows matching with a return loss of approximately -14 dB or better [129]. The radiation efficiencies of more than 90% is another feature of the PulsOn antenna [130]. The characterisation of the PulsOn P200 antenna is summarised in the table below.

Both antennas (coupled through a VNA) are vertically polarised operating in free space and rotate around the phantom to gather the signals in a multi-bistatic fashion.

- Vector Network Analyser (VNA)

The VNA is a portable handheld Vector Network Analyser that used a step frequency method to do measurements in a wide range of frequency. VNA is one of the main UWB

Table 3.1: The PulsOn P200 Antenna Characterisation [129]

Characteristic:	**Specification:**
Pattern	Omni in azimuth to ±15 dB
Polarisation	Linear (vertical)
Matching	VSWR 1.5:1; $\|S_{11}\|$ -14 dB
Gain	Nominally 3dBi
Phase Response	Linear
Efficiency	Nominally> 90%

measurement instruments in frequency domain measurement technology. This instrument is able to measure the magnitude and phase characteristics of the 1-port or 2-port networks.

In this research, the two-ports VNA, model MS2028C, Anritsu (manufactured by Anritsu EMEA Ltd) operating in frequency range 5MHz to 20 GHz has been used to perform the measurements (see Fig. 3.3). The transmitter and receiver antennas have been connected to port 1 and port 2, respectively. For every single time, a signal (at microwave frequency) illuminates the object (phantom), and the reflected signals from different angular positions around the phantom records by the VNA, and then the scattered parameters are calculated.

Figure 3.3: VNA device, model MS2028C, Anritsu.

S-parameters (scattered parameter) represent the characteristics of transmission and reflection in the frequency domain. In another word, S-parameters are known as complex numbers that contain the real and imaginary parts or magnitude and phase parts. The Two-port VNA is able to measure four fundamental S-parameters.

Commonly, S-parameters are illustrated in a matrix format, in which the number of rows and columns is equal to the number of ports. In the Sij parameter, “i” and “j” represent the output and input ports respectively.

In two-port VNA device, the signal measurements that coming out from ports 1 are known as forwarded measurements, whilst the signal measurements coming out from port 2 are known as reverse measurements. Moreover, reflection measurements, represent the signals that leave and return from/to the same port, whilst transmitting measurements indicate the signals that come out from one port and enter to another port. For instance, the S-parameters for the measurements are described as follow:

The S-Parameters and their Relation to the Voltage

-S11 is the reflection coefficient (forward reflection) that represents the measured signal reflected back to port 1 when coming out from port 1. Generally, it shows how much power is reflected from the antenna and can be also presented as Γ or return loss.

-S22 is the reflection coefficient (reverse reflection) that represents the measured signal reflected back to port 2 when coming out from port 2.

-S21 is the transmission coefficient (forward transmission) that represents the measured signal transmitted to port 2 when coming out from port 1.

-S12 is the reverse transmission coefficient.

It should be noted that, according to the imaging algorithm, we are interested in collecting the S21 parameter which is defined as a complex number.

When we are interested to describe a network in terms of amplitude and phase for frequencies instead of voltages and currents, S-parameters can be used to describe the relationship between different ports. In other terms, S-parameters indicate a complex network as a simple black box, and it shows easily what happens to the signal in that network [131]. For a two-port network, the S-parameters in terms of voltage can be described as follow:

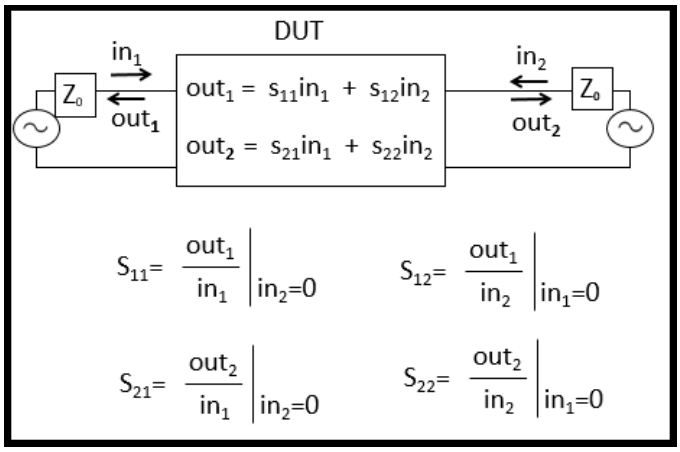

Figure 3.4: A two-port S-parameter matric records the reflection coefficient and transmission gain from both sides of DUT [131].

As Fig. 3.3 shows, the input port voltage reflection coefficient is denoted by S11, whiles the output voltage reflection coefficient is indicated by S22. Also, the reverse voltage gain is presented by S12, whilst the forward voltage gain is illustrated by S21.

As mentioned earlier, the reflection coefficient and transmission gain from both sides of a two-port network can be determined by S-parameter Matrix. The Return loss, Gain, VSWR can be determined by S-parameters.

The **Return Loss** can be expressed as follow:

$$RL_{\text{in}} = 10log_{10}|\frac{1}{S_{11}^2}| = -20log_{10}|S_{11}|dB$$

$$RL_{\text{out}} = -20log_{10}|S_{22}|dB$$

The **VSWR** (Voltage Standing Wave Ratio) is a function of the reflection coefficient. The reflected power from the antenna can be demonstrated by VSWR.

$$\text{VSWR} = \frac{1 + |S_{11}|}{1 - |S_{11}|}$$

It should be noted that the VNA has been calibrated to make sure about the performance of the antennas before starting the measurement procedure.

- Turntable Stand

An automatically rotating stand (called a rotatable table) is another piece of equipment in the anechoic chamber used in performing the measurements. In the frequency domain measurements process, the phantom is placed on the surface of the turntable, and the stand rotates every 6° to allow recording the signals for the whole 360° around the phantom and completes a set of measurements.

- Rotatable graduated Phantom Holder

The rotatable graded phantom holder is another required measurement equipment that has been used to improve the measurement accuracy. Regarding the strategy of this research, to perform a set of measurements in different transmitting positions, the phantom is rotated instead of rotating the transmitter antenna. In fact, the transmitting antenna is mounted on the rotatable stand, and the phantom is rotated manually for a specific degree to meet the new transmitting position. Therefore, using a rotatable phantom holder

prevents the phantom from moving during the rotation, increases the accuracy of the measurement, and decreases the percentage of error rates in the measurement process.

The graded phantom holder has been designed (with a scale from 0° to 360°) using Inventor Software and then has been constructed through 3D printing using ABS material. Fig. 3.5 indicates the designing and constructing the phantom holder and Fig. 3.6 shows the anechoic chamber measurement setup.

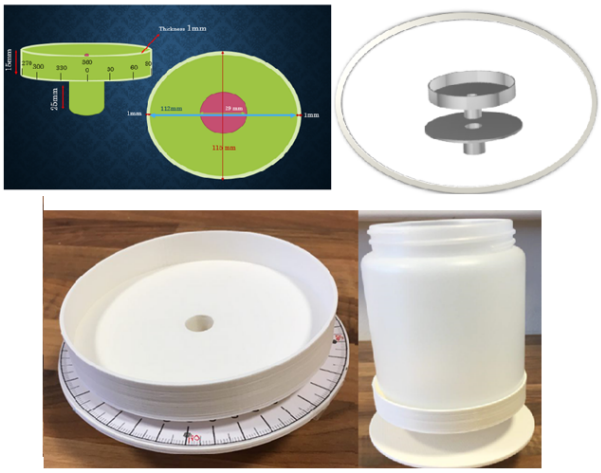

Figure 3.5: Designed and fabricated phantom holder using 3D printing.

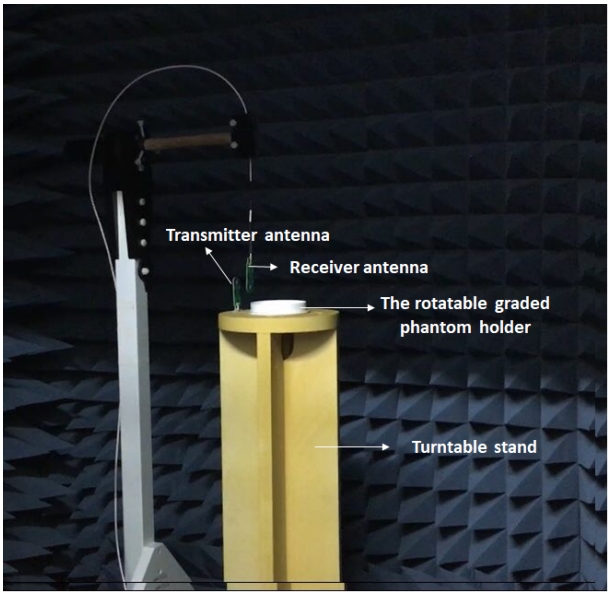

Figure 3.6: Anechoic chamber equipments, i.e. antennas, rotatable table, phantom holders.

- Computer Workstation

The total mathematical computations are performed using Computer Desktop. The processing of the collected signals from each array is extracted and imported to the MATLAB interface installed in the PC.

3.4 Related Fundamental Physical Concepts

3.4.1 Absolute Permittivity, Relative Permittivity, and Conductivity

Permittivity is the property of a particular medium that affects the magnitude of the force existing between two ports of charge. The absolute permittivity of air (or vacuum) is indicated with ε_0 and its value is equal to 8.854×10^{-3} F/m (Farad/meter), whereas the absolute permittivity (or actual permittivity) of all other insulating medium is shown with ε and its value is more than ε_0.

The ratio of these two permittivities (i.e. absolute permittivity (ε)) of the medium to the absolute permittivity of the air (ε_0) or vacuum) is known as the relative permittivity of that medium and is symbolised by ε_r.

$$\varepsilon_r = \frac{\varepsilon}{\varepsilon_0} \tag{3.1}$$

The human body comprises various materials such as water, dissolved organic molecules, macromolecules, ions, and insoluble matter. Each substance has specific electromagnetic properties that can be assessed by electrical permittivity and conductivity. Dielectric properties (permittivity and conductivity) characterise the interaction of electromagnetic waves with biological tissues. When the biological tissues are exposed to an electrical field, the electric field will cause the randomly oriented molecules to be aligned to the electric field direction. The external electric field impacts this alignment and results in the polarisation of the molecules within the tissues. This polarisation of molecules induces an electric field in an opposite direction to the applied field, which is smaller in magnitude [132]. The complex permittivity of material reported in [57] describes the molecules' resistance to the applied external electric field.

$$\varepsilon = \varepsilon_0 \left(\varepsilon_r - j\varepsilon_r'\right) \tag{3.2}$$

where ε_r represents the relative permittivity or dielectric constant, ε_r' is the loss factor and as mentioned above ε_0 is the permittivity of a vacuum. The loss factor can be demonstrated as:

$$\varepsilon_r' = \frac{\sigma}{\omega} \tag{3.3}$$

where the σ is the conductivity of the material with a unit of Simens per meter (S/m), ω is the angular frequency in radian per second (rad/s), in which ω is presented as follow:

$$\omega = 2\pi f \tag{3.4}$$

According to eq. (3.2) and eq. (3.3), the relaxation time associated with the frequency describes the frequency dependence of the permittivity or the dielectric dispersion of the biological tissues.

3.4.2 Near-Field & Far-Field

The electromagnetic or EM waves consist of a magnetic wave and an electric wave. A transmitting signal applied to an antenna produces the fields. The characteristics of the electromagnetic field changes with respect to the distance from the antenna. The radiation field is typically composed of the near field and the far-field. In the near-field, the pattern shape of the field is depended on the distance from the antenna. The near-filed can be divided into two different regions, in which are known as reactive near-field and radiating near-field. As shown in Fig. 3.7, the regions that are in close proximity to the antenna are called reactive near-field, which the energy of the electromagnetic decreases by increasing the distance from the antenna, whereas the regions are next to the reactive near-field region called radiating near-field [133].

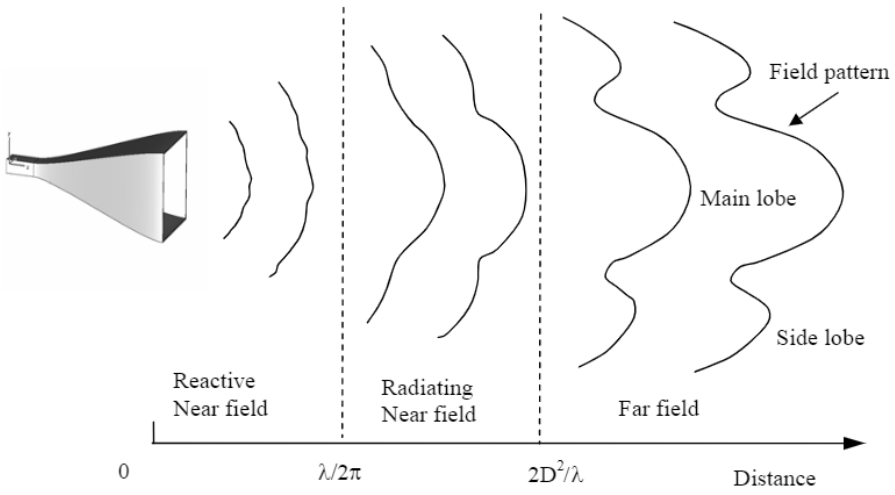

Figure 3.7: Reactive near-field, radiation nearfield, and far field regions.

Moreover, in the reactive near-field, the E-field and H-field present an unpredictable relationship. Therefore, the density of the power flow has complicated calculations. However, the region boundary [134] can be specified by:

$$R \leq 0.62\sqrt{\frac{D^3}{\lambda}} \tag{3.5}$$

where, R presents dimension the reactive near-field, D indicates the maximum dimension of the antenna, and λ is the wavelength that can be defined as a speed of light over frequency.

The radiating near field is the region between the reactive near field and far-field. In this region, the pattern shape of radiation varies with distance.

$$R \leq \frac{2D^2}{\lambda} \tag{3.6}$$

where, R presents the distance of the radiation near-field, D illustrates the largest dimension of the antenna, and λ is the wavelength that can be defined as a speed of light over frequency.

On the other hand, the region which is the farthest distance from the antenna is called the far-field, which, in this region, the pattern of the radiation does not change (in terms of shape) with the radiation distance. In the far-field, the E field and H field are perpendicular to each other. The far-field region boundary indicates as follows:

$$R \geq \frac{2D^2}{\lambda} \tag{3.7}$$

It should be highlighted that as the formulas show all these regions are frequency dependent.

3.5 Image Processing Algorithm

3.5.1 Description of HP Based Imaging Method

As mentioned in the literature, microwave technology relies on detecting the contrast at the interface between two healthy and unhealthy tissues with different dielectric properties. Recently, UWB has been applied to different medical applications with the purpose of detecting and monitoring. The are many benefits to using UWB technology, for instance, high resolution in generated images (due to the high bandwidth spectrum), low power transmission, reliability, and high capacity. In this research, the same principle is applied to identify the presence and location of the significant scatterers inside the cylindrical object i.e. forearm phantom employing the proposed imaging algorithm.

The proposed imaging algorithm deals with the specific principles of physical optics which is named the HP. In fact, an algorithm based on HP is applied to forward propagate the waves [135]. In more details: using HP to forward propagate the waves removes the need to solve inverse problems and, consequently, no matrix generation/inversion is required [135]. Along with its simplicity, capturing the contrast is the main ability of HP that is known as a feature of this physics principle. UWB provides an opportunity for all of the information in the frequency domain to be applied by combining the information from individual frequencies to create a constant image.

Let's clarify the HP procedure by expressing the example. It should be noted that

the HP points out that: "Each locus of a wave excites the local matter which reradiates secondary wavelets, and all wavelets superpose to a new, resulting wave (the envelope of those wavelets), and so on" [135].

For the sake of illustrating this proceeding, a cylinder with the radius of a_1 in free space has been considered. A transmitting line source tx_m in the frequency f is employed for illuminating the cylinder. Let us assume that ε_r and σ_1 represent the known dielectric constant and conductivity of the cylinder, respectively. It is supposed here that another small cylindrically-shaped object with a dielectric constant greater than ε_r, is considered as an inclusion inside the main cylinder (see Fig. 3.8). Hence, the identification of the existence and location of the inclusion only by relying on the measured field of the external surface of the cylinder is the challenge.

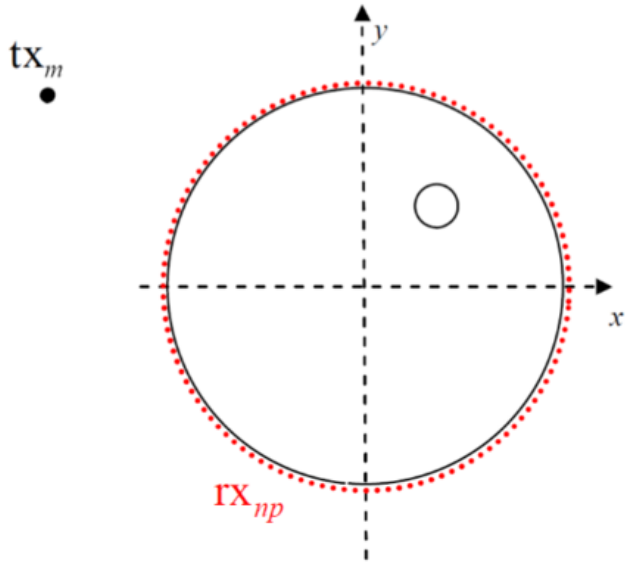

Figure 3.8: Problem in pictorial view, transmitting and receiving points are shown by the black and red dots respectively.

The S21 signals ($\mathrm{S21}^{\mathrm{known}}_{np,\mathrm{tx}_m}$) are measured with the fixed transmitter (tx_m), collected at the points rx_{np} displaced along a circular surface having a radius a_1, where a_1 is the distance from the receiving antenna to the center of the roaring table (6.5 cm), and the np is the number of receiving points on the cylinder-object and varies from 1 to N_{PT}.

The description of the measured S21 can be expressed in a mathematically way by eq. (3.8):

$$S21^{\mathrm{known}}_{\mathrm{tx}_m}|_{\mathrm{rx}_{np}} = S21^{\mathrm{known}}_{np,\mathrm{tx}_m} \quad \text{with} \quad np = 1, ..., N_{\mathrm{PT}} \tag{3.8}$$

Let's see what happens if HP is applied for reconstruction of the medium's internal field, using the field measured ($E^{\mathrm{known}}_{np,\mathrm{tx}_m}$) on its external surface as the locus of a wave.

According to the HP strategy, the interior scattered electric field E of the cylinder is calculated as the superposition of the fields radiated by the N_{PT} observation points of eq. (3.8) [126], [136]. It should be noted that the electric field E is reconstructed using HP helps that each point of the measurements is considered as a source that reradiated internally.

$$E^{\mathrm{rcstr}}_{\mathrm{HP,2D}}(\rho,\phi;\mathrm{tx}_m;f) = \Delta s \sum_{np=1}^{N_{\mathrm{PT}}} S21^{\mathrm{known}}_{np,\mathrm{tx}_m} G(k_1|\overrightarrow{\rho}_{np} - \overrightarrow{\rho}|) \tag{3.9}$$

where in eq. (3.9), $(\rho,\phi) \equiv \overrightarrow{\rho}$ represents the observation point, the tx_m demonstrates the number of transmitting antennas operating at frequency f, $|\overrightarrow{\rho}_{np} - \overrightarrow{\rho}|)$ is indicating the distance between the source and reconstructed point, Δs illustrates the spatial sampling which is the distance between two adjacent receiving points and can be defined by the eq. (3.10), k_1 represents the wave number for the media constituting the external layer (if known) and can be defined by the eq. (3.11). However, it has been shown that detection can be achieved also if setting k_1 as the free space wave number [137]., the string "restr" indicates the reconstructed internal field and the string "HP" demonstrates the employment of the HP-based procedure that is applying in eq. (3.9), and finally G is the Green's function that is used for homogeneous media with the aim of forwarding propagated the field using eq. (3.12) [136]. S21 is the parameter representing the complex transfer function from the transmitting antenna to the receiving antenna.

It was shown in [101], [136], that eq. (3.9) can capture the contrast, i.e., mismatch boundaries, and locate an inclusion within the volume.

It is worthwhile to point out that, in view of the fact that reconstructed electric field ($E^{\mathrm{rcstr}}_{\mathrm{HP,2D}}$) is influenced by both illuminating source and the frequency, these two parameters are very effective in the electric field reconstruction.

$$\Delta s = \frac{2\pi a_1}{N_{\mathrm{PT}}} \tag{3.10}$$

$$k_1 = \sqrt{(2\pi f)^2 \varepsilon_1 \mu_1} \tag{3.11}$$

$$G(k_1|\overrightarrow{\rho}_{np} - \overrightarrow{\rho}|) = \frac{1}{4\pi|\overrightarrow{\rho}_{np} - \overrightarrow{\rho}|} e^{-jk_1|\overrightarrow{\rho}_{np} - \overrightarrow{\rho}|} \tag{3.12}$$

It has to be stressed that there is no expectation to gain the correct internal field by using the HP procedure, even when it comes to homogeneous problems. It stems from the fact that HP is suitable for far-field phenomena, i.e. it refers to a propagating wavefront. Since we have plane wavefronts, therefore the knowledge of the E field is adequate in order to gain the far-field. From another point of view, with the aim of capturing and recovering the near field, either the knowledge of the H field or the normal derivative of

the E field is also required. In such circumstances, the evaluation of the internal field is not the purpose of the HP procedure. In fact, the intention is to investigate if the existing contrast which is the result of mismatch boundaries, can be identified by the HP procedure. Moreover, another purpose is to investigate whether HP is able to detect the location of inclusion inside the object. As mentioned previously, the capability to capture the contrast is caused by the dissimilarity between the two media's properties which were not taken to account by the eq. (3.9). Accordingly, the mismatch which happened in the area of transmission of the two media is illustrated by the reconstructed field. This mismatch paves the path for novel detection and also localization strategies.

For additional clarification of this problem, the outer cylinder is illuminated through various frequencies and also from the diverse illuminating positions, therefore, the whole set of the reconstructed fields will demonstrate the mismatch placed in the area of transmission of two media. In consequence, the detection and localization of inclusion will happen after summing incoherently all the solutions, i.e. the reconstructed fields.

Assuming we use N_F frequencies f_i, it follows that the intensity of the final image I can be obtained mathematically through the following equation, i.e. by summing incoherently all the solutions using Green's function (by summation the contribution of whole transmitting positions for all the frequencies).

More details of HP formulas can be found in [126], [136]:

$$I(\rho,\phi) = \sum_{i=1}^{N_F} |E_{\mathrm{HP}}^{\mathrm{rcstr}}(\rho,\phi;\mathrm{tx}_m;f_i)|^2 \tag{3.13}$$

- Artefact Removal Procedure

Obtained images of eq. (3.13) may contain some clutter partially or completely masking the inclusion, i.e. the lesion. This phenomenon is known as the artefact and may be due to images of the transmitting antenna or the first layer reflection or even due to multiple reflections occurring inside the phantom.

Artefact removal is the critical signal processing component in any imaging algorithm. Removing the artefact in the early stage and reconstructing high-quality images with minimal clutter are the main challenges in most imaging systems [138]. If the artefact is not perfectly cancelled, it could easily mask the region of interest, i.e. region of the presence of the tumour. Therefore, it could prevent achieving tumour detection at the stage of reconstruction of the image.

There are many artefact removal methods such as [39], [53], and [92]. In this research, we will employ the subtraction artefact removal method to remove the artefact.

Therefore, the artefact will be eradicated by applying the HP to the subtraction between measured fields of two adjacent transmitter positions (i.e. $S21^{\mathrm{known}}_{np,\mathrm{tx}_{m1}}$ - $S21^{\mathrm{known}}_{np,\mathrm{tx}_{m2}}$) which leads to removing the images of the transmitting antenna, or the first layer re-

flection, or even the multiple reflection occurring inside the phantom, that may cover the region of interest [101], [126], [136], and [139].

Consequently, in practical cases, it can be demonstrated that the artefact can be eliminated through using HP as follows:

$$E^{\mathrm{rcstr}}_{\mathrm{HP,2D}}(\rho,\phi;\mathrm{tx}_{m1}-\mathrm{tx}_{m2};f)=\Delta s\sum_{np=1}^{N_{\mathrm{PT}}}\left((\mathrm{S21}^{\mathrm{known}}_{np,\mathrm{tx}_{m1}}-\mathrm{S21}^{\mathrm{known}}_{np,\mathrm{tx}_{m2}})G(k_1|\overrightarrow{\rho_{np}}-\overrightarrow{\rho}|)\right) \quad (3.14)$$

with tx_{m1} and tx_{m2} belonging to the adjacent transmitter positions [126], [136].

More details; the rotation subtraction method requires two separate radar measurements. The first set of measurements is recorded by the antenna which rotated around the object (for the tx_{m1} transmitting position), and the second set of measurements of signals is recorded after the transmitting antenna has been rotated at the certain angle in the horizontal plane around the vertical axis (tx_{m2} transmitting position). Then the artefact removal procedure has been performed by employing the HP to the subtraction between measured fields of these two adjacent transmitter positions.)

Concerning the resolution, it is worthwhile to point out that; our expectation about the resolution is that it meets the limit of the optical resolution defined by one-quarter of $\lambda_{f_{\max}}$. It should be noted that the wavelength in the cylinder calculated at the highest frequency will define as $\lambda_{f_{\max}}$. This offers the rule of thumb to specify the greatest frequency to be applied.

3.5.2 Validation of Proposed MWI Algorithm through Phantom Measurements in Anechoic Chamber

This section discusses the verification of the HP-based imaging algorithm to detect and localize the inclusion through phantom measurements. For this purpose, a simple cylindrically-shaped phantom having an inclusion has been fabricated. Then, the set of measurements have been done to verify the ability of the HP-based imaging algorithm to detect the lesion inside the phantom.

The phantom has been fabricated by considering the electrical properties of human tissues that were assigned in the proposed phantom. Accordingly, a cylindrical plastic container with a height of 15 cm and a radius of 5.5 cm was chosen and filled up with the fat tissue's equivalents material (sunflower oil) having the dielectric constant value equal to 3.5 and conductivity value equal to 0.34 S/m. A cylindrical plastic tube having a radius of 0.5 cm and height of 7 cm filled up with tumour tissue's equivalent material (a mixture of water & salt) having a dielectric constant value of approximately 80 and a conductivity value around 6.42 S/m is mounted inside the external cylindrical plastic

container and plays the role of inclusion in the manufactured phantom. Fig. 3.9 shows the fabricated simple phantom. It is worthwhile to point out that the values of dielectric properties were obtained from [40] to emulate the breast fat and malignant tissue. However, in order to measure the dielectric properties of some materials such as oil, the Epsilon dielectric measurement device (Biox Epsilon model E100 manufactured by Biox System Ltd Company), has been employed. Although this device is capable to measure the isolated soft solid or liquid, it should be noted that this device is a free-frequency measurement instrument and gives the permittivity values calculated at frequency 0 Hz. Nevertheless it can be used for measuring the dielectric properties of some material with no changes in frequency variation such as oil. The Epsilon device and its performance will be explained in detail in the next sections.

Figure 3.9: Fabricated simple phantom consisting of sunflower oil and an inclusion.

The constructed phantom was placed in the centre of the turntable. Fig. 3.10 shows the fabricated phantom placed in the anechoic chamber.

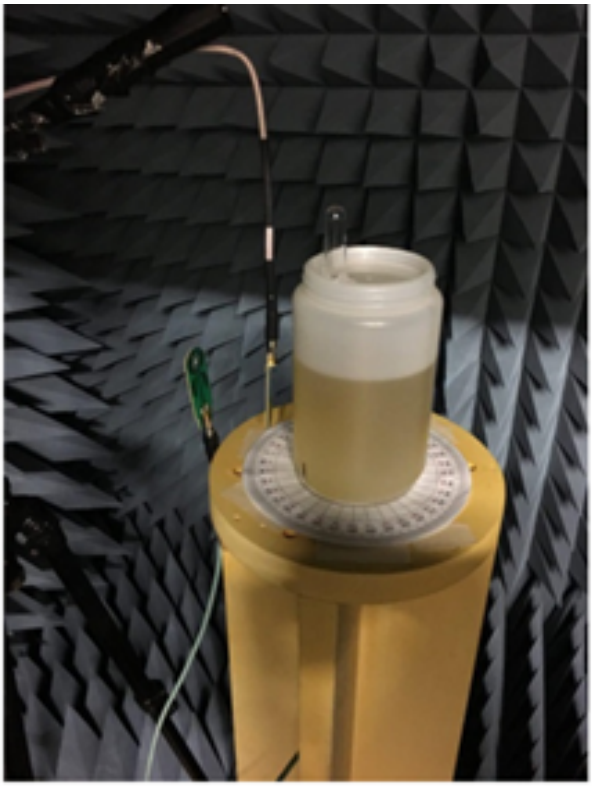

Figure 3.10: Position of the phantom inside anechoic chamber.

For each set of measurements, the phantom is illuminated with 6 transmitting line sources located at the distance of 10 cm away from the centre of the rotatable table whereas the receiving antenna is 6.5 cm away from the centre of the table and mounted on the computer-controlled rotating stage with 6° of angular resolution resulting in a total of N_{PT}=60 receiving point. The frequency range from 1 GHz to 10 GHz with the frequency step of 5.6 MHz is considered. For every separate frequency sample, and for every illuminating source, the receiving signal at 60 points on the external surface. The HP procedure is applied to the field $E^{\mathrm{known}}_{np,\mathrm{tx}_m}$ and the image is gained through eq. (3.13) by considering the total number of transmitting positions M= 6 (M=1, 2, . . . ,6). It should be noted that according to the measurements setup, in order to complete the measurements procedure for 6 transmitting positions, the phantom has been rotated instead of moving the transmitting antenna. The different positions of the transmitter are shown in Fig. 3.11.

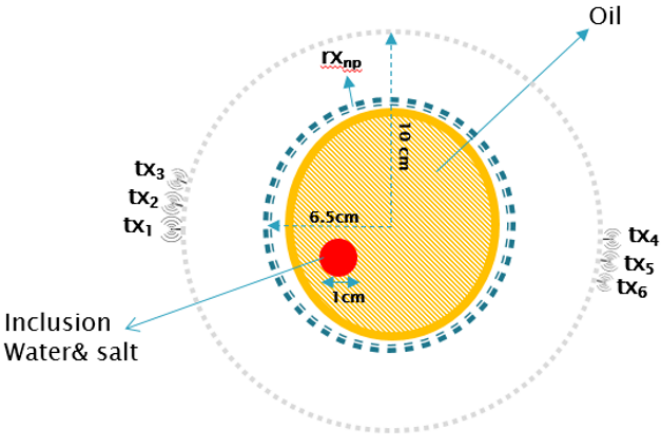

Figure 3.11: Pictorial view of the problem.

The microwave images are generated by applying eq. (3.13) through image processing based on HP using MATLAB Software (presented in the appendix). As Fig. 3.12 shows the peak is not observed in the obtained images when used the individual transmitting position. Although some peaks appear in the obtained images, they cannot be the inclusion. This phenomenon is called the artefact and could be the image of the transmitter that masks the region of interest preventing achieving the detection of the presence and location of the inclusion.

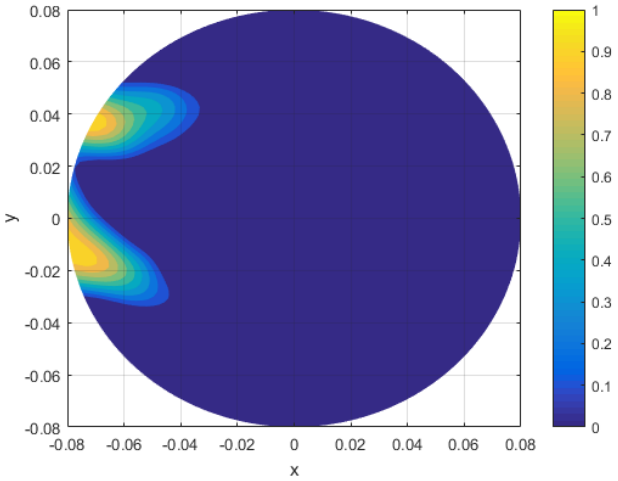

Figure 3.12: Normalised intensity of the obtained image, detection cannot be achieved; x and y are in meters.

Then the subtraction artefact removal method has been applied through eq. (3.14) to eradicate the artefact in the reconstructed images. Therefore, the peak representing the inclusion (tumour) could be observed and the detection is achieved in the final image as shown in Fig. 3.13.

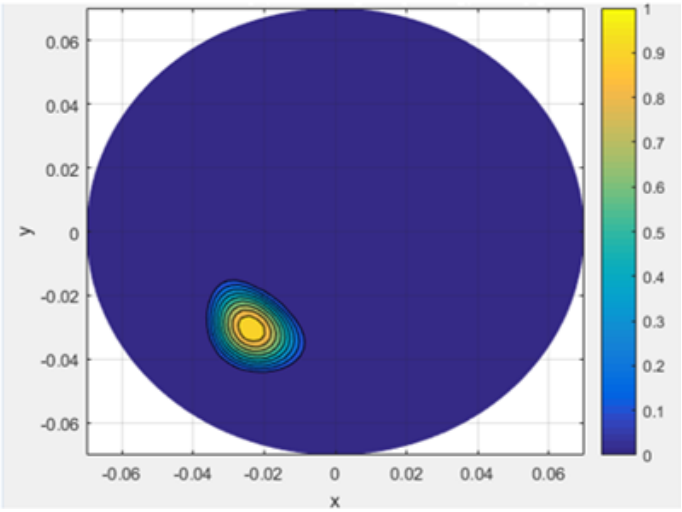

Figure 3.13: HP applied to the difference between two fields, linear normalised intensity obtained through eq. (3.4); x and y are in meters.

Eventually, according to the obtained images and successfully achieving the detection of inclusion, the validation of the proposed technique based on the HP has been performed. As a consequence, the presented results demonstrate the effectiveness of the proposed methodology to detect the presence and location of inclusion in the human tissue.

3.6 Measurements Procedure using MammoWave Microwave Apparatus

In the previous section, the results of phantom measurements inside the anechoic chamber approved the proposed methodology to detect the presence of the lesion inside the phantom. Now, this section discusses the verification of the MammoWave MWI device through phantom measurements.

3.6.1 Measurement Setup and Measurement Equipment

Recently, the MammoWave MWI novel device has been manufactured with the aim of breast cancer detection and has been verified through phantom measurements [98].

The MammoWave device collects all the microwave measured signals with the aim of generating the images through imaging processing based on the HP (the same algorithm mentioned in the previous section). The method is capable to capture the existing discrimination between different tissue and various conditions of tissues and illustrates this contrast in the final image. The HP technique is able to discover the presence and location of the considerable scatterer inside the volume which reveals the location of the lesion.

It should be noted that, for performing measurements using the MammoWave imaging device, the required hardware equipment is the same as that described in section 3.21 but in a different model with the following specifications: VNA is S5056, Copper Mountain model, two Antennas are Horn type and Vivaldi type antennas, and a PC.

Let's have a brief explanation of the MammoWave MWI device and its performance. MammoWave device is composed of the aluminium cylindrical hub having external diameter of 100 cm. Inside the cylindrical hub, there are two antennas that play the role of transmitting signals (tx) and receiving signals (rx) respectively. The transmitting antenna is the Horn type and the receiving antenna is the Vivaldi type having Voltage Standing Wave Ratio < 3. Moreover, one cup is mounted inside the hub for placing the phantom. Both antennas are placed at the same height in the free space (no matching liquid is required) and are able to gather all the reflected electromagnetic fields from various angular positions due to their capability of rotating around the azimuth. The transmitting and receiving antennas that can operate in a frequency band of 1-9 GHz are connected to a 2-port VNA (S5056, Copper Mountain, Indianapolis, IN) which operates up to 6.5 GHz. The MammoWave microwave device is illustrated in Fig. 3.14. More details can be found in [100].

Figure 3.14: Mammowave MWI device.

The measurement procedure is performed by recording the complex S21 in a multi-bistatic fashion, i.e. for 10 transmitting positions (tx_m), the receiving antenna is moved to measure the received signal every 4.5° leading to 80 receiving points (rx_{np}). It should be noted that the experiment is performed using a frequency range of 1-6.5 GHz, with 5 MHz sampling, employing 10 transmitting positions divided into 5 angular sections of 72°, centred at 0°, 72°, 144°, 216°, and 288°. Each section consists of 2 transmitting positions called doublets, and in each doublet, the two transmitting positions are displayed by 9°. Fig. 3.15 illustrates the configuration setup.

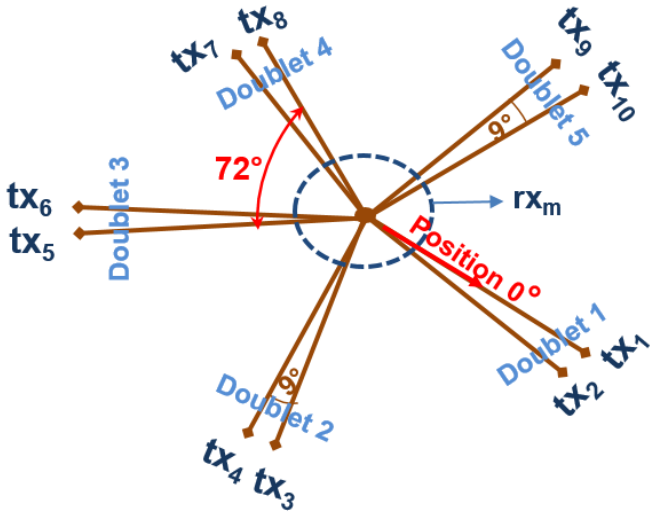

Figure 3.15: Mammowave measurements setup.

3.6.2 Validation of Proposed Imaging Algorithm through Phantom Measurements

Performing the phantom experiments using the MammoWave microwave device is exhibited to verify the ability of the HP-based MWI algorithm to detect the presence and location of the inclusion.

It is important to point out that, for developing the dedicated phantom to more realistic scenarios, an extremely thin tube (radius of 4 mm) is used as an inclusion. The phantom is built in two layers; the external layer is the cylindrical shaped plastic container with a height of 15 cm and a radius of 5.5 cm that is filled up with sunflower oil in order to mimic breast fat with the dielectric properties equal to 3.5 and conductivity equal to 0.34 S/m. The internal layer is the narrow tube as an inclusion with a height of 20 cm and a radius of 4 mm that is mounted inside the external container and filled up with a mixture of water and salt in order to mimic the malignant tumour with the dielectric properties of 80 and conductivity of 6.42 S/m.

For performing the set of measurements, first, the phantom is placed in the MammoWave device as shown in Fig. 3.16, a transmitting antenna tx_m illuminated the phantom through operating in the frequency range of 1-6.5 GHz.

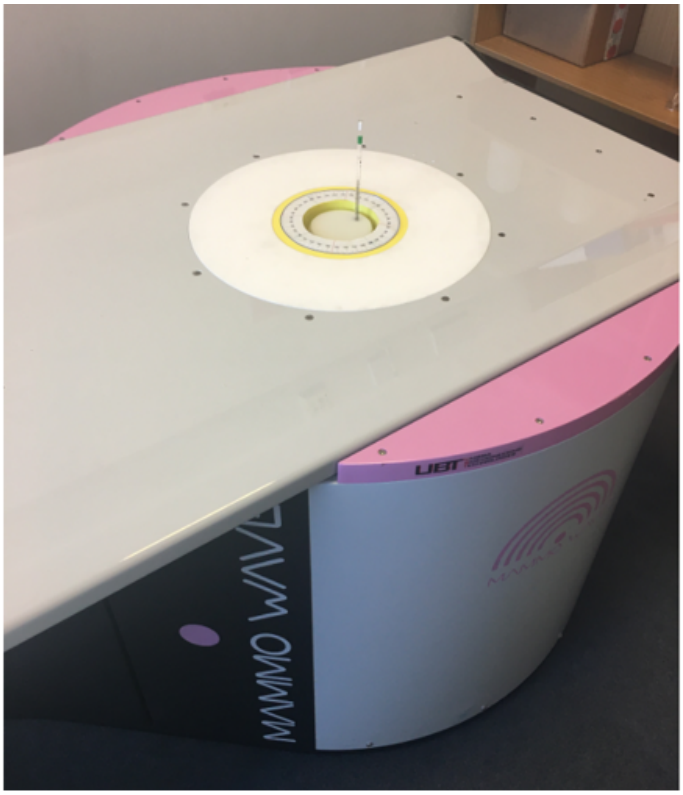

Figure 3.16: The phantom placed in the MammoWave device.

The complex S21 recorded by the VNA is processed using MATLAB Software running the proposed imaging algorithm based on HP [136] through employing eq. (3.13) to generate the final images (for more details refer to appendix). Fig. 3.17 shows the reconstructed image employing the individual doublet transmitting position.

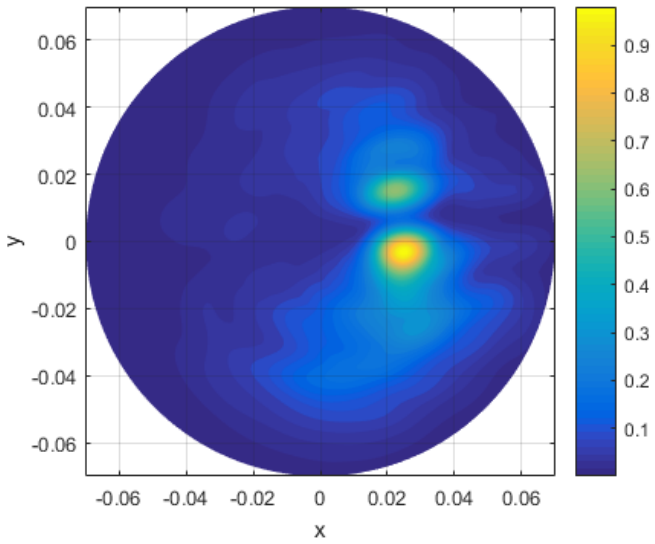

Figure 3.17: The obtained microwave image employing the individual doublet transmitting position; x and y are in meters.

Although, the inclusion can be almost observed, however, some artefacts could be noticed in the obtained image which can be eliminated by employing the combination of all the transmitting positions using the rotation subtraction artefact removal method.

Therefore, it should be highlighted that, since the 5 transmitting position doublets have been attended to complete the measurement procedure in the MammoWave measurement device, the intensity of the final images is given by the summation of different images corresponding to different transmitting doublets, each one obtained through the non-coherent summation of all frequency contributions. Accordingly, the combined image of 5 transmitting position doublets has been generated through the following equation, eq. (3.15) (N_F being the number of frequency samples) which leads to achieving the detection with a more effective artefact removal. By considering M transmitting sources varying from 1 to 5 and employing N_F frequencies f_i, the image intensity I could be derived by summing incoherently all the solutions. More in details, the intensity of the final images is given by the summation of different images corresponding to different transmitting doublets, and each one obtained through the non-coherent summation of all frequencies contributions (eq. (3.15)) [100].

$$\begin{aligned} I(\rho,\phi) &= \sum_{m=1}^{5} I(\rho,\phi;\mathrm{tx}_m - \mathrm{tx}_{m+1}) \\ &= \sum_{m=1}^{5}\sum_{i=1}^{N_F} |E^{\mathrm{rcstr}}_{\mathrm{HP,2D}}(\rho,\phi;\mathrm{tx}_m - \mathrm{tx}_{m+1};f_i)|^2 \end{aligned} \tag{3.15}$$

The HP procedure is applied to $E^{\mathrm{known}}_{np,\mathrm{tx}_m}$ and then the image is gained by considering the combination of 5 transmitting positions doublet after applying eq. (3.15) in order to eliminate the artefact. The rotation subtraction method has been performed for artefact removal by employing subtraction between the set of measurements obtained using two slightly displaced transmitting positions (positioned 4.5° apart on the circumference of the cylinder).The rotation subtraction strategy is explained mathematically as ($S21^{\mathrm{known}}_{np,\mathrm{tx}_{2m}}$ - $S21^{\mathrm{known}}_{np,\mathrm{tx}_{2m-1}}$) which presents the subtracting of the two adjacent transmitting positions, where 2m and 2m-1 correspond to the two adjacent transmitting positions in the same doublet (i.e. can be expressed as subtracting transmitting position m+1 from transmitting position m).

As shown in Fig. 3.18, using eq. (3.15) leads to generating an image where a peak can be undoubtedly detected in the correct location which was the exact region of the inclusion. Hence, detection and localization are achieved successfully using the combination of five transmitting position doublets.

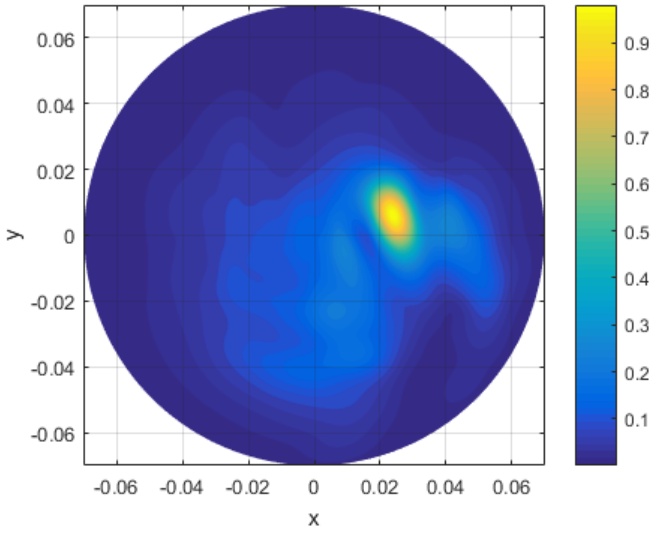

Figure 3.18: The obtained a microwave image employing the combination of the 5 transmitting position doublets; x and y are in meters.

The capability of the MammoWave device based on the HP imaging algorithm to detect the inclusion has been verified through the phantom experiment.

It is worthwhile to highlight that, the obtained microwave image using the proposed methodology gives us the image in arbitrary unit. It means that there is no physical meaning and this image is not representing the values of dielectric constant and conductivity. It is the map of homogeneity given in arbitrary unit. It is different from tomography, since tomography gives the values of dielectric constant and conductivity.

3.7 Summary/Conclusion

In this chapter, our methodology which is the MWI method based on the HP using the Green's function was presented.

Using the HP to forward-propagation the wave eliminates the need of resolving the inverse problem and accordingly no need for matrix generation/inversion. Along with its simplicity, capturing the contrast which comes from discrimination of various tissues or various conditions of tissues is one of the abilities of HP that is known as an advantage of this methodology. UWB provides an opportunity for all of the information in the frequency domain to be applied by combining the information from individual frequencies to create a consistent image.

A simple phantom has been modeled in a cylindrical shape to mimic the breast tissue consists of the fat tissue with a malignant tumour inside it. Fabricating the phantom has been done by considering the dielectric properties of each tissue. The dielectric properties of the human tissues considered in modelling the cylindrical phantom. The cylindrical

phantom has been used for the investigation of the proposed MWI procedure based on the HP. Validation of the technique has been performed through phantom measurements both in the anechoic chamber and also using a dedicated MammoWave imaging device to detect the location of tumour tissue inside the phantom.

It should be noted that, since the aim of this research is to investigate the capability of the MWI technique for diagnostic applications, so, validating the proposed imaging algorithm through phantom measurements using a dedicated imaging device is very important.

Initial measurement outcomes demonstrate the capability of the HP-imaging algorithm to produce the images. Moreover, the presented findings illustrate that using Green's function in the HP imaging algorithm makes it possible to detect the presence and positioning of considerable scatterers inside the cylindrical phantom. Consequently, verification of the HP-based MWI method and its effectiveness to detect the presence and location of the inclusion has been proven through performing the measurements in an anechoic chamber. Moreover, performing measurements using a dedicated MammoWave device not only has validated the MWI technique based on the HP but has also shown the feasibility of this technique to reach diagnostic applications.

The next three chapters of this thesis will focus on the extension of HP to more complex and realistic geometries. Multi-layered cylindrical phantoms will be investigated for skin cancer detection and bone lesion detection. In chapter 4, the possibility of MWI technique to detect the lesion inside the human forearm will be performing with the aim of skin cancer detection. Chapter 5 will be investigating the capability of the MWI technique for bone lesion detection. For this purpose, the two different scenarios of the bone lesion including the bone marrow lesion and bone fracture lesion will be investigated through phantom measurements in the anechoic chamber. Subsequently, chapter 6 will be discussing the applicability of the MammoWave MWI device to detect the bone lesion through phantom measurements. Moreover, the development of the phantom will be performing by considering a flat-shaped instead of cylindrically-shaped inclusion (a high-eccentric elliptical cross-section, i.e. flat-shaped).

Chapter 4

The Applicability of Microwave Imaging Technique to Skin cancer Detection

4.1 Introduction

This chapter investigates the feasibility of MWI-based on HP to detect a lesion inside the human forearm phantom mimicking skin cancer. Besides, the current chapter examines the extension of the HP to more complex and more realistic phantoms in terms of geometries. The human forearm phantom will be modelled in cylindrically- shaped having three layers. Afterward, a set of measurements will be performed in the anechoic chamber using the multi-layered human forearm phantom to check the ability of MWI for skin cancer detection.

This chapter is organized as follows: A brief overview of skin histology and skin cancer is presented in the next section. Then the procedure of modelling the human forearm will be discussed in detail. Further, the explanation of the experimental setup in the anechoic chamber, performing measurements using dedicated phantom, and also the procedure of generating the images will be presented. The last section belongs to the discussion and conclusion.

4.2 Human Skin Biology and Skin Cancer

The fundamental knowledge of human skin anatomy and the growth of the malignant skin tumour would be essential to understanding the interaction between the skin tissue and microwave signals. Designing the MWI system suitable for skin cancer detection will be not possible without adequate knowledge of the skin anatomy and malignant tumour.

For this reason, a very brief explanation of the skin anatomy and the malignant tumour is expressed in this section.

The human skin can be introduced as the largest organ in the whole body which contains 12% of the total weight of the body and between 18% to 40% of its water content. This organ is responsible to protect the body against environmental factors such as light, heat, injury, and infections. Moreover, controlling the temperature of the body, storing water, fat, and vitamin D are other responsibilities of this organ.

Although the skin itself does not possess a homogeneous nature, it is composed of several layers with different compositions and functions as shown in Fig. 4.1. Human skin consists of three layers including the epidermis, dermis, and hyperdermis.

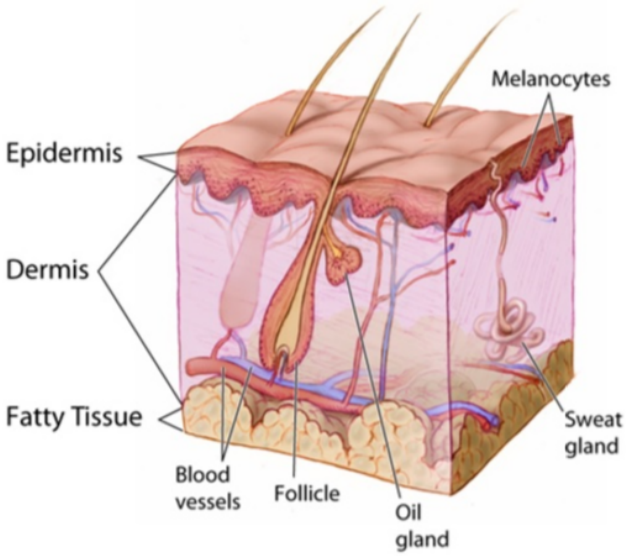

Figure 4.1: Human skin layers.

As mentioned in the literature, skin cancer occurs when uncontrolled growth happens in the skin cells and leads to unrepaired DNA damage of the skin cells and form a malignant tumour [140]. There are three kinds of skin cancers including basal cell carcinoma (BCC), squamous cell carcinoma (SCC), and malignant melanoma [73, 74]. Due to the fact that a considerable share of annual mortality rates results from cancer, it is important to address this issue and carry out the research to achieve an appropriate technique for detecting cancer in an early stage.

4.3 Microwave Imaging for Skin Cancer Detection

As mentioned previously, the characterisation of the tumour tissue is different from healthy tissue. One of the obvious differences between healthy tissue and tumour tissue is the increase in the amount of water inside the tumour tissue [56]. This difference in water

content leads to the variation of the different tissues' dielectric properties [56], [57]. It is a fact that the dielectric properties of human tissues can be utilized as an impressive and right indicator for diagnostic purposes [141]. The MWI technique uses the difference in dielectric properties between normal tissue and malignant tissue for cancer detection [142].

Concerning skin cancer, the high water content is observed notably in the epidermis layer that reaches up to 81% [110]. These variations in the water content lead to a change in the value of tissue's permittivity. Therefore, the observed contrast between normal and malignant skin tissue at microwave frequency range can be taken into account as a reason for proposing MWI to detect skin cancer.

Accordingly, this part of our research investigates the possibility of the MWI technique based on HP for skin cancer detection through phantom measurements as follows.

At the first, this study presents the design and fabrication of the multilayer heterogeneous phantoms having a lesion. The complex phantom consists of different layers of the human forearm tissue that simulates skin cancer. Then, the phantom measurements will be performing in the anechoic chamber using UWB microwave signals, and the S21 parameter is measured and collected. Afterward, the collected signals process through a proposed MWI algorithm based on HP, and then the images will be generated.

4.4 Human Forearm Phantom

4.4.1 Design of the Proposed Phantom

The phantom presented in this section has been designed for the UWB imaging experiments in a frequency range between 1 GHz to 10 GHz. The proposed phantom is simplified in a multilayer model so that each layer corresponds to a specific layer of human forearm tissue. The phantom is designed to be multilayer including the skin, bone, adipose, muscle, and tumour layers to simulate the human forearm phantom. To allow for the possibility of constructing, the proposed forearm phantom has been modelled in three layers of the skin, the combination of adipose & muscle and a cortical bone. Then the tumour is placed inside the combination of adipose & muscle layers to imitate the skin cancer.

It should be noted that different parameters demonstrate the characteristics of layers, among these, the dielectric constant of each layer is known as the most important parameter. Therefore, this parameter should be taken into account both in finding the appropriate recipes for each layer and in the construction of the phantom. Moreover, the similarity of the geometric characteristics of each layer of the phantom with the geometry of the desired human forearm has been considered and assessed. Besides, the stability of materials to keep the desired dielectric properties in the long-term is investigated. Ac-

cordingly, a specific recipe has been considered for each layer to simulate the dielectric parameters of human tissue.

As abovementioned, our proposed multi-layered phantom includes the following parts: i) skin layer, ii) layer of cortical bone, iii) a combination of adipose & muscle layer with a ratio of 50%-50%, and iv) the tumour layer.

The proposed phantom has been designed to be cylindrical shape to be geometrically matched to the real shape of the human forearm. Hence, in the designing of the phantom two concentric cylinders having different radii have been considered to construct the phantom where the inner cylinder holds the bone simulation material while the outer cylinder holds the combination of adipose & muscle simulation material. Another cylinder with a much smaller radius has been placed in the space between two cylinders as a tumour and surrounded by adipose & muscle. Figs. 4.2 (a) and (b) show the design of each layer of the phantom and proposed design of the human forearm phantom, respectively.

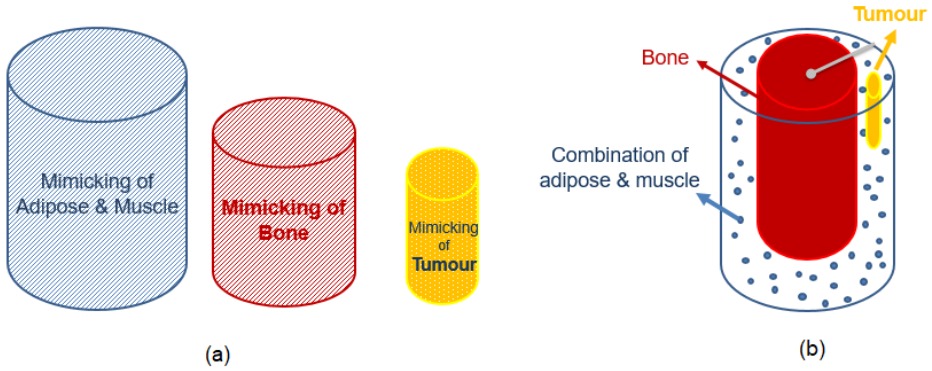

Figure 4.2: (a) Design of different layers of phantom, (b) design of the proposed human forearm phantom.

Subsequently, two different volumes of cylindrically-shaped plastic containers have been used for constructing the phantom. The cortical bone tissue-equivalent material and a combination of the adipose & muscle tissue-equivalent material have been used to fill them up to manufacture the cortical bone layer and a combination of adipose & muscle layer. A small plastic tube has also been used to fill up with tumour tissue-equivalent material to mimic a lesion/tumour in the human forearm phantom. Fig. 4.3 illustrates the cylindrically- shaped containers used in constructing the phantom. It should be noted that, in this research, the external plastic layer of the cylinder has played the role of the skin tissue layer.

The modelled phantom has been manufactured through the following steps. A plastic cylindrical tube with a radius of 0.7 cm and a height of 11 cm has been filled with the tumour equivalent material and inserted inside the adipose & muscle layer. The smaller

Figure 4.3: The used cylindrical shapes for constructing the proposed multilayer phantom.

cylindrical plastic container with a height and radius of 9 cm and 3.5 cm respectively, has been filled up with the bone tissue-equivalent material. Afterward, both the tumour and bone containers have been placed in the larger cylindrically shaped plastic container having a height of 13 cm and a radius of 5.5 cm, and the remaining space surrounding the tumour and bone has been filled with the adipose & muscle equivalent materials. Table 4.1 shows the phantom layer's design height and size.

Table 4.1: Phantom layers' design height and size

Tissue layers of the phantom	**Radius (cm)**	**Height (cm)**
Adipose & Muscle	5.5	13
Bone	3.5	9
Tumour	0.7	11

In the process of choosing tissue-equivalent material of the phantom, the bone layer has been considered to be solid, whereas a combination of adipose & muscle to be semi-solid, and the malignant tissue to be a liquid. The mixture of the constituent ingredients with the proper proportion has been employed for constructing each layer of the phantom. Moreover, the similarity in dielectric properties and the geometric characteristic of human tissue has been addressed in the process of the selection of the recipes.

4.4.2 Tissue Mimicking Forearm Phantom

As already mentioned, the microwave frequency is the principle of electromagnetic-based technologies. The interaction of microwave to the biological tissue caused the researchers to design biological phantoms with the properties imitating the real tissues' electrical

properties at microwave frequencies.

Accordingly, since the MWI works based on the dielectric properties, therefore, in this research, the phantom fabrication has been implemented by careful imitation of the electrical properties with the electrical properties of human tissues. The phantom has been fabricated in a realistic model in terms of its shape, dielectric properties, and geometric characteristics. It has also been considered to be cost-effective and to keep the stability of materials over a long time.

To achieve the goal, the phantom has been constructed by considering the following step.

1. Candidating suitable materials that seem to mimic the properties of the real tissue.
2. Measuring the dielectric constant of the material in the lab to choose ones that have a dielectric constant approximately same as the dielectric constant of real tissues.
3. Finalizing the appropriate materials.
4. Fabricating the phantom using the selected materials.

For the continuation of the work, various ingredients have been tested to find the materials suitable for emulating each layer of a phantom. The dielectric properties values of some materials have been measured using the Epsilon measurement device (the Epsilon device will be introduced in the following sections). The value of dielectric properties and conductivity of each layer at frequency 5.5 GHz (central frequency) have been collected in Table 4.2. The values are proximate to the realistic tissue, where the real values of the dielectric constant and conductivity of human tissue have been derived from [57].

Table 4.2: Dielectric constant and conductivity at the frequency of 5.5 GHz [57].

Microwave frequency (5.5 GHz)	**Permittivity**	**Conductivity (S/m)**
Bone (Cortical)	10	0.96
Adipose & Muscle	27	2.14
Tumour	50	3

- Measurement of the dielectric constant of materials to find the appropriate recipe

Relying on the results derived from the literature review and also based on the implemented experimental analysis, the development of the recipes corresponding to cortical bone, adipose & muscle layer, and tumour layer of phantom has been performed.

The assessment of material has been done to obtain tissue-equivalent materials for the cortical bone, adipose & muscle, and the tumour layers by considering the similarity of

dielectric properties with the dielectric properties of the human forearm tissues. Therefore, various materials have been analysed to find the most suitable candidate materials with the desired dielectric properties over the frequency range of 1-10 GHz.

Consequently, several recipes for tissue-equivalent dielectric properties have been derived from the candidate materials. Each of those recipes has been investigated to check whether they can keep the stability of dielectric properties for a long time.

Consequently, several recipes for tissue-equivalent dielectric properties have been derived from the candidate materials. Each of those recipes has been investigated to check whether they can keep the stability of dielectric properties for a long time. However, some of the recipes that had been nominated for simulating the layer of the phantom have been eliminated due to not keeping their stability over time. For instance, in some cases, the ingredients that participate in the recipes have been separated from the mixture, as shown in Figs. 4.4 and 4.5. Eventually, the best recipes corresponding to each layer of the forearm phantom have been measured with an Epsilon device after investigating its stability, to get finalized.

Figure 4.4: (a) Presents the investigation of various recipes mimicking cortical bone layer of the forearm phantom, (b) represents the unstable recipes.

4.4.3 Finalizing the Appropriate Recipe

Various recipes for tissue-equivalent dielectric properties have been tested to find the best one. Then, the best recipes have been tried more than twice to finalize the recipe corresponding to each layer. The permittivity properties have been measured more than three times and then the average values have been taken. The new Epsilon device has been used to measuring the permittivity of each recipe. The Epsilon device and its performance will be presented in detail in the next sections.

The recipe has been finalized when the measured value of permittivity derived from

Figure 4.5: Testing the recipe for muscle tissue.

the measurement device was in good agreement with the desired permittivity value given in Table 4.2.

Table 4.3 shows the final ingredients of appropriate recipes for the cortical bone, and the combination of adipose & muscle, since its recipe gives the correct dielectric constant value [143], [144].

Table 4.3: Tissue mimicking recipes; all the ingredients are given in grams.

Ingredient	**Bone**	**Adipose & Muscle**
Deionized water	10.5	-
Flour	50	30
Vegetable oil	30	25
Sugar	7.2	-
Salt	0.2	-
Detergent	-	12

4.4.4 Permittivity Measurement Device

The Epsilon Biox dielectric measurement device (Biox Epsilon Model E100 manufactured by Biox System Ltd Company) is used in the microwave laboratory for doing the measurements of dielectric properties of some materials. The Novel Epsilon permittivity measuring device is based on the fingerprint sensor for mapping near-surface dielectric permittivity (ε) of materials in contact with its sensing surface [145].

As Fig. 4.6 shows the device is composed of a base to mount the probe with its sensor surface horizontal and facing upwards. This device is capable of giving a controlled contact

Figure 4.6: Epsilon, dielectric constant measurement device.

with samples varying from 3 to 3.8 Newtons.

The instrument is calibrated using materials of known dielectric constant, to ensure consistent measurements from instrument to instrument and from time to time. It should be highlighted that the device does not give any information about conductivity.

After performing the calibration of the device and connecting it to the windows computer by a mini-USB socket, the absolute dielectric permittivity of the sample can be measured through the specific software [145].

A small sample of the prepared materials has been placed on the surface of the Epsilon device to measure the dielectric properties of each recipe. The corresponding permittivity value of the sample appears on the screen, in the ROI (Region of Interest) area (seeFig.4.7).

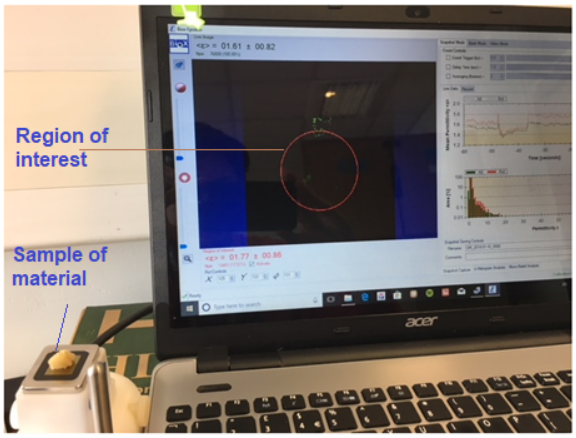

Figure 4.7: Photo of the permittivity measurement device and related software.

4.4.5 Phantom Construction Method

The fabrication method for our proposed multilayer forearm phantom is described as follows:

The required ingredients for emulating the cortical bone tissue are including flour, vegetable oil, sugar, salt, and deionized water with different ratios in grams (amounts

given in Table 4.3) which have been weighted by digital scale. Fig. 4.8 is the photograph of using a digital scale for weighing the ingredients.

Figure 4.8: Digital scale used for weighing the ingredients.

For preparing the cortical bone equivalent material, at first, 30 gr vegetable oil has been mixed with the 50 gr flour and stirring for 10-15 minutes until all the oil was absorbed by the flour and the uniform mixture has been obtained. In the separate bowl, 7.2 gr sugar is mixed with 10.5 gr of deionized water, continued to stir until the sugar was dissolved in the water. The solution of water and sugar is then added to the mixture of flour and vegetable oil and mixed using the electric mixer until the uniform shaped obtained. The final mixture forms the emulation of the cortical bone.

To emulate the combination of adipose & muscle tissue equivalent material, 30 gr flour is added to the 25 gr vegetable oil and mixed. Then 12 gr detergent (washing up liquid) is added to them to prevent the oil from separating from the mixture. Then the mixture is put inside the fridge overnight.

Finally, the tumour tissue-equivalent material is emulated by using 60% glycerol, and 40% water [146]. The mixture is stirred using an electric mixer for a specific time to make sure that the material was mixed completely.

Fabrication of the forearm phantom was done after preparing the final recipe for each layer corresponding to the real forearm tissues. For this purpose, the small cylindrically shaped plastic containers and the plastic tube have been filled up with the prepared bone equivalent materials and tumour-equivalent materials, respectively. Then both bone and tumour have been placed inside the larger cylindrically-shaped plastic containers and the adipose & muscle-equivalent material has been poured around them to fill it without any remaining space (as shown in Fig. 4.9). Then the fabricated forearm phantom has been ready for measuring in the anechoic chamber.

4.5 Measurements in Anechoic Chamber

As explained previously, frequency-domain UWB measurements have been performed in an anechoic chamber using a VNA arrangement to obtain the transfer function (S21)

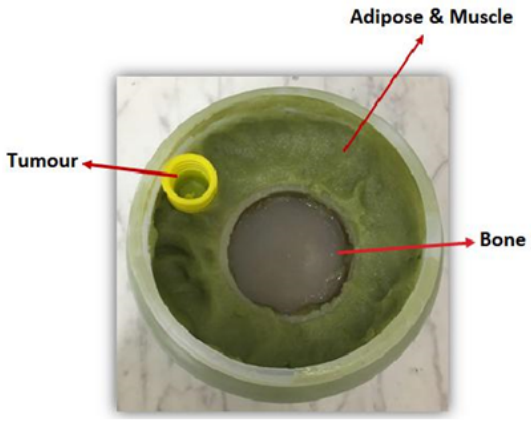

Figure 4.9: Human forearm fabricated phantom.

between two antennas. PULSON antennas, vertically polarized, and Omni-directional in the azimuth plane have been used in free space, after calibration. The phantom has placed in the centre of a rotatable table. Fig. 4.10 shows the fabricated phantom placed inside the anechoic chamber. To exploit the variation of signals at different frequencies, the complex S21 values have been recorded over a wide frequency range of 1-10 GHz, employing a frequency step of 5.6 MHz. For each set of measurements, the transmitting antenna has been fixed at approximately 10 cm away from the centre of the table whilst the position of the receiver antenna has been considered 6.5 cm away from the centre of the table and mounted on a computer-controlled rotating stage with 6 degrees of angular resolution (number of points: 60).

The procedure has been repeated for 6 transmitting positions, divided into 2 triplets displaced at 0°, and 90°; each triplet contains 3 transmitting position displaced 5° from each other such that the first triplet includes positions 0°, 5°, and 10° while the second triplet includes positions 90°, 95°, and 100°. Note that, rather than moving the transmitting antenna, the 6 transmitting positions have been synthesized by appropriately rotating the phantom. Fig. 4.11 shows the measurement setup diagram and the position of the phantom to the transmitting position of 0°.

4.6 Image Reconstruction Procedure

As mentioned previously, the measured signals, i.e., the complex S21 of the VNA, have been processed through the HP imaging algorithm by applying eqs. (3.9), (3.13), and (3.14) which have been extensively explained in chapter 3. The robust MATLAB Software has been implemented for the imaging procedure. The explanation of the Software

Figure 4.10: The position of the phantom inside the anechoic chamber.

algorithm using MATLAB and its block diagram are demonstrated in the appendix.

To remind the readers, the Huygens mathematical relations for reconstructing the internal field, obtaining the intensity of the final image, and removing the artefact, are recounted below.

- Reconstructing the internal field (eq. (3.9))

$$E^{\text{rcstr}}_{\text{HP,2D}}(\rho,\phi;\text{tx}_m;f) = \Delta s \sum_{np=1}^{N_{PT}} S21^{\text{known}}_{np,\text{tx}_m} G(k_1|\overrightarrow{\rho}_{np} - \overrightarrow{\rho}|)$$

- Obtaining the intensity of the final images (eq. (3.13))

$$I(\rho,\phi) = \sum_{i=1}^{N_F} |E^{\text{rcstr}}_{\text{HP}}(\rho,\phi;\text{tx}_m;f_i)|^2$$

- Removing the artefact (eq. (3.14))

$$E^{\text{rcstr}}_{\text{HP,2D}}(\rho,\phi;\text{tx}_m;f) = \Delta s \sum_{np=1}^{N_{\text{PT}}} \left(S21^{\text{known}}_{np,\text{tx}_m} - S21^{\text{known}}_{np,\text{tx}_{m'}} \right) G(k_1|\overrightarrow{\rho}_{np} - \overrightarrow{\rho}|)$$

It has been shown in [126], [136], and [139] that HP can identify the presence and location of the dielectric discontinuities inside an object by using only the outside field measurement. The next section discusses the results of investigating skin cancer detection

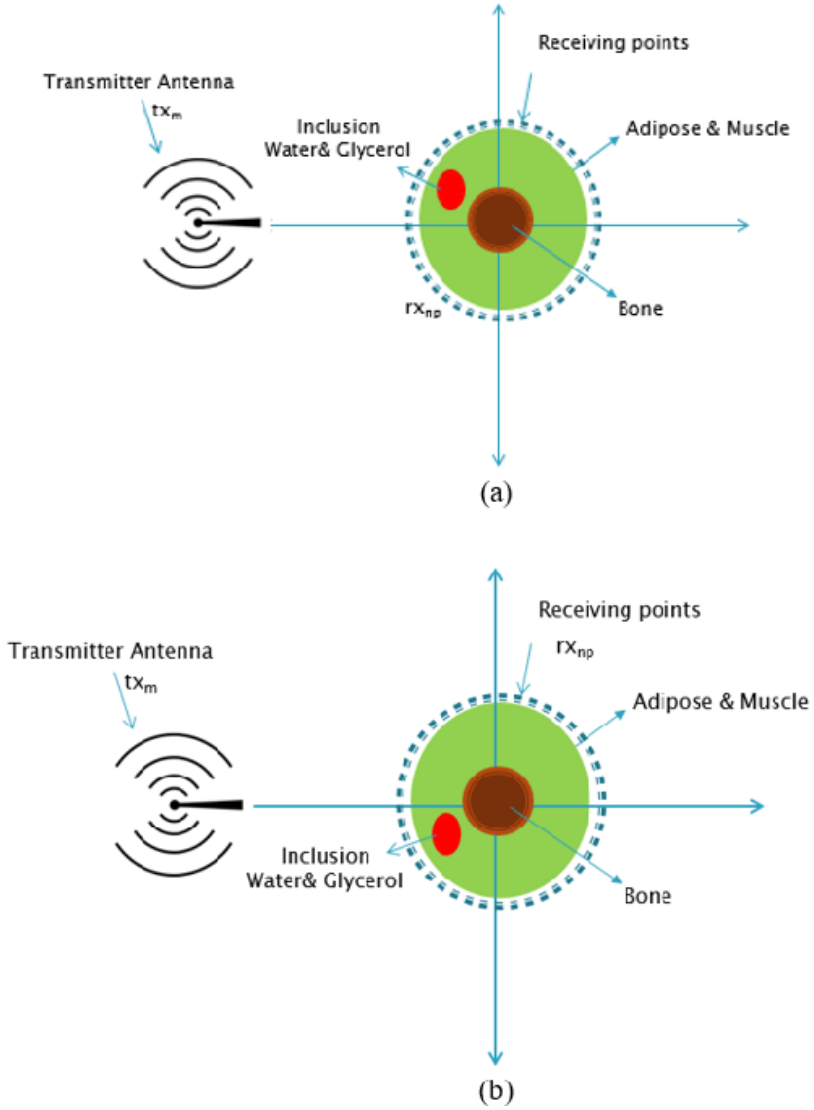

Figure 4.11: Pictorial view of the measurement setup for first triplet (a) and second triplet (b).

using HP.

4.7 Results & Discussion

4.7.1 Permittivity Measurements Result

The permittivity of the proposed recipe for each layer of the phantom has been measured by placing a small sample of the material on the surface of the Epsilon device. The permittivity of the bone equivalent material's sample and also the combination of adipose & muscle equivalent-material samples are measured using the Epsilon device. The photograph of the samples under test is shown in Fig. 4.12.

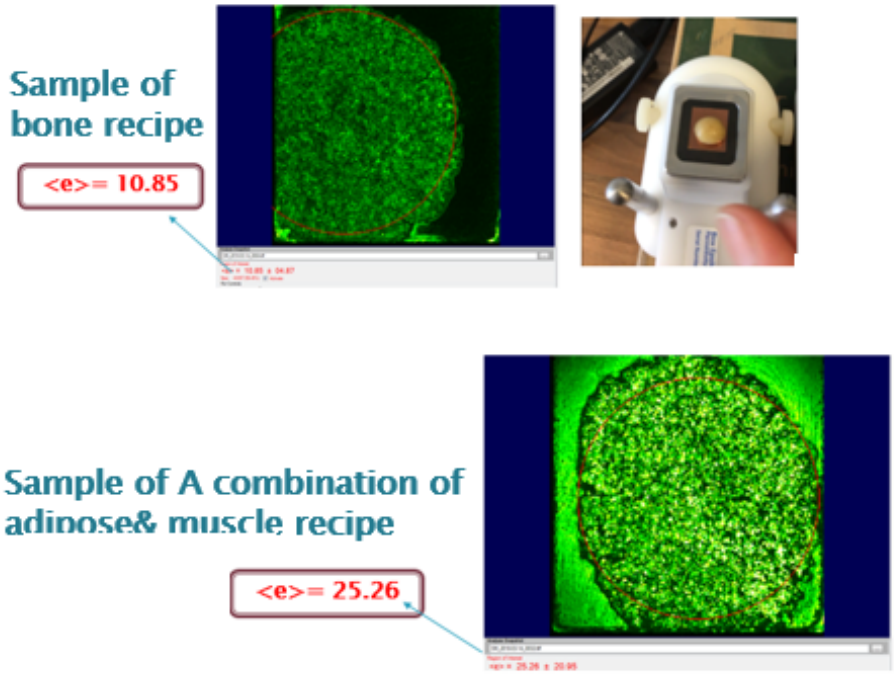

Figure 4.12: The photograph of sampling measurements using Epsilon device.

The recipe for each layer was finalized when the obtained value of the permittivity was very close to the real permittivity value of human tissue (previously shown in Table 4.2). The obtained permittivity values of the final recipe for each layer of phantom have been collected in Table 4.4.

As can be observed from the results, an excellent agreement was found between the values given in Table 4.4 and the corresponding values given in Table 4.2. It is important to highlight that the measurement device does not give the dielectric value at the frequency of the interest but gives the permittivity value at a frequency of 0 Hz. However, it is still suitable for recipes that consist of ingredients that do not experience any change with

Table 4.4: Obtained permittivity for each layer of the phantom.

Layer of phantom	**Our recipe's permittivity value**
Bone	10.85
Adipose & muscle	25.26
Tumour	51.70

frequency variation such as oil and flour. Accordingly, since the combination of adipose & muscle and bone recipes are constructed mainly by a high percentage of oil and flour, therefore, the obtained measured permittivity with this device at zero frequency has been considered equivalent to its permittivity at a frequency of 5.5 GHz. This does not hold true for glycerol and water mixture [146], however, the permittivity of such mixture can be derived from [146], where the conductivity is also given.

4.7.2 Obtained Microwave Images

The microwave images of skin phantom measurements have been generated by using the MWI based on HP algorithm. The microwave images of the skin phantom when employing eq. (3.9) for the first triplet in different individual transmitting positions of 0°, 5°, and 10° have been shown in Figs. 4.13(a), 4.13(b), and 4.13(c), respectively. As obtained images show for each transmitting position, the artefact has masked the region of the inclusion and no detection achieved. The artefact can be assumed to be the image of the transmitter antenna or the skin layer reflection.

In contrast, Figs. 4.13(d), 4.13(e), and 4.13(f) illustrate the obtained microwave images after applying the artefact removal procedure through employing eq. (3.14), i.e. using the difference between measurements obtained with transmitting positions 0° and 5°, 5° and 10°, 0° and 10° respectively. As Figs. 4.13(d), 4.13(e), and 4.13(f) depict, the inclusion is now clearly detectable in the correct position. In addition, since the peak in Figs. 4.13(d), 4.13(e), and 4.13(f) are observed in the same position, we can conclude that it is not an artefact.

Figure 4.14 refers to the second triplet and confirms the previous results. It means that the obtained images correspond to the individual transmitting position of 90°, 95°, and 100° which have been shown in Figs. 4.14(a), 4.14(b), and 4.14(c) respectively, proving that the image of the transmitter antenna has masked the region of the inclusion. However, after employing eq. (3.14) to remove the image of the transmitter, as indicated in Figs. 4.14(d), 4.14(e), and 4.14(f), the detection of the presence and location of the inclusion has been successfully achieved. Specifically, the inclusion shown in Figs. 4.14(d), 4.14(e), and 4.14(f) appears here with a 90° rotation to Figs. 4.13(d), 4.13(e), and 4.13(f). This is

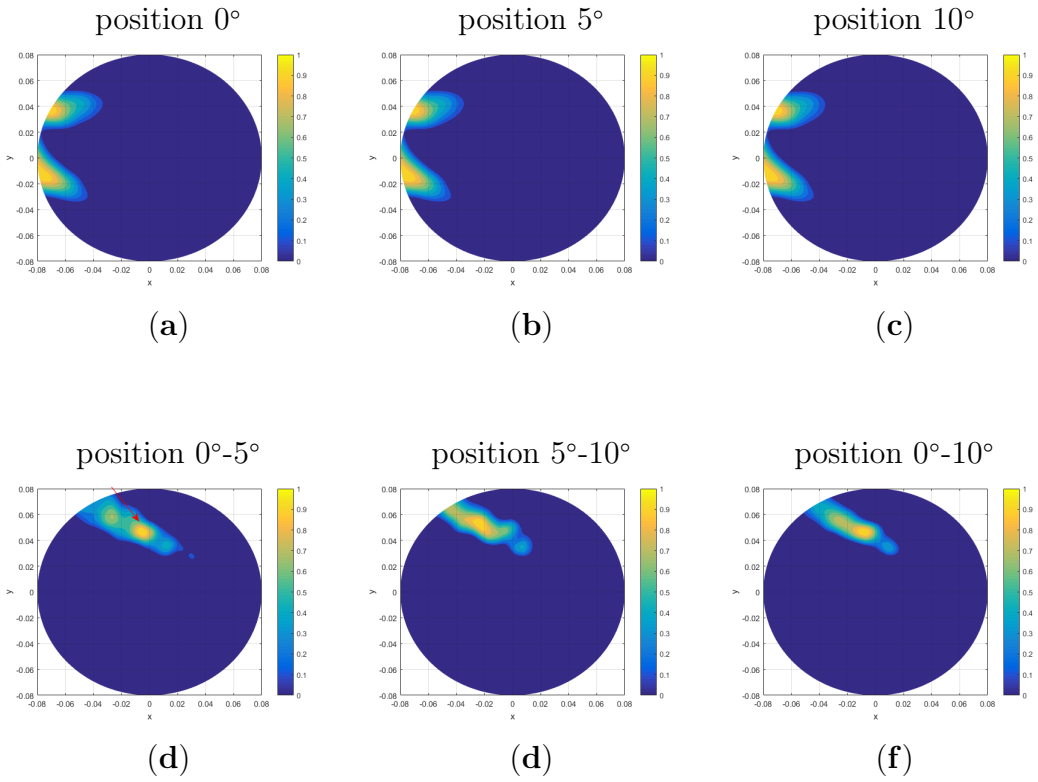

Figure 4.13: Obtained microwave images for skin cancer using individual transmitting position in the first triplet, following normalization to their correspondent maximum values and forcing to 0 the intensities below 0.5 (x and y are given in meters.)

in agreement with our experiments since the transmitting positions have been synthesized by appropriately rotating the phantom.

4.8 Summary/Conclusion

In this chapter, the proposed MWI procedure based on the HP has been introduced which achieved promising results for skin cancer detection. It has been indicated that the MWI technique based on the HP permits the detection of the presence and location of the considerable scatters inside a cylindrically-shaped skin phantom.

In the present chapter, the development of a realistic human forearm phantom for skin cancer detection has been described. We have fabricated a phantom using dedicated recipes mimicking layers of cortical bone, adipose & muscle, and a lesion as a cancerous tumour. The combination of adipose & muscle has been considered here using a ratio of 50%-50%; future research will be focused on the development of other phantoms that would realize the different combinations of adipose & muscle, analysing the impact of the combined ratio in tumour detection. Various recipes were tested for tissue-equivalent dielectric properties and the final recipes have been selected by considering the similarity

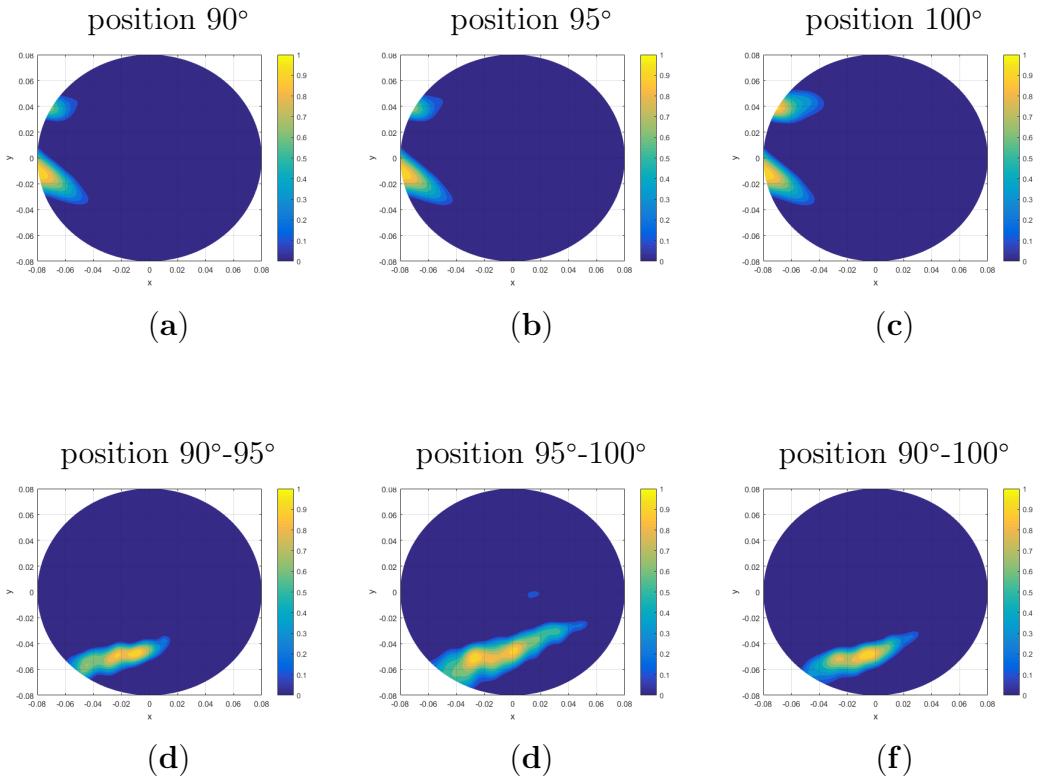

Figure 4.14: Obtained microwave images for skin cancer using individual transmitting position in the second triplet, following normalization to their correspondent maximum values and forcing to 0 the intensities below 0.5 (x and y are given in meters).

of its dielectric properties with the human tissues.

The phantom was then used for UWB experiments and after that, the collecting data processed through an imaging algorithm based on HP in MATLAB Software. The detection of the tumour has been achieved after removing the artefacts, i.e. the images of the transmitter, through employing a subtraction between S21 obtained using two sets of measurements.

Subsequently, the capability of MWI based on HP to detect and locate a skin cancer type inclusion in a multilayer cylindrical phantom was verified.

This research is in progress to show the performance of the HP procedure in the case of the complex multi-layered phantom to investigate the ability of this method in other diagnostic applications such as bone lesion detection.

Chapter 5

The Possibility of Microwave Imaging Technique for Bone Lesion Detection (Anechoic chamber)

5.1 Introduction

In the previous chapter, the proposed MWI technique based on HP was employed to investigate skin cancer detection through phantom measurements in an anechoic chamber. The multilayer phantom was fabricated using equivalent materials to mimic the real tissue of the human forearm. In modelling the phantom, the differences in dielectric properties between healthy and malignant tissues led to contrast in the region of the transition of two media, and this mismatch was captured by the HP method. The set of phantom measurements was performed in an anechoic chamber and the detection of inclusion was achieved in the generated images after applying the HP imaging procedure.

Therefore, the previous chapter indicated that the HP procedure permits the detection of the significant scattered inside the cylindrical forearm phantom and leads to achieved tumour detection in the skin cancer scenario.

This chapter covers the extension of the HP technique to more realistic geometries constituting multiple-layer phantom with the aim of bone lesion detection. The feasibility study of the MWI procedure based on the HP for bone lesion detection is presented in this chapter. For this purpose, two scenarios including bone fracture lesion, and bone marrow lesion are investigated through phantom measurements.

Specifically, a realistic multilayer bone phantom comprised of cortical bone mimicking and bone marrow mimicking layers is constructed. Subsequently, a large inclusion is placed within the marrow layer to represent the bone marrow lesion, and afterward, a small inclusion is placed in the cortical layer to represent the bone lesion or bone fracture. The identification of the lesion's presence in different bone layers will be investigated on

images that will be derived after processing through the HP.

Explicitly, S21 signals in the frequency range of 1–3 GHz [16] will be collected in a multi-bistatic fashion in an anechoic chamber setting using a multilayer phantom, emulating bones. Angular subtraction rotation will be used for artefact removal, allowing lesion detection.

Additionally, quantification of the images obtained through HP MWI will be performed by introducing dedicated parameters such as the resolution and S/C. Furthermore, investigating the impact of different frequencies and bandwidths, lesion size and angular rotation subtraction in the detection procedure will also be addressed.

This chapter is organized as follows. A brief overview of bone lesion disease, the current diagnostic imaging methods for bone lesion detection with their limitations will be demonstrated in the next section. Then the procedure of designing and modelling the bone lesion phantom will be discussed in detail. Afterward, the experimental configuration in the anechoic chamber, performing measurements using dedicated phantom, and also imaging procedure and imaging quantification will be explained in the following section. Then the next section will be focused on the result, discussion, and concentrates on improving the artefact removal. The last section belongs to the conclusion/summary.

5.2 Bone Lesion Diseases and Current Bone Imaging Methods

Bone fracture can be caused as a result of high force impact, a simple accident, stress, or certain medical conditions that weaken the bones. The structure of the bones includes two principal parts: (i) cortical (compact) bone, which is a hard outer layer and is dense, strong, durable, and surrounded by the cancellous tissue, and (ii) bone marrow, which is the inner layer, less dense and with lighter content. There are many types of bone fractures [147]. Depending on the fracture severity, the injuries can lead to a reduction in the mobility of the patient [148]. X-rays, computed tomography (CT), and magnetic resonance imaging (MRI) are used as essential tools in the diagnosis and monitoring of bone conditions, including fractures, and joint abnormalities [23]. However, each technique suffers from its negative aspects. For instance, fractures can be commonly detected by X-rays [149], which is the fastest and easiest way to assess bone injuries, including fractures. However, since this technique involves radiation and can potentially cause damage, it raises major concerns especially in the cases of infants and stages of pregnancy. Besides, X-rays provide limited information about muscles, tendons, or joints [6]. Nevertheless, CT is very effective for imaging and gives better quality images for body organs, such as an image of complicated fractures, subtle fractures, or dislocations. However, similar to

X-rays, ionizing radiation is the major problem of using this technique, which leads to limits in its application [24]. There is no ionizing radiation in the MRI technique, and it may be more useful in identifying bone and joint injuries. MRI can also detect occult fractures or bone bruises that are not visible on X-ray images, but the high cost of purchasing and maintaining such systems and their long time duration cause restrictions. Moreover, none of these devices are portable and cannot be used at the accident site. As mentioned in the literature, a fast and portable imaging system could be particularly useful locally for the rapid diagnosis of bone injuries. Therefore, this research investigates the possibility of the MWI method for bone lesion detection through phantom measurements.

5.3 Design and Fabrication of Multilayer Human Bone Lesion Phantom

This section presents the design and fabrication of a multi-layered cylindrical phantom simulating the human bone by considering the relative permittivity and conductivity to perform MWI experiments in the frequency range of 1 to 3 GHz. Hence, our proposed multi-layered bone phantom has been comprised of two layers, which included: (i) an external layer representing the cortical bone tissue (radius = 5.5 cm) and (ii) an internal layer representing the bone marrow tissue (radius = 3.5 cm). A small size inclusion (radius = 0.3 cm) is placed in the cortical bone layer to represent the bone fracture, and a larger sized inclusion (radius = 0.7 cm) is placed in the bone marrow layer to represent the internal bone lesion. In this research, the lesion was assumed to have the dielectric properties of blood.

The fabrication procedure for each layer of phantom has been performed by considering the following factors: (i) dielectric property (permittivity and conductivity) similarity of the layers with the tissues to be mimicked, (ii) an easy construction process, (iii) the stability of the materials and (iv) the geometric dimension similarity between each layer and the realistic scenario. The upper half of Table. 5.1 shows the dielectric properties of each tissue to be imitated, where the values were derived from [57], while the lower half of the Table indicates the dielectric properties of the tissue-emulating materials used.

To construct the multi-layered bone phantom appropriately, different volumes of cylindrically shaped plastic containers and tubes have been used and are shown in Fig. 5.1.

Table 5.1: Relative permittivity and conductivity at a frequency of 2 GHz.

	Relative permittivity	**Conductivity (S/m)**
Bone marrow	5.35	0.07
Bone cortical	11.7	0.31
Lesion (assumed here as blood)	59	2.19
Bone marrow tissue equivalent material (ZMT Zurich MedTech Company, TLec24 oil)	5	0.2
Bone cortical tissue equivalent material (ZMT Zurich MedTech Company, TLe11.5c.045 oil)	7	0.3
Blood tissue equivalent material (40% glycerol and 60% water)	60	2

Figure 5.1: Design of the different layers of the phantom.

As shown in Table 5.2, the phantom fabrication has been performed using a large cylindrically shaped plastic container with a radius of 5.5 cm and a height of 13 cm filled with cortical bone equivalent material to represent the cortical bone layer. Then, a medium-sized cylindrically shaped plastic container with a radius of 3.5 cm and a height of 9 cm has been placed inside the large container after filling it up with bone marrow equivalent material representing the bone marrow layer. Subsequently, the small cylindrically shaped plastic tube with a radius of 0.3 cm and a height of 13 cm filled up with lesion equivalent material has been placed inside the cortical bone layer to represent bone fracture (see Fig. 5.2(a)). In the next scenario, the larger cylindrically shaped plastic tube having a radius equal to 0.7 cm and a height equal to 11 cm, again filled up with lesion equivalent material, has been placed inside the bone marrow layer to represent bone marrow lesion (see Fig. 5.2(b)).

Table 5.2: Phantom layer's design height and size.

Different layers of the phantom	**Radius (cm)**	**Height (cm)**
Bone marrow (internal layer)	3.5	9
Bone cortical (external layer)	5.5	13
Small lesion	0.3	13
Large lesion	0.7	11

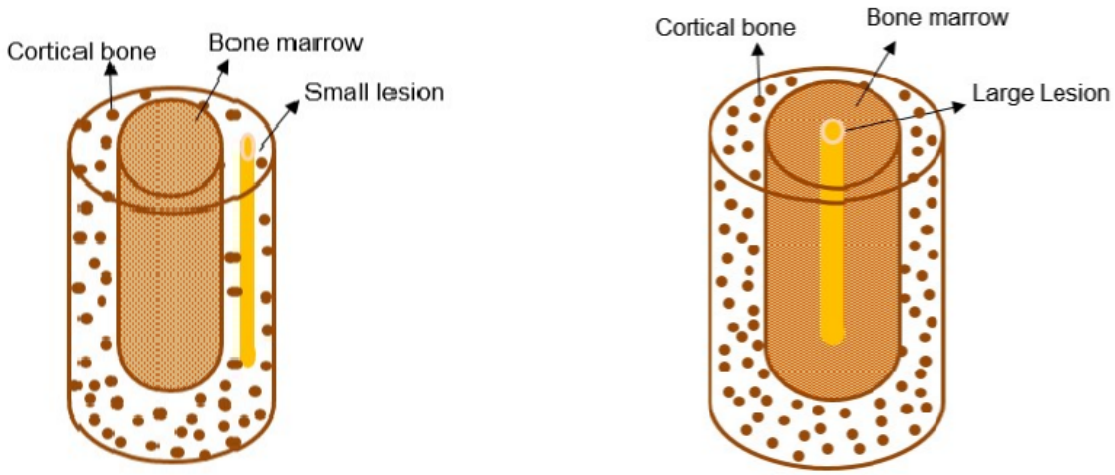

(**a**) (**b**)

Figure 5.2: Design of the proposed bone fracture (**a**), and bone marrow lesion (**b**).

Different recipes for each layer of the phantom were tested to select those showing dielectric properties similar to those given in the upper half of Table 5.1. In this context, dedicated liquids have been purchased from the ZMT Zurich MedTech Company [150]. As shown in the lower half of Table 5.1, the TLe11.5C.045 oil displayed (at 2 GHz) a dielectric constant of 7 and a conductivity of 0.3 S/m; the Tle5C24 displayed (at 2 GHz) a permittivity of 5 and a conductivity of 0.2 S/m. Thus, TLe11.5C.045 was selected as a cortical bone tissue-equivalent material and Tle5C24 as a bone marrow tissue equivalent material. In addition, a mixture of glycerol and water with a ratio of 40% and 60%, respectively, was chosen as the recipe mimicking the lesion (blood), giving (at 2 GHz) a permittivity value equal to 60 and conductivity of 2 S/m [146]. Figs. 5.3(a), 5.3(b) show the fabricated multi-layered bone fracture and bone marrow lesion, respectively.

(**a**) (**b**)

Figure 5.3: Fabricated bone fracture phantom (**a**), and bone marrow lesion phantom (**b**).

5.4 Experimental Configurations in an Anechoic Chamber

All microwave images presented in this chapter have been obtained by processing the frequency domain measurements obtained in the band of 1 to 3 GHz. Measurements have been performed inside an anechoic chamber using a VNA (model MS2028C, Anritzu) and PulsON P200 antennas. Specifically, the measurement setup was comprised of one transmitting antenna and one receiving antenna connected to the VNA device. The phantom was placed at the centre of a rotatable table. The transmitting antenna was located 12 cm away from the centre of the table, while the receiving antenna was placed nearer to the object (i.e., 8.5 cm from the centre of the table). Both receiving and transmitting antennas were vertically polarized and omni-directional in the azimuth plane and were calibrated and operated in free space.

The receiving antenna has been configured to rotate azimuthally around the phantom to collect the reflected signals in different directions. For each receiving position, the complex S21 has been recorded over a wide frequency range of 1 to 3 GHz with a frequency step of 10 MHz [98] to exploit the variation of the signal over the different frequencies. To allow artefact removal, the measurement procedure has been repeated using 3 transmitting positions displaced 5° from each other (considered as a transmitting triplet displaced at positions 0°, 5°, and 10°). It should be pointed out that the 3 transmitting positions were synthesized by appropriately rotating the phantom instead of rotating the transmitting antenna. For each transmitting position, the receiving antenna rotated to measure the receiving signal every 6°, which led to a total of 60 receiving points. Fig. 5.4 shows the measurement setup of the multi-layered bone phantom inside the anechoic chamber.

It should be pointed out that according to experiments' setup in the anechoic chamber, since the distance between transmitter and receiver antennas varies from the minimum of 3.5 cm to the maximum of 20.5 cm, and the maximum dimension of the antenna is 6 cm, by applying eq. (3.5), eq. (3.6), and eq. (3.7), can be concluded that almost all the measurements were performed under the far-field region.

Figure 5.4: Position of the bone marrow lesion phantom inside the anechoic chamber. The phantom was placed in the centre of a rotatable table. The external PulsON P200 antenna is the transmitter, and the internal PulsON P200 antenna is the receiver.

The positions of the phantoms concerning to the transmitting antenna are shown in Figs. 5.5(a), 5.5(b), which represent the pictorial views of the measurement setup.

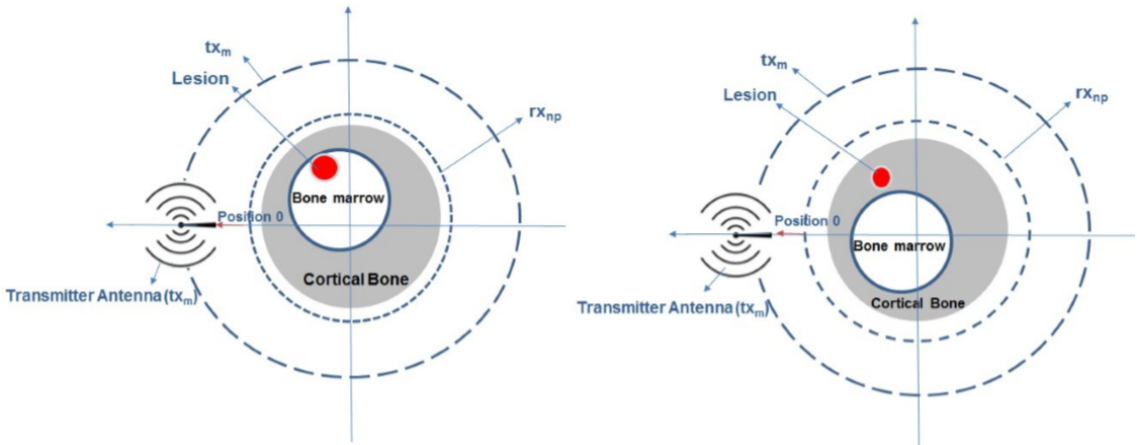

(**a**) (**b**)

Figure 5.5: Pictorial view of bone marrow lesion (**a**), and bone fracture lesion (**b**) measurement setups.

5.5 Imaging Procedure and Image Quantification

To reconstruct the image, the complex measured S21 has been processed through HP imaging algorithm [136] using MATLAB Software which completely explained in chapter 3. The Software part of the imaging algorithm and its block diagram is presented in the appendix.

However, the Huygens mathematical relations for reconstructing the internal field, obtaining the intensity of the final image, and removing the artefact, are recounted below.

- Reconstructing the internal field (eq. (3.9))

$$E^{\text{rcstr}}_{\text{HP,2D}}(\rho,\phi;\text{tx}_m;f) = \Delta s \sum_{np=1}^{N_{PT}} S21^{\text{known}}_{np,\text{tx}_m} G(k_1|\overrightarrow{\rho}_{np} - \overrightarrow{\rho}|)$$

- Obtaining the intensity of the final images (eq. (3.13))

$$I(\rho,\phi;\text{tx}_m) = \sum_{i=1}^{N_F} |E^{\text{rcstr}}_{\text{HP}}(\rho,\phi;\text{tx}_m;f_i)|^2$$

- Removing the artefact (eq. (3.14))

$$E^{\text{rcstr}}_{\text{HP,2D}}(\rho,\phi;\text{tx}_m;f) = \Delta s \sum_{np=1}^{N_{\text{PT}}} \left(S21^{\text{known}}_{np,\text{tx}_m} - S21^{\text{known}}_{np,\text{tx}_{m'}} \right) G(k_1|\overrightarrow{\rho}_{np} - \overrightarrow{\rho}|)$$

More details can be found in [126], [136]. However, it should be highlighted that all the abbreviations used within this formula have been extensively explained in chapter 3.

- Image Quantification

Images may contain some clutter even following artefact removal procedures. Thus, it is appropriate to introduce and calculate two parameters S/C and resolution to compare and quantify the performance of MWI. Specifically, the resolution is defined as a dimension of the region whose normalized intensity is above 0.5 [126]; S/C was defined as the ratio between maximum intensity evaluated in the region of the lesion divided by the maximum intensity outside the region of the lesion [35]. The evaluation of these parameters has been performed for both external and internal lesion placement in the two following scenarios: (i) calculating eq. (3.13) maintaining the same bandwidth of 0.5 GHz and varying the central frequency, and (ii) calculating eq. (3.13) increasing the bandwidth. Then, to evaluate the impact of the rotation angle of the transmitter for artefact removal, the procedure has been repeated using two transmitting positions displaced 5° (i.e., transmitting $\Delta\phi = 5°$) and using two transmitting positions displaced 10° (i.e., transmitting $\Delta\phi = 10°$).

5.6 Results and Discussions

As mentioned previously, the researchers in [16] performed a study for bone imaging, collecting the signals in multi-monostatic fashion, and using antennas immersed in a coupling liquid. In [16], imaging was performed using a beamforming procedure named non-coherent migration, after applying an average trace subtraction strategy to remove the artefact. Instead, here, we collect the signals in multi-bistatic fashion, using antennas in free space; imaging was performed using an HP-based algorithm, which operated in the frequency domain, after applying a rotation subtraction strategy to remove the artefact.

It may happen that artefact removal is not effective to fully cancel the artefact, in this case, the inclusion, i.e., the lesion, may become masked. This may be due to imperfect cancellation of the transmitting antenna or inappropriate cancellation of the first layers' reflection or even due to multiple reflections occurring inside the phantom that cannot cancel completely. Figs. 5.6 and 5.7 show all the images of the experimental phantom investigated in various frequencies and various bandwidths for bone marrow lesion and bone fracture scenarios, respectively. The correct position of the lesion is indicated by the arrow. The left columns refer to artefact removal performed using a transmitting step $\Delta\phi = 5^{\circ}$, while the right columns refer to artefact removal performed using a transmitting step $\Delta\phi = 10^{\circ}$.

It is important to point out that all the images shown here have been normalized and adjusted, forcing the intensity values below 0.5 to zero. However, S/C has been calculated before performing the image adjustment.

As Figs. 5.6(a), 5.6(b) and 5.7(a), 5.7(b) show, in the frequency range from 1 GHz to 1.5 GHz, the artefact masked the inclusion. When using the frequency range from 1.5 GHz to 2 GHz (see Figs. 5.6(c), 5.6(d) and 5.7(c), 5.7(d)) and from 2 GHz to 2.5 GHz (see Figs. 5.6(e), 5.6(f) and 5.7(e), 5.7(f)), only the lesion was visible, without any residual clutter. Images corresponding to a frequency range of 2.5 GHz to 3 GHz depicted that, although the lesion was detectable, the presence of residual clutters could not be ignored (see Figs. 5.6(g), 5.6(h) and 5.7(g), 5.7(h)).

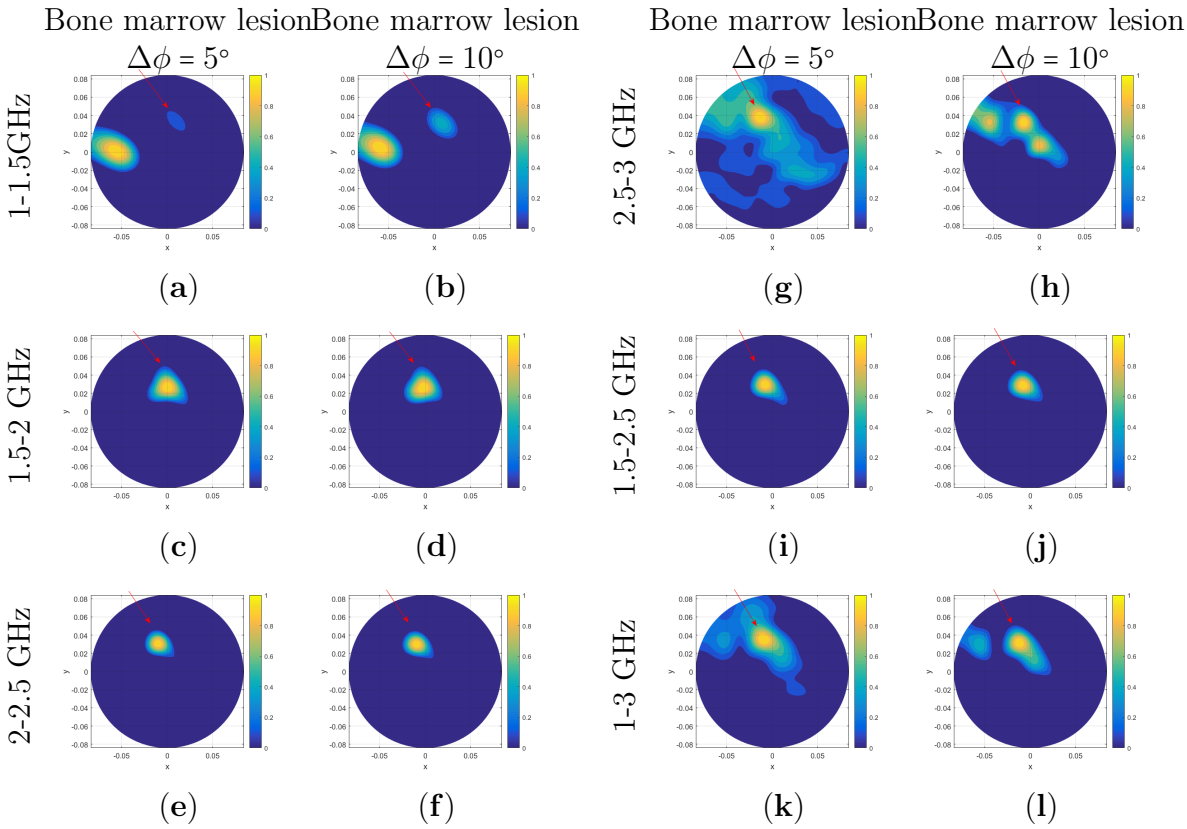

Figure 5.6: Microwave images of the bone marrow lesion employing various frequencies and bandwidths; (a,b), (c,d), (e,f) and (g,h) represent the resulting images when employing frequency ranges 1-1.5 GHz, 1.5-2 GHz, 2-2.5 GHz and 2.5-3 GHz, respectively, while (i,j) and (k,l) represent the images when considering bandwidths equal to 1 GHz and 2 GHz, respectively. Images are obtained following normalization to their correspondent maximum values and forcing to zero the intensity values below 0.5 (x and y are given in meters).

Table 5.3: Resolution (m) and S/C (linear) for bone marrow lesion.

Bone Marrow Lesion	$\Delta\phi$ = 5°		$\Delta\phi$ = 10°	
Freq. (GHz)	Resolution	S/C	Resolution	S/C
1-1.5	N/A	< 1	N/A	< 1
1.5-2	0.015	2.06	0.015	2.13
2-2.5	0.012	2.13	0.012	1.88
2.5-3	0.017	1.38	0.015	1.52

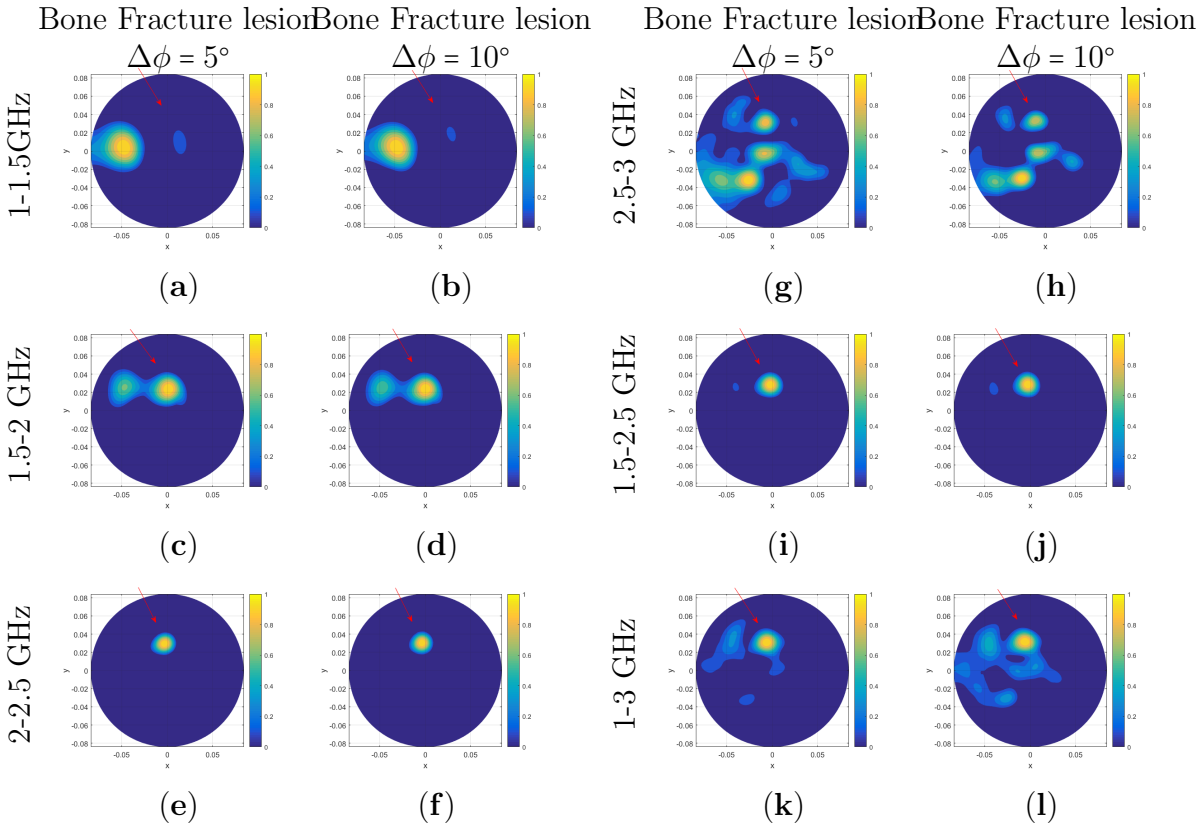

Figure 5.7: Microwave images of the bone fracture lesion employing various frequencies and bandwidths; (a,b), (c,d), (e,f) and (g,h) represent the resulting images when employing frequency ranges 1-1.5 GHz, 1.5-2 GHz, 2-2.5 GHz and 2.5-3 GHz, respectively, while (i,j) and (k,l) represent the images when considering bandwidth equal to 1 GHz and 2 GHz, respectively. Images are obtained following normalization to their correspondent maximum values and forcing to zero the intensity values below 0.5 (x and y are given in meters).

After visual inspection, image quantification has been performed calculating the resolution and S/C. Tables 5.3 and 5.4 summarise such parameters for bone marrow lesion and bone fracture lesion, respectively.

Concerning the bone marrow lesion, as Table 5.3 shows, the highest S/C values were

Table 5.4: Resolution (m) and S/C (linear) for bone fracture lesion.

Bone Fracture Lesion	$\Delta\phi$ = 5°		$\Delta\phi$ = 10°	
Freq. (GHz)	Resolution	S/C	Resolution	S/C
1-1.5	N/A	< 1	N/A	< 1
1.5-2	0.016	1.85	0.016	1.51
2-2.5	0.011	2.09	0.011	1.92
2.5-3	N/A	< 1	N/A	< 1

Table 5.5: Resolution (m) and S/C (linear) for various bandwidths for bone marrow lesion.

Bone Marrow Lesion	$\Delta\phi$ = 5°		$\Delta\phi$ = 10°	
Freq. (GHz)	Resolution	S/C	Resolution	S/C
1.5-2.5	0.013	2.22	0.014	2.06
1-3	0.018	1.49	0.015	1.34

related to the frequency range from 1.5 GHz to 2 GHz and from 2 GHz to 2.5 GHz. The same holds for the bone fracture scenarios as shown in Table 5.4. Concerning the resolution, resolutions of 1.2 cm and 1.1 cm have been achieved for the bone marrow lesion and bone fracture, respectively, when employing a frequency range from 2 GHz to 2.5 GHz. The result of operating frequency range from 2.5 GHz to 3 GHz showed that a further increase of the central frequency did not imply higher S/C and/or better resolution, since residual clutter may be enhanced.

Turning now to investigate the impact of increasing the bandwidth, S/C and resolution values have been calculated employing a frequency from 1.5 GHz to 2.5 GHz (i.e., a bandwidth of 1 GHz) and a frequency from 1 GHz to 3 GHz (i.e., a bandwidth of 2 GHz). As Tables 5.5 and 5.6 show, the highest S/C (2.22) corresponded to the bandwidth of 1 GHz compared to employing a bandwidth of 2 GHz (S/C = 1.49). It was evident that, although increasing the bandwidth of operation might be beneficial for S/C [126], such a bandwidth increase should be performed carefully to avoid including a region of frequency where residual clutter may be enhanced.

A further confirmation of such a finding may be drawn through a visual inspection of Figs. 5.6(i), 5.6(j) and 5.7(i), 5.7(j) and Figs. 5.6(k), 5.6(l) and 5.7(k), 5.7(l), which show the images employing the bandwidth of 1 and 2 GHz for both the bone marrow lesion and bone fracture, respectively.

Table 5.6: Resolution (m) and S/C (linear) for various bandwidths for bone fracture lesion.

Bone Fracture Lesion	$\Delta\phi$ = 5°		$\Delta\phi$ = 10°	
Freq. (GHz)	Resolution	S/C	Resolution	S/C
1.5-2.5	0.011	1.78	0.012	1.74
1-3	0.013	1.51	0.013	1.36

The highest value of S/C, which was equal to 2.22, was obtained through the HP procedure using a bandwidth of 1 GHz (1.5 GHz to 2.5 GHz). It should be emphasized that our obtained linear value of S/C 2.22 corresponded to 6.9 dB, which was in excellent agreement with [35] , [126]. According to Tables 5.3 and 5.4, the resolution that came from the experiments (1.1 cm) was in excellent agreement with the optical resolution limit of $\lambda_{1,f_{\max}}/4$, where $\lambda_{1,f_{\max}}$ represents the wavelength in the scenarios by considering a dielectric constant equal to the arithmetical average of the two layers calculated at the highest frequency of 3 GHz [35], [126].

Concerning the impact of the transmitter $\Delta\phi$ in artefact removal, we observed that for a large lesion size (radius = 0.7 cm), similar S/C values were obtained when using both $\Delta\phi$ = 5° and 10°. Instead, for a small lesion size (radius = 0.3 cm), S/C obtained when using $\Delta\phi$ = 5° was higher than that obtained for 10°. It is worthwhile pointing out that $\Delta\phi$ = 5° corresponded to a spatial displacement of 0.87 cm, while $\Delta\phi$ = 10° corresponded to a spatial displacement of 1.74 cm. Thus, we may conclude that optimal artefact removal was obtained with a transmitting $\Delta\phi$ = 5°, leading to a spatial displacement approximately of the same magnitude as the dimension of the lesion.

5.7 Summary/Conclusions

In this chapter, the extension of the MWI algorithm based on the HP to the multi-layered bone lesion phantom was performed.

This chapter presented the application of a new radar-based MWI procedure based on the HP approach, which achieved promising results for bone marrow lesion and bone fracture lesion detection.

We have fabricated a realistic multilayer phantom using dedicated recipes mimicking layers of cortical bone, bone marrow and lesion assumed as blood. Two scenarios were investigated, a large inclusion was placed within the marrow layer to represent the bone marrow lesion scenario and then, a small inclusion was placed in the cortical layer to represent the bone lesion or fracture scenarios.

The procedure was successfully tested inside an anechoic chamber on a dedicated multi-layer phantom in the frequency range of 1–3 GHz using one receiving and one transmitting antenna in free space. The identification of the lesion's presence in different bone layers was performed on images that were derived after processing through HP, the S21 signals measured inside an anechoic chamber in multi-bistatic fashion. Subtraction between S21 obtained using two transmitting positions was employed to remove the artefacts.

The impact of different frequencies and bandwidths (in the 1–3 GHz range) on lesion detection was investigated. The quantification of the microwave images was calculated using two parameters, which were the resolution and S/C. The findings showed that the frequency range of 1.5–2.5 GHz offered the best resolution (1.1 cm) and S/C (2.22 on a linear scale). A further bandwidth increase may lead to an enhancement of the residual clutter.

It should empathize that S21 is a measure of the total field; thus, detection can be achieved only after artefact removal, which can cancel the image of the transmitter and the reflection of the first layer. Together with the subtraction between S21 obtained using two slightly displaced transmitting positions, i.e., rotation subtraction, other techniques may be used for artefact removal, both in the frequency and in the time domain [151]. Among the techniques in the frequency domain, the rotation subtraction could be effective also for imaging highly asymmetric scenarios (such as human bones), since it assumes only the similarity of the first layer' reflection when displacing slightly the transmitting position.

Ultimately, this chapter verified that the microwave scanning procedure, which was based on HP, can be used to perform bone imaging to detect lesions and fractures in bone layers successfully, negating the use of X-rays. Our proposed scanning procedure was simple and required only two antennas in free space, thus no matching liquid was needed. This outcome of this part of the research may pave the way for the construction of a dedicated bone imaging system that is inexpensive, compact, and portable since it resorts to two rotating antennas coupled through a VNA.

The next chapter will see the extension of the HP algorithm for bone lesion detection into more realistic scenarios and through using a dedicated MammoWave imaging device to achieve the MWI system for bone lesion diagnostic imaging.

Chapter 6

The applicability of a HP-based Microwave Imaging Device for Bone Lesion Detection

6.1 Introduction

In the previous chapter, the applicability of the HP technique was investigated on the complex phantom consisting of different layers. The different sizes of inclusions were used to fabricate the bone marrow lesion and bone fracture lesion scenarios. The S21 signals were measured inside an anechoic chamber using bone lesion phantom in the frequency band of 1-3 GHz. All the presented measurement results validated the capability of the HP method is achieving promising results for bone marrow lesion and bone fracture lesion detection. The impact of different frequencies and bandwidths (in the 1–3 GHz range) on lesion detection was investigated. The quantification of the microwave images was also calculated using two parameters, which were the resolution and S/C. Consequently, the previous chapter verified that the microwave scanning procedure, which was based on HP, can be used to perform bone imaging to detect lesions and fractures in bone layers successfully.

Since the HP procedure was successful in bone lesion imaging using phantom measurements in an anechoic chamber, therefore this chapter aims to investigate the possibility of using MammoWave (a dedicated MWI device based on the HP procedure) for bone lesion imaging to detect the inclusion through phantom measurements. For evaluating the capability of the dedicated imaging device using a more realistic scenario, the proposed phantom was slightly modified as follows: i) we repeated the measurement replacing the cylindrically-shaped inclusion with an inclusion having a high-eccentric elliptical cross-section, i.e. flat-shaped, ii) we kept the cylindrically-shaped inclusion and replaced the external layer with the 90% glycerol and 10% water mixture.

Then the phantom experiments have been performed using a low complexity MWI device operating in free space in the 1-6.5 GHz frequency band. The portable MWI device, which operates in free space with two azimuthally-rotating antennas, measures the scattered signals in a multi-bistatic fashion, and employs the HP-based imaging procedure [100]. More in detail, the two antennas rotate all around the medium under test to collect the signals in a multi-bistatic fashion.

The purpose of this chapter is to investigate and quantify, the capability of this imaging device in detecting bone lesions through phantom experiments.

In this context, multi-layered phantoms simulating bone fracture or bone marrow lesion are realized, using millimetric cylindrically–shaped and also flat-shaped inclusions to emulate lesions. Artefact removal procedure will be applied using the rotation subtraction method [17]. Subsequently, a rigorous image quantification procedure will be implemented to assess the detection capability in two scenarios, i.e., bone fracture and bone marrow lesion.

This chapter is organized as follows. The experimental configuration, introducing the MammoWave MWI device, describing the bone lesion phantoms, imaging procedure and measurement, and imaging quantification are presented in the following section. Then all the experimental results will be illustrated in the next section. Afterward, the discussion of the image quantification and artefact removal method will be presented in more detail. The last section will be covered with a summary and conclusion.

6.2 Experimental Configuration

6.2.1 Microwave Imaging Device Description

The MWI device consists of an aluminium cylindrical hub containing two antennas, one transmitting (tx), and one receiving (rx). The hub is internally covered by microwave absorbers and is equipped with a hole with a cup, allowing the insertion of the object to be imaged. The antennas are installed at the same height, in free space, and can rotate around the azimuth to collect microwave signals from different angular positions. More details can be found in [100]. The tx and rx are connected to a 2-port VNA (S5065, Copper Mountain, Indianapolis, IN) which operates up to 6.5 GHz. Measurements have been performed by recording the complex S21 in a multi-bistatic fashion, i.e. for each transmitting position tx_m the receiving antenna is moved to measure the received signal every 4.5°, leading to a total of 80 receiving points rx_{np}. Concerning the transmitting positions, all the experiments have been done by employing 10 transmitting position, displaced in 5 doublets centred at 0°, 72°, 144°, 216°, and 288°. Figure 6.1 illustrates the setup configuration. As Fig. 6.1 shows, in each doublet, the two transmitting positions,

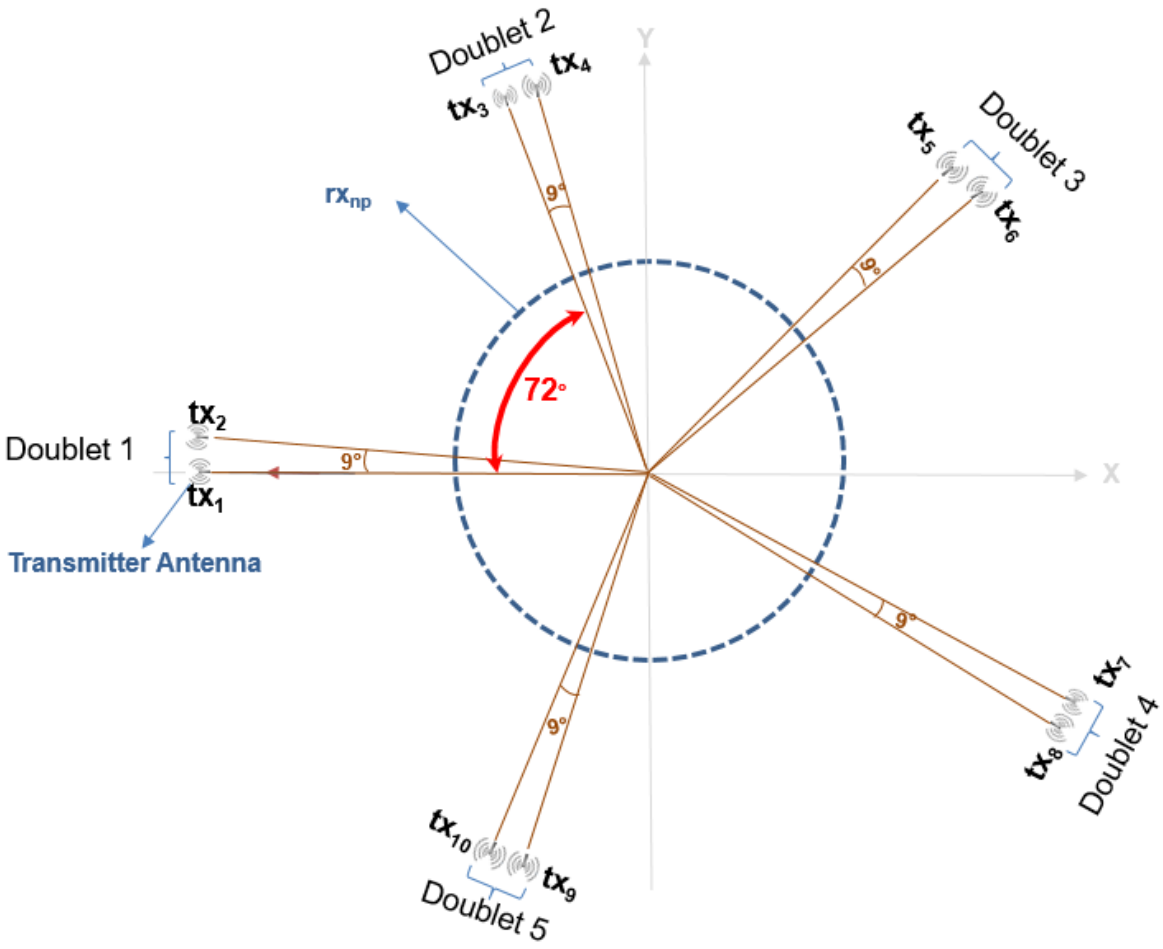

Figure 6.1: Pictorial view of the MWI device configuration.

are displaced by 9°. For each transmitting and receiving position, the complex S21 is collected from 1 to 6.5 GHz, with 5 MHz sampling. This frequency range can be considered appropriate for bone imaging [16], [17].

6.2.2 Phantom Descriptions

Two bone lesion phantoms comprising three layers have been fabricated. The three layers imitate: i) cortical bone (external layer); ii) bone marrow layer (internal layer); and iii) lesion. In the first phantom, which represents the bone fracture, the lesion has been placed between the external and internal layers, as shown in Fig. 6.2 (a). In the second phantom, which represents the bone marrow lesion, the lesion has been placed inside the internal layer, as shown Fig. 6.2(b). Dedicated liquids have been purchased from the ZMT Zurich MedTech Company [150] to emulate different layers of bone. The TLe11.5C.045 liquid oil has been employed to represent the external layer, which imitates the cortical bone layer. The internal layer, which emulates the bone marrow layer, has been fabricated by considering the Tle5C24 liquid oil. The lesion instead has been mimicked through

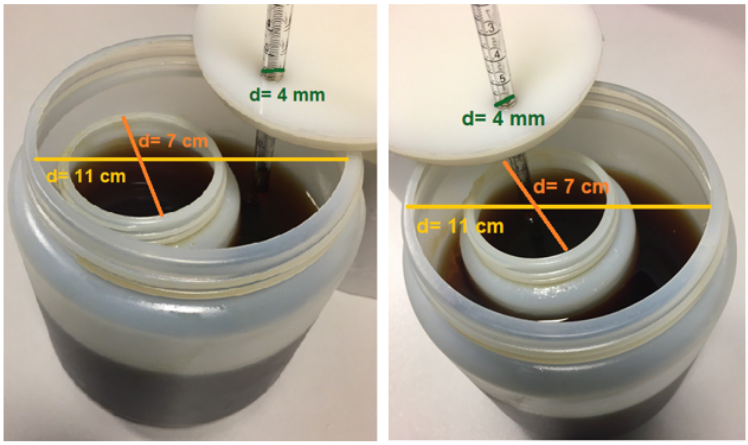

Figure 6.2: Fabricated phantoms for (a) bone fracture, and (b) bone marrow lesion.

Table 6.1: Relative permittivity and conductivity at 2 GHz.

	Relative permittivity	Conductivity (S/m)
Tle5C24 oil	5	0.2
TLe11.5C.045 oil	7	0.3
40% glycerol & 60% water mixture	60	2

a combination of 40% glycerol and 60% water [98]. The permittivity and conductivity values were calculated at 2 GHz for TLe11.5C.045, Tle5C24, and the combination of 40% glycerol and 60% water are given in Table 6.1. It should be highlighted that such dielectric properties can be considered representative of cortical bone, bone marrow, and a lesion constituted of blood [17].

Two different sizes of cylindrically shaped plastic containers with diameters of 11 cm and 7 cm have been considered to maintain the bone cortical and bone marrow equivalent materials, respectively. A cylindrically shaped tube with a diameter of 4 mm has been employed to contain an inclusion (see Fig. 6.2). The phantoms have been placed inside the cup of the MWI device as shown in Fig. 6.3 (a); in more details, the bone marrow lesion phantom has been positioned as shown in Fig. 6.3 (b) while the bone fracture lesion phantom has been located as shown in Fig. 6.3 (c). The cortical bone layer, bone marrow layer, and inclusion are presented in grey, light blue, and red respectively.

Additionally, two further scenarios have been considered, slightly modifying the bone marrow lesion phantom to be more realistic. First, we are keeping the same materials for the external and internal layers of phantoms and we replaced the cylindrically-shaped inclusion with an inclusion having a high-eccentric elliptical cross-section, i.e. flat-shaped (major axis 6 mm, minor axis 2 mm). After this, we are keeping the cylindrically-shaped

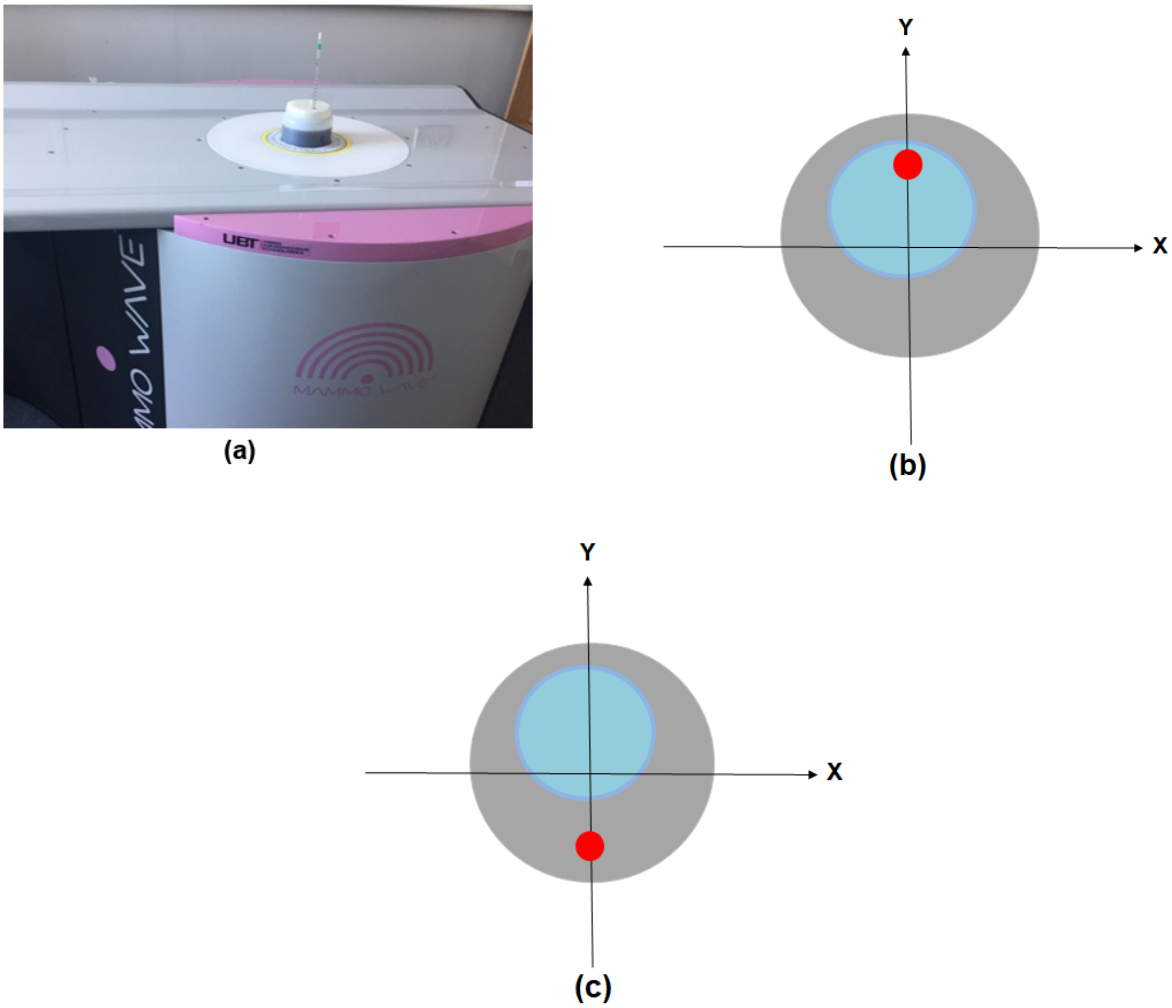

Figure 6.3: The MWI device, having an external diameter of 100 cm. Inside the cylindrical hub, there are the tx (Horn-type) and rx (Vivaldi-type) antennas, having Voltage Standing Wave Ratio < 3 in the band 1-6.5 GHz. Schematic view of bone marrow (b), and bone fracture lesion (c) measurement setups.

inclusion, and we replaced the TLe11.5C.045 with a combination of 90% glycerol and 10% water, having ε_r =16 and σ=1.1 S/m at 2 GHz [146]; such dielectric properties can be considered representative of a muscle and fat tissue [57]. Fig. 6.4 shows the bone lesion phantom using flat inclusion placed inside the MammoWave device.

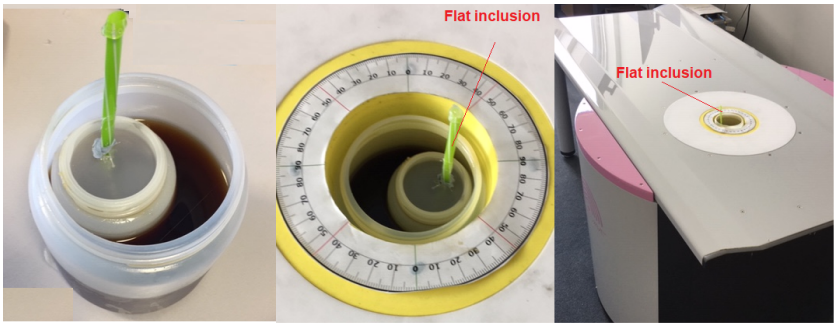

Figure 6.4: Phantom using flat inclusion placed inside the device.

6.2.3 Imaging Procedure

As extensively explained in chapter 3, the measured complex S21 has been processed through HP algorithm to generate the images [136] using MATLAB Software. The imaging algorithm and its block diagram are presented in the appendix.

However, the applied Huygens mathematical relations to reconstruct the field, and the intensity of final images, are briefly recounted here.

- Reconstructing the internal field using HP imaging procedure has been performed through subtraction between transmitting position m and transmitting position m+1, with m and m+1 belonging to the same doublet (eq. (3.9)).

$$\begin{aligned} &E^{\text{rcstr}}_{\text{HP,2D}}(\rho,\phi;\text{tx}_m-\text{tx}_{m+1};f) \\ &\propto \Delta s \sum_{np=1}^{N_{\text{PT}}} \left((\text{S21}^{\text{known}}_{np,\text{tx}_m} - \text{S21}^{\text{known}}_{np,\text{tx}_{m+1}}) G(k_1|\overrightarrow{\rho_{np}} - \overrightarrow{\rho}|) \right) \end{aligned} \tag{6.1}$$

- The intensity of the final images is given by the summation of different images corresponding to different transmitting doublets, which each one obtained through the non-coherent summation of all frequency contributions. Therefore, the combined image of 5 transmitting position doublets has been generated through (eq. (3.13)) while N_F is the number of frequencies:

$$
\begin{aligned}
I(\rho,\phi) &= \sum_{m=1}^{5} I(\rho,\phi;\mathrm{tx}_{2m-1}-\mathrm{tx}_{2m}) \\
&= \sum_{m=1}^{5}\sum_{i=1}^{N_F} |E^{\mathrm{rcstr}}_{\mathrm{HP,2D}}(\rho,\phi;\mathrm{tx}_{2m-1}-\mathrm{tx}_{2m};f_i)|^2
\end{aligned}
\tag{6.2}
$$

More details can be found in [100], [126], and [136]. However, it should be highlighted that all the abbreviations used within this formula have been extensively explained in chapter 3.

6.2.4 Imaging Quantification

To quantify the imaging algorithm's detection capabilities, we will again use the two metrics: i) resolution and ii) S/C.

6.3 Experimental Results

The experimentations have been executed by considering both the 5 individual transmitting position doublets, and the combination of 5 transmitting position doublets. All the obtained microwave images have been gathered in Figs. 6.5 and 6.6, exhibiting bone fracture lesion and bone marrow lesion, respectively. The images are obtained after employing the rotation subtraction between two doublet positions, functioning as an artefact removal procedure. The red arrows in the figures indicate the true location of the inclusion.

For both bone fracture lesion and bone marrow lesion, the images in Figs. 6.5(a) to 6.5(e) and 6.6(a) to 6.6(e) represent the results of employing individual transmitting position doublets after applying eq. (6.1) and obtaining the intensity images, whilst Figs. 6.5(f) and 6.6(f) represent the result of employing the combination of five transmitting position doublets, i.e. applying eq. (6.2).

Imaging performance has been investigated through image quantification. For this purpose, to evaluate the impact of transmitting positions in achieving detection, the resolution and S/C have been calculated for the obtained images of five individual transmitting position doublets and the combination of 5 transmitting position doublets. Results have been collected and summarised in Table 6.2 for both bone fracture and bone marrow lesions. It is worthwhile pointing out that S/C has been calculated before image adjustment performance.

In addition, Figs. 6.7(a) and 6.7(b) show the images obtained employing one single sample frequency, i.e., a single frequency contribution calculated for the central frequency (3.75 GHz), for bone fracture lesion and bone marrow lesion, respectively.

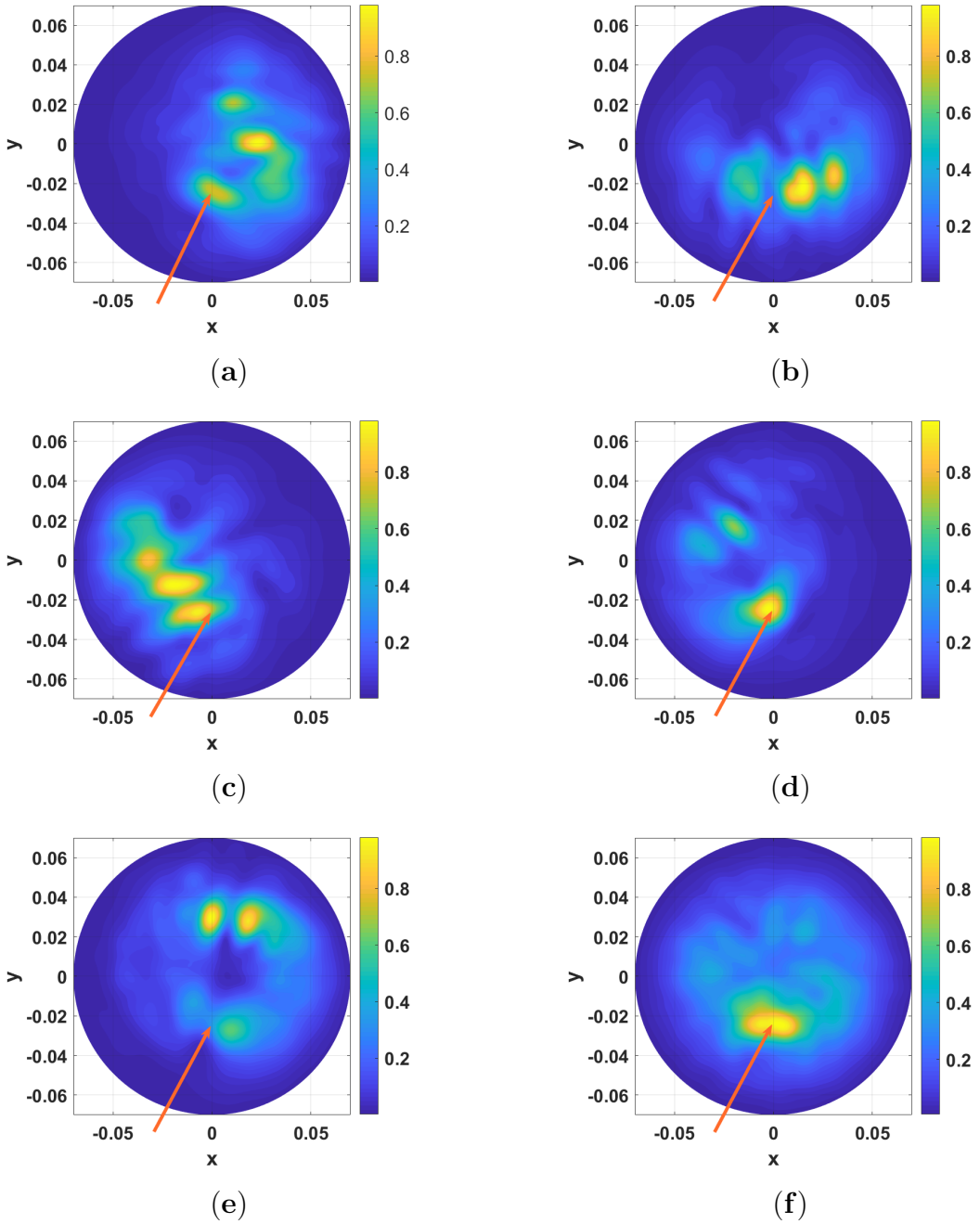

Figure 6.5: Microwave images of bone fracture lesion employing frequency 1-6.5 GHz. (a) to (f) represent the resulting images for first, second, third, fourth, fifth doublets and the combination of 5 transmitting position doublets, respectively.

Finally, Figs. 6.8 (a) and 6.8(b) show the images corresponding to the combination of 5 transmitting position doublets obtained for bone fracture lesion and bone marrow lesion phantom when using a flat-shaped inclusion, respectively. Moreover, Fig. 6.9 shows the image corresponding to the combination of 5 transmitting position doublets obtained in bone marrow lesion phantom when replacing the TLe11.5C.045 with a combination of 90% glycerol and 10% water, mimicking muscle and fat. All images of these two figures

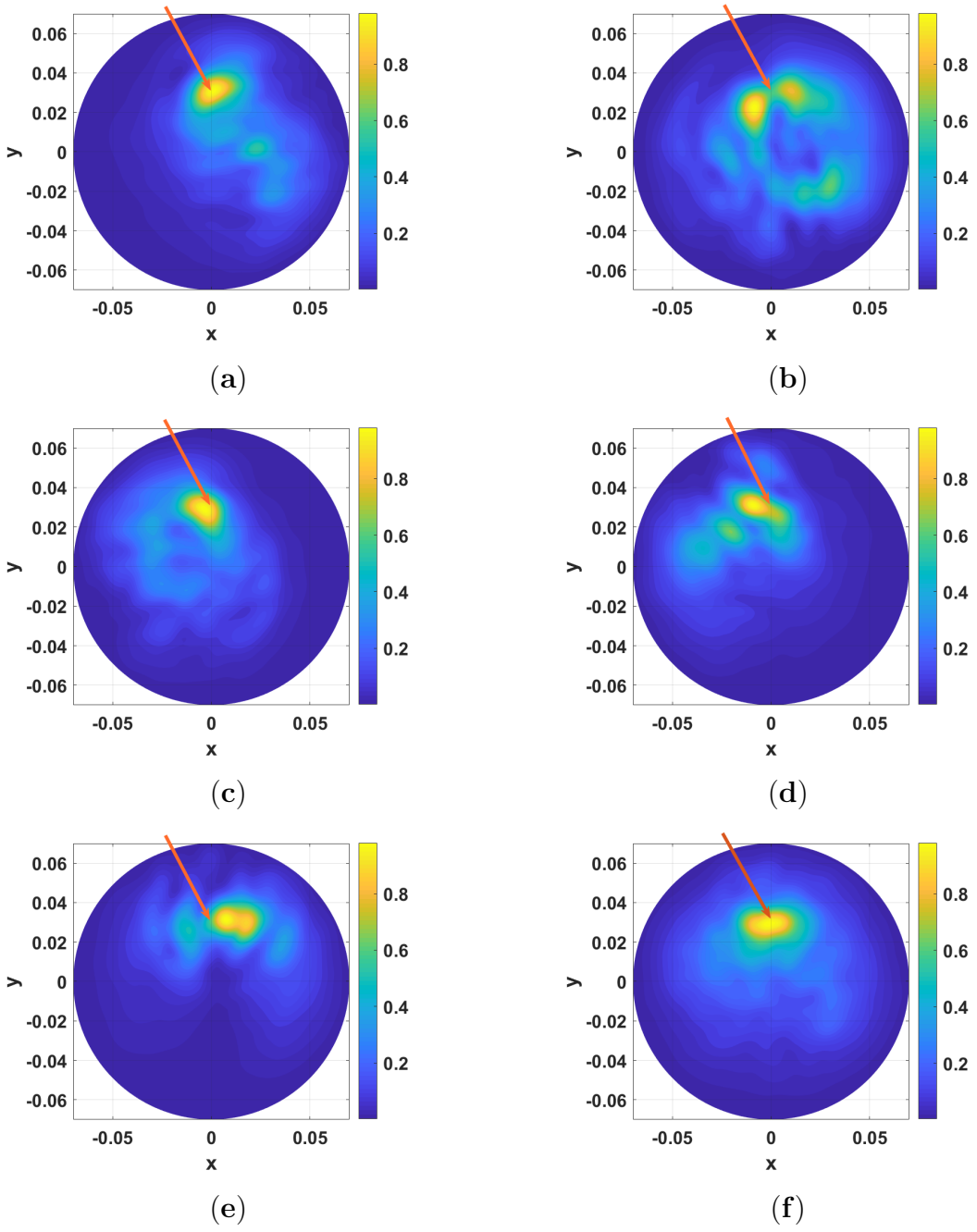

Figure 6.6: Microwave images of bone marrow lesion employing frequency 1-6.5 GHz. (a) to (f) represent the resulting images for first, second, third, fourth, fifth doublets and combination of 5 transmitting position doublets, respectively.

are the combination of 5 transmitting position doublets.

Table 6.2: Resolution (mm) and S/C (linear) for bone lesion.

	Bone fracture		Bone marrow	
Doublet No.	Resolution	S/C	Resolution	S/C
First doublet	N/A	< 1	7	1.8132
Second doublet	6	1.1585	6	1.5795
Third doublet	9	1.1822	6	2.5833
Fourth doublet	6	1.4751	6	1.5316
Fifth doublet	N/A	< 1	6	1.9960
Combining 5 doublets	5	2.2650	5	3.3512

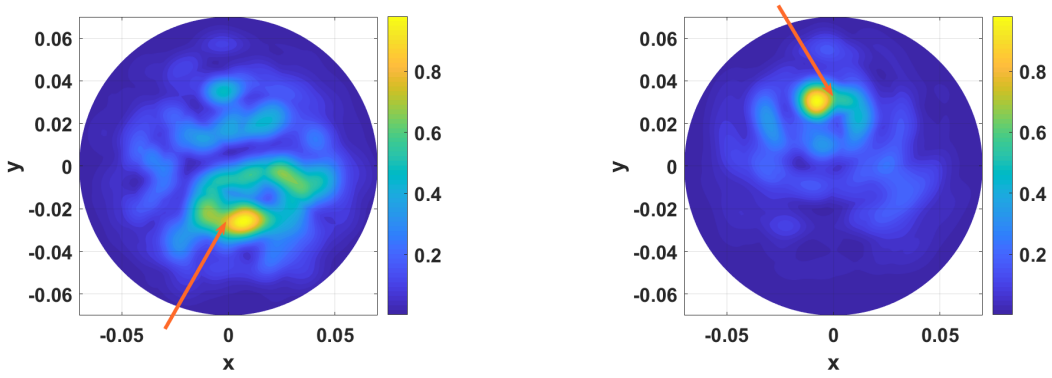

(a) (b)

Figure 6.7: Microwave images employing a central frequency of 3.75 GHz for: (a) bone fracture lesion, (b) bone marrow lesion.

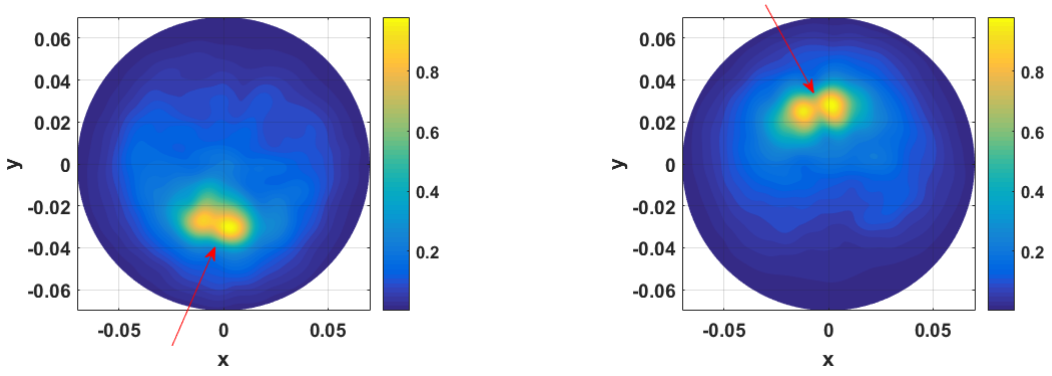

(a) (b)

Figure 6.8: Microwave images when using flat inclusion: (a) bone fracture lesion, (b) bone marrow lesion.

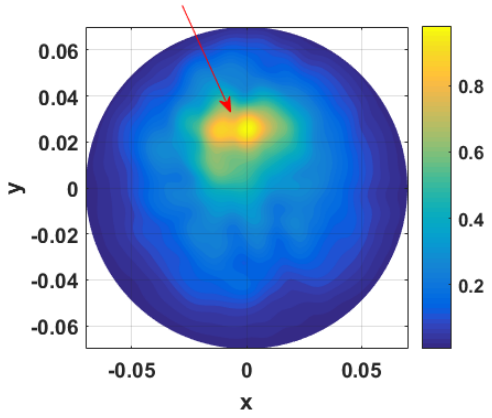

Figure 6.9: Microwave image of bone marrow lesion considering muscle as an external layer.

6.4 Discussion

To investigate the ability of the proposed MWI device to detect bone lesions, experiments have been performed using realistic phantoms with a very thin inclusion (diameter 4 mm), employing both individual transmitting positions doublets and their combination.

Rotation subtraction artefact removal has been employed to suppress artefacts, i.e. to reduce the clutter that could be the image of the transmitter and the reflections of the layers. However, it may happen that even beyond artefact removal, the residual clutter masks the inclusion. Residual clutter is due to the imperfect cancellation of the transmitting antenna or inappropriate cancellation of the first layer reflection or even due to multiple reflections occurring inside the phantom that cannot be cancelled completely.

For the bone fracture lesion, detection is achieved using second transmitting position doublet (Fig. 6.5(b)), third doublet (Fig. 6.5(c)) and fourth doublet (Fig. 6.5(d)). However, detection is not achieved using the first doublet (Fig. 6.5(a)) and fifth doublet (Fig. 6.5(e)), probably due to residual clutter. Detection is also achieved using the combination of 5 doublets (Fig. 6.5 (f)). For bone marrow lesion case, as Fig. 6.6 shows, detection has been successfully achieved in all individual transmitting position doublets and also using the combination of the five doublets.

Concerning image quantification (Table 6.2), in bone fracture lesion the S/C varies up to 1.47 by employing the individual doublets, while in the bone marrow lesion scenario S/C varies from 1.53 to 2.58 by employing the individual doublets. These values are in good agreement with those from anechoic chamber measurements [17], where a transmitting position doublet displaced at 5° or 10° has been employed. Furthermore, Table 6.2 shows that, when using the combination of 5 doublets, S/C increases up to 2.26 in bone fracture lesion and 3.35 in bone marrow lesion. It follows that the combination of 5 doublets can be very beneficial in term of S/C, a finding which is in agreement with previous

studies [35], [101], [126], and [136].

The higher values of S/C for bone marrow lesion to the bone fracture may be related to the existence of more residual clutter in fracture lesion scenario, as the fracture lesion scenario is more asymmetric. This is confirmed from Fig. 6.7, which refers to one single frequency contribution.

Concerning the resolution, according to the collected data in Table 6.2, using the combination of 5 doublets for both bone fracture and bone marrow lesion, we achieve the best resolution value equal to 5 mm. This is in excellent agreement with the optical resolution limit of $\lambda_{1,f_{\max}}/4$, where $\lambda_{1,f_{\max}}$ represents the wavelength when considering a dielectric constant equal to the arithmetical average of the two layers calculated at the highest frequency of 6.5 GHz [35], [126].

According to Figs. 6.8(a) and 6.8(b), the detection also can be achieved in the case of using flat-shaped inclusion for bone fracture lesion and bone marrow lesion, respectively. However, two spots appear in correspondence of the major axis extremities, the sharp edges in the images give a high intensity. This might suggest that lesions of 2 mm could be detected, even if they might appear, in the images, larger in size.

Turning now to investigate the impact of using 90% glycerol and 10% water for the external layer of bone lesion phantom to simulate the muscle and fat, Fig. 6.9 indicates the possibility of detection of the inclusion when a muscle and fat mimicking layer is employed as an external layer in the bone lesion phantom. However, the lower resolution is observed in comparison to the previous scenario.

Thus, Figs. 6.8 and 6.9 confirm that detection can be achieved also in more realistic phantoms, even if the S/C lower than that of Fig. 6.6(f) can be visually appreciated. However, a limitation of the investigation presented in this research is that we always used phantoms having a cylindrically shaped external layer. The next steps will be focused on the construction and use of anthropomorphic phantoms.

6.5 Summary/Conclusion

This chapter focused on expanding the MWI algorithm based on the HP for bone lesion detection using a dedicated MammoWave MWI device. The MammoWave device, initially manufactured for breast cancer detection, measures the scattered signals in a multi-bistatic fashion and employs an imaging procedure based on HP.

The validation of a free space operating MWI device based on the HP has been performed through phantom measurements. The multi-layered bone phantoms representing bone fracture and bone marrow lesion using millimetric cylindrically–shaped inclusions to emulate lesions have been improved by replacing the inclusion having a high-eccentric elliptical cross-section, i.e. flat-shaped (major axis 6 mm, minor axis 2 mm) instead of

cylindrically-shaped. Promising results have been obtained for bone lesion phantom in all scenarios.

Specifically, detection has been achieved in both bone fracture lesion and bone marrow lesion scenarios after applying the rotation subtraction artefact removal method using the superimposition of five doublet transmitting positions. The image quantification procedure has been implemented to assess the detection capability in two scenarios, i.e., bone fracture and bone marrow lesion. The quantification of the microwave images was calculated using the resolution and S/C parameters. Resolution of 5 mm and the S/C of 3.35 have been obtained by employing the combination of 5 transmitting position doublets in the imaging procedure and using a frequency band of 1-6.5 GHz. The achieved value of resolution (5 mm) and S/C (3.35 in linear scale) confirm the advantage of employing many transmitting positions on detection capability and the finding is in agreement with previous studies [35], [101], [126], and [136].

Bone lesion detection can also be achieved when using the combination of 90% glycerol and 10% water to mimic muscle and fat-equivalent material as an external layer of the bone lesion phantom. In fact, achieving the inclusion detection using the phantom having muscle and fat layer also confirmed the capability of the MWI device to detect the bone lesion.

Consequently, the MWI device is safe (no X-rays), portable, and has low complexity since it employs only two rotating antennas operating in free space coupled through a VNA. Therefore, the MammoWave MWI device may pave the way for the construction of an X-ray free bone lesion diagnostic device.

Chapter 7

Conclusion and Proposed Future Work

7.1 Conclusion

This thesis's contribution has been to MWI development presenting the proposed imaging algorithm for medical diagnostic applications including skin cancer detection, bone fracture lesion, and bone marrow lesion detection. The methodology used in this research, which is the MWI technique based on HP provides various advantages including simplicity, non-invasive technique, non-ionizing radiation, and also the capability of capturing the contrast or dielectric variation. Due to these features, HP has been the chosen method for investigation in this thesis. Going along this thesis, the extension of the HP method can be seen step by step for the investigation of skin cancer detection, bone fracture lesion, and bone marrow lesion detection.

First, the validation of the MWI based HP technique for skin cancer detection has been performed through simulation, modelling the human forearm phantom, and phantom measurements in an anechoic chamber using one transmitting and one receiving antenna placed in free space employing frequency range of 1-10 GHz. The multi-layered cylindrically-shaped human forearm phantom containing skin, adipose & muscle, cortical bone, and malignant layers (as an inclusion) has been designed and fabricated to simulate skin cancer. The combination of adipose & muscle has been considered here using a ratio of 50%-50%. Various recipes were tested for tissue-equivalent dielectric properties and the similarity of dielectric properties of each layer with the human tissue was addressed to finalise the recipes. It should be highlighted that the research of this thesis relies on the fact that there is a significant contrast between normal and malignant tissues. Detection of the tumour has been achieved in the generated images after applying HP-based imaging algorithm and artefacts removing procedure, i.e. the images of the transmitter, through employing a subtraction between S21 obtained using two sets of measurements.

Accordingly, the first part of this thesis verifies that HP can successfully be used to detect and locate a skin cancer type inclusion in a multilayer cylindrical phantom.

In addition, the possibility of HP-based MWI approach to detect the bone fracture lesion and bone marrow lesion has been investigated through designing and fabricating multilayer bone lesion phantoms and performing the phantom measurements in the anechoic chamber.

The bone lesion phantoms consisted of cortical bone, bone marrow, and the lesion layers. The lesion was placed once in the cortical bone layer and then inside the bone marrow layer to present both the bone fracture lesion and bone marrow lesion scenarios. Both phantoms were measured in the anechoic chamber using a frequency range of 1- 3 GHz using two antennas in free space. Promising results were achieved for both scenarios after applying the artefact removal method to remove the artefact by subtracting between S21 obtained using two transmitting positions. The findings illustrated the robustness of the HP procedure to detect the presence and location of inclusion in a multi-layered phantom. Subtraction between S21 obtained using two slightly displaced transmitting positions has been employed to remove the artefacts.

Moreover, to investigate the performance of the imaging, the analysing of the obtained images was performed through image quantification. For this purpose, to evaluate the impact of the various frequencies and bandwidths in achieving detection, the quantification of the images was performed by introducing two parameters, resolution, and S/C. The results of the image quantification specified the optimal frequency and optimal bandwidth for achieving lesion detection. Findings show that the frequency range of 1.5-2.5 GHz offers the best resolution (1.1 cm) and S/C (2.22 on a linear scale).

As mentioned previously, artefact removal is an essential procedure in the MWI system to allow achieving detection of the lesion inside the object. Since in this research, the rotation subtraction strategy was employed as an artefact removal method, the impact of the transmitter $\Delta\phi$ in removing the artefact has also been investigated. For this purpose, artefact removal using a transmitting step $\Delta\phi$ = 5° and $\Delta\phi$ = 10° have been tested in anechoic chamber measurements employing phantom having a large/small lesion. It has been observed that for large lesion size (radius = 0.7 cm), similar values of S/C were obtained when using both $\Delta\phi$ = 5° and $\Delta\phi$ = 10°. Instead, for a small lesion size (radius = 0.3 cm), higher S/C values were obtained when using $\Delta\phi$ = 5° rather than that obtained for $\Delta\phi$ = 10°. It should be noted that $\Delta\phi$ = 5° corresponded to a spatial displacement of 0.87 cm, while $\Delta\phi$ = 10° corresponded to a spatial displacement of 1.74 cm. It can be concluded that the optimal artefact removal was obtained when the spatial displacement was approximate of the same magnitude as the dimension of the lesion.

Accordingly, the result of performing experiments in the anechoic chamber verified the capability of the HP procedure for detecting the lesion inside the bone layers.

Afterward, the capability of the MammoWave MWI device based on the HP, initially used for breast cancer detection has been also investigated for bone lesion detection through phantom measurements. The development of modelling the bone lesion phantom was performed to gain more realistic scenarios employing MammoWave imaging device in the frequency range of 1-6.5 GHz. The phantom measurements have been performed on the cylindrical model containing the inclusion in various scenarios of bone fracture lesion and bone marrow lesion. To evaluate detection capability in a more realistic scenario, the measurement was repeated for the following scenarios; i) using the cylindrically-shaped inclusion (diameter 4 mm), ii) using an inclusion having a high-eccentric elliptical cross-section, i.e. flat-shaped (major axis 6 mm, minor axis 2 mm), and iii) replacing the muscle and fat layer in the external layer of the bone lesion phantoms. The measurements have been performed for both individual transmitting positions doublets and their combination.

The rotation subtraction artefact removal procedure has been applied to eliminate the images of the transmitting antenna or the reflection of different layers. The artefact removal has been performed with $\Delta\phi = 9^{\circ}$ when using MammoWave device for measurements (following what was done in the anechoic chamber) and follows that the lesion has been detected.

In addition, the image quantification has been performed through introducing the S/C and resolution parameters to evaluate the impact of transmitting positions in achieving detection. The findings show, in bone fracture lesion the S/C varies up to 1.47 by employing the individual doublets, while in the bone marrow lesion scenario S/C varies from 1.53 to 2.58 using the individual doublets. However, using the combination of 5 doublets leads to S/C increases up to 2.26 in bone fracture lesion and 3.35 in bone marrow lesion. Concerning the resolution, using the combination of 5 doublets for both bone fracture and bone marrow lesion, the best resolution value equal to 5 mm was achieved.

The S/C of 3.35 on a linear scale which has been obtained by employing the combination of 5 transmitting position doublets in the imaging procedure indicates that S/C using the MammoWave device, in general, is higher than the obtained S/C of the measurements in the anechoic chamber. It follows that the combination of 5 doublets is beneficial in term of S/C, a finding which is in agreement with previous studies [101], [126], and [136] confirms that S/C increases with employing the larger number of transmitting positions.

Consequently, the promising results indicate the ability of the MammoWave MWI device based on the HP procedure to detect the bone lesion in both bone fracture lesion and bone marrow lesion scenarios. Achieving the bone lesion detection in all different bone lesion scenarios including using cylindrically-shaped inclusion, using a flat inclusion, and replacing the muscle and fat layer in the external layer of the bone lesion phantoms, illustrate the capability of the MammoWave MWI device to detect the bone lesion.

Concerning the experimental duration, it should be pointed out that there is a balance

between the number of transmitting positions and the execution time. The experimental duration using the MammoWave device is approximately 10 minutes. This time depends on the number of transmitting positions, receiving positions, and frequency samples. For example, the time of measurements will be increased by increasing the transmitting positions, and it will be decreased by reducing the number of frequency samples. However, it should be noted that reducing the number of frequency sample may impact the S/C [136].

Ultimately, in this research, the effectiveness of the scanning procedure based on HP to perform bone imaging to detect the presence and location of the lesions and fractures in bone layers has been demonstrated. The outcomes of this thesis may pave the way for the construction of a dedicated bone imaging system that could be inexpensive, safe, portable, compact, and has low complexity employing only two rotating antennas operating in free space coupled through a VNA.

7.2 Future Work

The novel MWI technique based on HP, like other new techniques still has room for improvements in different aspects.

In the case of skin cancer detection, one of the aims for future research will be focused on the development of the skin phantom that would realise the different combinations of adipose & muscle, analysing the impact of the combined ratio in tumour detection. Moreover, investigating the capability of the MammoWave device to detect skin cancer using a more realistic phantom (after adapting the frequency range which can be used for high frequency) will be another step for future work.

A major change that is expected to be provided in the next step is to improve the artefact removal procedure that leads to having perfect cancellation of artefacts which can be caused by the transmitting antenna, first layers' reflection, or multi-reflection occurring inside the phantom. In addition, a comparison of the performances between rotation subtraction artefact removal and (local) average subtraction artefact removal is the desired point for the next work.

Furthermore, since the limitation of this research is that the used phantoms have a simple structure and are often cylindrical in shape for the external layer, the next steps will be focused on the extension of the HP method to geometries other than cylinders. Additionally, since, the limitation of this research is that the used phantoms are not anthropomorphic phantoms, the development of phantoms from multi-layer phantom to anthropomorphic phantom having the same structure as the human body in terms of shape, size, and materials are the scopes of future work.

Fabricating the anthropomorphic phantom is more complicated and should be performed by considering all the characterisations of the human body portion. For example,

the anthropomorphic phantom should be made of materials with a similar characterisation to human tissues. The characterisation of the human body portions such as hand limbs and leg parts does not remain constant with age particularly in terms of size, density, and shape (for instance, children's bones are smaller than adults' bones). For this reason, in fabricating the anthropomorphic phantoms, consideration of the difference between tissue characteristics in kids and adults or the difference between males and females is essential. Also, the impact of the age-related changes in bone geometry should be investigated because the body shape changes with age which varies for men and women. Finding the average values of thickness of the different substrates of body tissues in males and females also must be examined. Therefore, the study of how to generate the anthropomorphic phantom having similar characteristics to the human body is the next step.

However, since this research focuses on bone imaging using the MammoWave device, and according to the structure of this device, the future goal is to investigate the parameters related to the characteristics of human arm limbs, to construct the anthropomorphic phantom mimicking arm limbs. Since the anthropomorphic arm phantom should consist of skin, adipose, muscle, and bone layers, all the parameters related to the characteristics of the arm should be considered. The average will be different if we consider male and female or child and adult.

The anthropomorphic arm phantom will be constructed by having the required characteristics such as the thickness of each layer of the arm including skin, adipose, muscle, and bone layers (for example the average thickness of the adipose layer in the arm is 6.2 mm), the width of the arm (for example the average thickness of the arm for the child is 59.8 mm), and the dimension of the bone layer.

After determining the dimension and thickness of each layer, the 3D printing technology will be used to construct the 3D container to achieve the more realistic anthropomorphic arm phantom in terms of geometry, density, thickness, volume, and length. Then each layer of the 3D container will be filled with suitable materials mimicking the dielectric properties of real arm tissue.

Following the anthropomorphic arm, the lesion will be embedded inside it, and the set of anthropomorphic phantom experiments will be performed using the MammoWave device. The set of measurements will be performed using anthropomorphic arm phantom without lesion/fracture, and then the set of measurements will be performed using anthropomorphic arm phantom having a lesion/fracture. Once the successful results are obtained, the clinical trials will start. The clinical trials will be performed for both people without a fracture and people having fractures in arms.

Chapter 8

Appendix

In the following appendix, the proposed imaging software algorithm and the relevant code have been described. However, it should be highlighted that, since this work has been developed under industry part-funded, it is not possible to illustrate the entire code and process, since some parts of the code are confidential and cannot be fully presented.

8.1 Appendix I: Software/Algorithms

The frequency-domain measurements have been performed using one transmitting and one receiving antenna, connected to the VNA to record the S21 parameter which is the complex transfer function from the transmitting antenna to the receiving antenna.

MATLAB is a powerful programming language. Since it can be simply applied to manipulate the matrix, plot the function and data, and implement the algorithm, we used this software for image reconstruction procedure as follow:

Those measurement results have been saved as s2p files via VNA. The file has been loaded in MATLAB Software and extracted in the matrix in which contains the real part and the imaginary part of S21. After generating the matrix, the initial parameters have been defined such as defining the free-space parameter, defining the axis for plotting the internal field, and defining the grid that we want to place the reconstructing the internal field. Then the software used two separate loops for employing the different transmitting positions and different frequencies. Afterward, the HP reconstruction has been implemented (which is protected and not possible to show) and leads to generate the images.

8.2 Appendix II: Software Algorithm Block Diagram

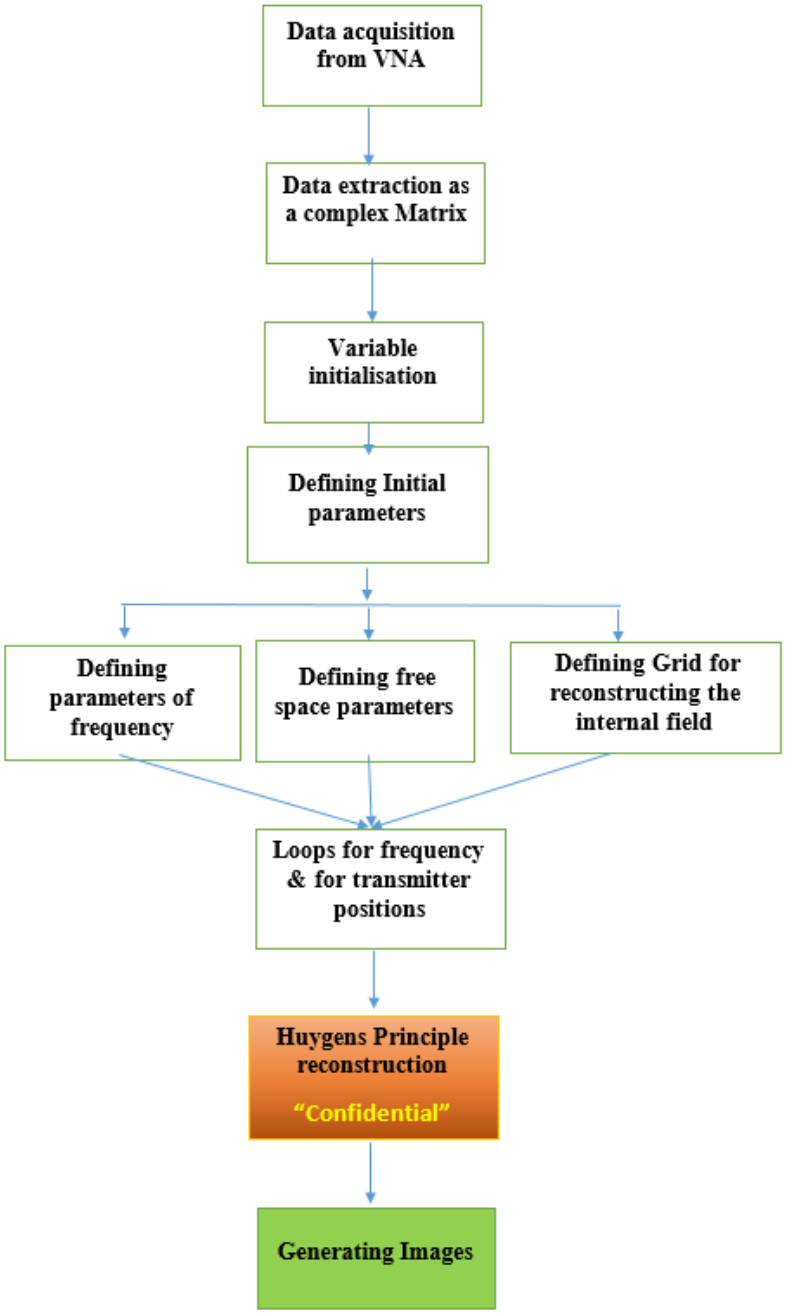

Figure 8.1: The block diagram of the applied Software imaging Algorithm.

8.3 Appendix III: Sample Code of Applied Imaging Algorithm

The measurement results have been saved as s2p files via VNA. The collected data have been processed through an imaging algorithm in MATLAB Software. Some parts of the code (as a sample) have been illustrated in the following steps:

1- Extracting the obtained data from VNA into the complex matrix.

This part of the code responsible to load the recorded data in the matrix, in which the first column represents the real part of S21 and the second column represents the imaginary part of S21. The matrix has been generated by this section (see Fig. 8.2).

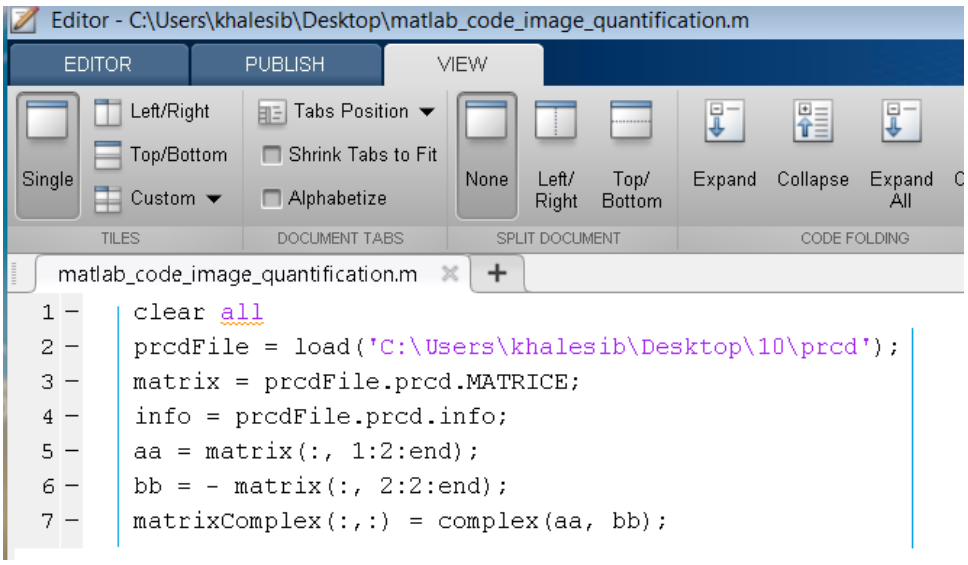

Figure 8.2: Loaded the recorded file via VNA in MATLAB.

2- Defining initial parameters such as ε_r, σ, and defining the grid of placing the reconstructing field (see Fig. 8.3).

3- Definition of the free-space and frequency parameters such as start frequency, stop frequency, frequency step, and etc. (see Fig. 8.4).

4- Defining the axis for plotting the internal field (see Fig. 8.5).

5- Definition of two loops for different transmitting positions in various frequencies (see Fig. 8.6).

6- Then the special code has been written relating to HP reconstruction which has been protected and is not possible to show.

7- Plotting the generated image (see Fig. 8.7).

```
er1=1;
ur1=1;
sigma1=0.2;

raggio0=0.07;
delta_phi=4.5*pi/180;   % phi step
phi_oss=[0:delta_phi:2*pi-delta_phi] ;
rho_oss=raggio0*ones(1,length(phi_oss))*1.0;

% defining grid where we want to reconstruct the  internal field
delta_phi_reconstr=pi/90;
delta_rho_reconstr=0.0005;
[phi_oss_reconstr,rho_oss_reconstr]= meshgrid(0:delta_phi_reconstr:2*pi,
```

Figure 8.3: Defining initial parameters.

```
% free-space
u0=4*pi*10^(-7);
e0=1/(36*pi)*10^-9;
Z0=120*pi;
c0=300000000;

% frequency
f_min=1.0*10^9
f_max=6.5*10^9
df_new=5*10^6;  % frequency step
new_ff=[f_min:df_new:f_max]';
NF=length(new_ff);
BB=df_new*NF;
```

Figure 8.4: Definition of the free-space and frequency parameters.

```
[X_reconstr,Y_reconstr] = pol2cart(phi_oss_reconst


simulated_reconstr_HuygensG_diff_OLD=zeros(NP_rho,
simulated_reconstr_HuygensG_diff_NEW=zeros(NP_rho,


newindex=1
```

Figure 8.5: Defining the axis for plotting the internal field.

```
for multisource_index= 1:3:13

    phi_note=phi_note_MULTISOURCE(multisource_index)
    phi_oss=-[phi_note:delta_phi:2*pi+phi_note] ;

for i=1:10:1100


            f=new_ff(i);
            e1=er1*e0*(1-j*sigma1/(2*pi*f*er1*e0));
            u1=ur1*u0;
            k1=sqrt((2*pi*f)^2*u1*e1);
            Z1=sqrt(u1/e1);
            lambda1=2*pi./real(k1);
            pen_depth=-1./imag(k1)

            for np=1:80
```

Figure 8.6: Definition two different loops for different transmitting positions in various frequencies.

```
%plot(2,1)
contourf(X_reconstr,Y_reconstr,(MAG_uwb_scatt_incoh_reconstr_diff_OLD_one.'
xlabel('x')
ylabel('y')
axis square
%title('magnitude- incoh reconstr- 2layer cyl  (eccentric) threshold=10 ')
colorbar
grid
%title('all freq, lstmag, multi triplets ,(k1)')
```

Figure 8.7: Generating the image.

It should be pointed out that, the investigation of the best ε_r, σ to optimise the imaging algorithm has been done through this research. Besides, the following codes which are responsible to do the image quantification ha been performed by this research to improve the HP imaging algorithm. Some parts of the image quantification code are demonstrated in Fig. 8.8:

```
totalIntesita_MAG_OLD_one=0;
for m=1:size(rho_oss_reconstr,1)
    for n=1:size(phi_oss_reconstr,2)
        totalIntesita_MAG_OLD_one=totalIntesita_MAG_OLD_one+MAG_uwb_scatt_incoh
    end
end
mediaIntesita=totalIntesita_MAG_OLD_one/(pi*raggio0^2)
MtoAVG_MAG_OLD_one=(max(max(abs(MAG_uwb_scatt_incoh_reconstr_diff_OLD_one))))/m

totalIntesita_MAG_NEW_one=0;
for m=1:size(rho_oss_reconstr,1)
    for n=1:size(phi_oss_reconstr,2)
        totalIntesita_MAG_NEW_one=totalIntesita_MAG_NEW_one+MAG_uwb_scatt_incoh
    end
end
mediaIntesita=totalIntesita_MAG_NEW_one/(pi*raggio0^2)
MtoAVG_MAG_NEW_one=(max(max(abs(MAG_uwb_scatt_incoh_reconstr_diff_NEW_one))))/m



    totalIntesita_PH_OLD_one=0;
for m=1:size(rho_oss_reconstr,1)
    for n=1:size(phi_oss_reconstr,2)
        totalIntesita_PH_OLD_one=totalIntesita_PH_OLD_one+PH_uwb_scatt_incoh_re
    end
end
```

Figure 8.8: Part1: Image quantification code.

```
MAX_phi_MAG_OLD_one=max(NEW_INTENSITY_HuygensG_MAG_OLD_one,[],1);
[MM,index] = max(MAX_phi_MAG_OLD_one)

%figure;plot(rho_oss_reconstr,NEW_INTENSITY_HuygensG)
%figure;plot(rho_oss_reconstr(:,12),NEW_INTENSITY_HuygensG(:,12))


figure;plot(rho_oss_reconstr(:,index),NEW_INTENSITY_HuygensG_MAG_(
title('magnitude k1')



INTENSITY_HuygensG_MAG_NEW_one=abs(MAG_uwb_scatt_incoh_reconstr_di
NEW_INTENSITY_HuygensG_MAG_NEW_one=imadjust(INTENSITY_HuygensG_MAG
figure,
```

Figure 8.9: Part2: Image quantification code.

```
contourf(X_reconstr,Y_reconstr,NEW_INTENSITY_Huygens
xlabel('x')
ylabel('y')
title('normalized intensity MAG  real k1(after image
colorbar
grid
axis square


MAX_phi_MAG_NEW_one=max(NEW_INTENSITY_HuygensG_MAG_N
[MM,index] = max(MAX_phi_MAG_NEW_one)

%figure;plot(rho_oss_reconstr,NEW_INTENSITY_HuygensG
%figure;plot(rho_oss_reconstr(:,12),NEW_INTENSITY_Hu
```

Figure 8.10: Part3: Image quantification code.

Bibliography

[1] P. Palmer and *et.al*, "Diagnostic imaging in the community, a manual for clinics and small hospital," in *Pan-American Health Organisation World Health Organisation*, 2012.

[2] W. H. O. T, "The World Health Organisation," in *Global Tuberculosis Report*, 2012.

[3] B. Bouhemad and *et.al*, "Clinical Review: Bedside Lung Ultrasound in Critical Care Practice," *Crit. Care*, vol. 11, no.1, pp. 205, 2007.

[4] N. Zasler and *et.al*, "Brain Injury Medicine: Principle and Practice," in *2nd Edition*, New York: NY:Demos Medical, 2013.

[5] T. A. Einhorn,"Enhancement of fracture-healing," in *Journal of Bone and Joint Surgery*, vol. 77, no. 6, pp. 940–956, 1995.

[6] M. Mercuri and *et.al*, "Radiation exposure from medical imaging: A silent harm," *CMAJ*, vol. 183, no. 4, pp. 413–414, 2011.

[7] D. W. Winters and *et.al*, "Estimation of the Frequency-Dependent Average Dielectric Properties of Breast Tissue Using a Time-Domain Inverse Scattering Technique," *IEEE Transactions on Antennas and Propagation*, vol. 54, no.11, pp. 3517-3528, Nov. 2006.

[8] C. G. Bilich, "Bio-Medical sensing using Ultra Wideband Communication and Radar Technology: A feasibility Study," *in Pervasive Health Conference and Workshops*, Innsbruck, Austria, Nov. 29 2006 - Dec. 1 2006, pp. 1-9.

[9] M. Lazebnik and *et.al*, "A large-scale study of the ultrawideband microwave dielectric properties of normal, benign and malignant breast tissues obtained from cancer surgeries," *Physics in Medicine and Biology*, vol. 52, no. 20, pp. 6093-6115, 2007.

[10] D. Andreuccetti and *et.al*, "An Internet resource for the calculation of the dielectric properties of body tissue in the frequency range 10 Hz -100 GHz," *IFAC-CNR*, Florence (Italy), 1997. [online]. Available: `http://niremf.ifac.cnr.it/tissprop/`. [Accessed Based on data published by C. Gabriel et al. in 1996].

[11] E. Porter and *et.al*, "An Early Clinical Study of Time-Domain Microwave Radar for Breast Health Monitoring," *IEEE Transactions on Biomedical Engineering*, vol. 63, no. 3, pp. 530-9, March 2016.

[12] L. Wang, "Multi-Frequency Holographic Microwave Imaging for Breast Lesion Detection," *IEEE Access*, vol. 7, pp. 83984-83993, June 2019.

[13] S. Y. Semenov and D. R. Corfield, "Microwave Tomography for Brain Imaging: Feasibility Assessment for Stroke Detection," *International Journal of Antennas and Propagation*, vol. 2008, pp. 1-8, April 2008.

[14] V. L. Coli and *et.al*, "Detection of Simulated Brain Strokes Using Microwave Tomography," *IEEE Jornal of Electromagnetics, RF and Microwaves in Medicine and Biology*, vol. 3 , no. 4, pp. 256-260, 2019.

[15] A. E. Stancombe and *et.al*, "Portable Microwave Head Imaging System using Software-defined Radio and Switching," *IEEE Journal of Electromagnetics, RF and Microwave in Medicine and Biology*, vol. 3, no. 4, pp. 284-291, 2019.

[16] G. Ruvio and *et.al*, "Microwave bone imaging: A preliminary scanning system for proof-of-concept," *IET Healthcare Technology Letters*, vol. 3, no. 3, pp. 218-221, Sep 2016.

[17] B. Khalesi and *et.al*, "A Phantom Investigation to Quantify Huygens Principle based Microwave Imaging for Bone Lesion Detection," *Electronics*, vol. 8, no. 12, pp. 1505 https://doi.org/10.3390/electronics8121505, 2019.

[18] C. K. Kuhl and *et.al*, "Mammography, Breast Ultrasound, and Magnetic Resonance Imaging for Surveillance of Women at High Familial Risk for Breast Cancer," *Jornal of Clinical Oncology*, vol. 23, no. 33, pp. 8469-8476, 2005.

[19] C. R. Hill and G. R. Ter-Harr, "Review Article: High Intensity Focused Ultrasound–Potential for Cancer Treatment," *British Journal of Radiology*, vol. 68, no. 816, pp. 1296-1303, Dec. 1995.

[20] "Memorial Hospital of Texaz Country", 20 Jun 2011. [Online]. Available: `http://www.mhtcguymon.org/`. [Accessed 2011].

[21] R. Guo and *et.al*, "Ultrasound imaging technologies for breast cancer detection and management: a review," *Ultrasound in medicine & biology*, vol. 44, no. 1 pp. 37-70, 2018.

[22] "Medical Device Managing, CT Scan", 3 February 2013. [Online]. Available: http://www.fda.gov/Radiation-EmittingProducts/RadiationEmittingProductsandProcedures/MedicalImaging/MedicalX-Rays/ucm115317.htm.

[23] D. L. Pham and *et.al*, "Current Methods in Medical Image Segmentation," *Annu. Rev. Biomed. Eng.*, vol. 2, pp. 315-37, 2000.

[24] R. F. Cotellesa and *et.al*, "Principle of Computerized Tomography," *IEEE Free Press*, 1987.

[25] "MRI Scan for Stroke Diagnose," 15 January 2012. [Online]. Available: http://www.radiologyinfo.org/content/mr_cardiac.htm.

[26] A. Abubakar and *et.al*, "Imaging of biomedical data using a multiplicative regularized contrast source inversion method," *IEEE Transactions on Microwave Theory and Techniques*, vol. 50, no. 7, pp. 1761-1771, 2002.

[27] P. M. Meaney and *et.al*, "A clinical prototype for active microwave imaging of the breast," *IEEE Transactions on Microwave Theory and Techniques*, vol. 48, no. 111, pp. 1841-1853, 2000.

[28] L. Jofre and *et.al*, "Medical imaging with a microwave tomographic scanner," *IEEE Transactions on Biomedical Engineering*, vol. 37, no. 3, pp. 303-312, March. 1990.

[29] S. Y. Semenov and *et.al*, "Microwave tomography: two-dimensional system for biological imaging," *IEEE Transactions on Biomedical Engineering*, vol. 43, no. 9, pp. 869-877, Sep. 1996.

[30] S. Y. Semenov and *et.al*, "Spatial resolution of microwave tomography for detection of myocardial ischemia and infarction-experimental study on two-dimensional models," *IEEE Transactions on Microwave Theory and Techniques*, vol. 48, no. 4, pp. 538-544, Apr. 2000.

[31] M. Jalilvand and *et.al*, "Quantitative imaging of numerically realistic human head model using microwave tomography," *Electronics Letters*, vol. 50, no. 4, pp. 255-256, Feb. 2014.

[32] A. H. Golnabi and *et.al*, "Tomographic Microwave Imaging With Incorporated Prior Spatial Information," *IEEE Transactions on Microwave Theory and Techniques*, vol. 61, no. 5, pp. 2129-2136, May. 2013.

[33] M. Pastorino and *et.al*, "Microwave imaging," *John Wiley & Sons*, vol. 208, 24 March 2010. Online ISBN:9780470602492 —DOI:10.1002/9780470602492, 2010.

[34] E. C. Fear and *et.al*, "Microwave System for Breast tumour Detection," *IEEE Microwave and Guided Wave Letters*, vol. 9, no. 11, pp. 470-472, 1999.

[35] E. C. Fear and *et.al*, "Confocal microwave imaging for breast cancer detection: localization of tumours in three dimensions," *IEEE Transactions on Biomedical Engineering*, vol. 49, no. 8, pp. 812-822, Aug. 2002.

[36] X. Li and S. C. Hagness, "A confocal microwave imaging algorithm for breast cancer detection," *IEEE Microwave and Wireless Components Letters*, vol. 11, no. 3, pp. 130-132, March. 2001.

[37] E. C. Fear and *et.al*, "Microwave Breast Imaging With a Monostatic Radar-Based System: A Study of Application to Patients," *IEEE Transactions on Microwave Theory and Techniques*, vol. 61, no. 5, pp. 2119-2128, May. 2013.

[38] R. Nilavalan and *et.al*, "Numerical investigation of breast tumour detection using multistatic radar," *Electronics Letters*, vol. 39, no. 25, pp. 1787-1789, Dec. 2003.

[39] E. J. Bond and *et.al*, "Microwave imaging via space-time beamforming for early detection of breast cancer," *IEEE Transactions on Antennas and Propagation*, vol. 51, no. 8, pp. 1690-1705, Aug. 2003.

[40] X. Li and *et.al*, "Microwave Imaging via Space Time Beamforming: Experimental Investigation of tumour Detection in Multilayer Breast Phantoms," *IEEE Transactions on Microwave Theory and Techniques*, vol. 52, no. 8, pp. 1856-1865, Aug. 2004.

[41] M. O'Halloran and *et.al*, "Quasi-Multistatic MIST Beamforming for the Early Detection of Breast Cancer," *IEEE Transactions on Biomedical Engineering*, vol. 57, no. 4, pp. 830-840, 2010.

[42] Y. Xie and *et.al*, "Multistatic Adaptive Microwave Imaging for Early Breast Cancer Detection," *IEEE Transactions on Biomedical Engineering*, vol. 53, no. 8, pp. 1647-1657, 2006.

[43] M. Klemm and *et.al*, "Radar-based breast cancer detection using a hemispherical antenna array–Experimental results," *IEEE Transactions on Antennas and Propagation*, vol. 57, no. 6, pp. 1692-1704, Jun. 2009.

[44] M. Klemm and *et.al*, "Microwave Radar-Based Differential Breast Cancer Imaging: Imaging in Homogeneous Breast Phantoms and Low Contrast Scenarios," *IEEE Transactions on Antennas and Propagation*, vol. 58, no. 7, pp. 2337-2334, Jul. 2010.

[45] D. Byrne and I. J. Craddock, "Microwave Time-Domain Wideband Adaptive Beamforming for Radar Breast Imaging," *IEEE Transactions on Antennas and Propagation*, vol. 63, no. 4, pp. 1725-1735, April. 2015.

[46] M. Persson and *et.al*, "Microwave-Based Stroke Diagnosis Making Global Prehospital Thrombolytic Treatment Possible," *IEEE Transactions on Biomedical Engineering*, vol. 61, no. 11, pp. 2806-2817, Nov. 2014.

[47] N. Ghavami and *et.al*, "Microwave Imaging Through a Mode-Matching Bessel Functions Procedure," *IEEE Transactions on Microwave Theory and Techniques*, vol. 61, no. 8, pp. 2753-2760, Aug. 2013.

[48] E. G. Fear and J. M. Sill, "Preliminary investigations of tissue sensing adaptive radar for breast tumour detection," *Proceedings of the 25th Annual International Conference of the IEEE Engineering in Medicine and Biology Society*, Cancun, Mexico, 17-21 Sept. 2003, vol. 4, pp. 3787-3790, 2003.

[49] C. M. Saunders and *et.al*,"Breast Cancer: The Facts," *Oxford Univertity Press*, 2009.

[50] G. M. Cooper, "Elements of Human Cancer," *The Jones & Bartlett Learning*, 1992

[51] R. M. Rangayyan and *et.al*,"Measures of acutance and shape for classification of breast tumours," *IEEE Transactions on Medical Imaging*, vol. 16, no. 6, pp. 799-810, 1997.

[52] Y. Chen and *et.al*,"Effect of lesion morphology on microwave signature in 2-D ultrawideband breast imaging," *IEEE Transactions on Biomedical Engineering*, vol. 55, no. 8, pp. 2011-2021, Aug 2008.

[53] J. M. Sill and E. C. Fear, "Tissue sensing adaptive radar for breast cancer detection—experimental investigation of simple tumour models," *IEEE Transactions on Microwave Theory and Techniques*, vol. 53, no. 11, pp. 312-3319, 2005.

[54] R. Benjamin and *et.al*, "Microwave detection of buried mines using non-contact, synthetic near-field focusing," *IEE Proceedings - Radar, Sonar and Navigation*, vol. 148, no. 4, pp. 233-240, 2001.

[55] Y. Huo and *et.al*, "Modeling of noninvasive microwave characterization of breast tumours," *IEEE Transactions on Biomedical Engineering*, vol. 51, no. 7, pp. 1089-1094, Jul 2004.

[56] W. T. Joines and *et.al*, "The Measured Electrical Properties of Normal and Malignant Human Tissues from 50 to 900 MHz," *Medical Physics*, vol. 21, no. 4, 1994.

[57] C. Gabriel and *et.al*, "The Dielectric Properties of Biological Tissues: I. Literature survey," *Physics in Medicine & Biology*, vol. 41, no. 11, pp. 2231-2249, 1996.

[58] A. M. Campbell and D. V. Land, "Dielectric Properties of Female Human Breast Tissue Measured In Vitro at 3.2 GHz," *Physics in Medicine & Biology*, vol. 37, no. 1, pp. 193-210, 1992.

[59] S. Gabriel and *et.al*, "The Dielectric Properties of Biological Tissues: II. Measurements in the Frequency Range 10 Hz to 20 GHz," *Physics in Medicine & Biology*, vol. 41, pp. 2251-2269, 1996.

[60] J. Jossinet and M. Schmitt, "A Review of Parameters for the Bioelectrical Characterization of Breast Tissue," *Annals of the New York Academy of Science*, vol. 873, pp. 30-41, 1999.

[61] S. S. Chaudhary and *et.al*, "Dielectric Properties of Normal and Malignant Human Breast Tissues at Radiowave and Microwave Frequencies," *Indian Journal of Biochemistry& Biophysics*, vol. 21, pp. 76-79, 1984.

[62] M. Lazebnik and *et.al*, "A Large-Scale Study of the Ultrawideband Microwave Dielectric Properties of Normal Breast Tissue Obtained from Reduction Surgeries," *Physics in Medicine and Biology*, vol. 52, no. 10, pp. 2637-2656, 2007.

[63] E. Pancera, "Medical applications of the Ultra Wideband technology," *in 2010 Loughborough Antennas and Propagation Conference (LAPC)*, Loughborough, UK , 8-9 Nov. 2010, pp. 52-56.

[64] Z. Wang and *et.al*, "Medical Applications of Microwave Imaging," *The Sceintific World Journal*, vol. 2014, Available `https://doi.org/10.1155/2014/147016`, pp. 7, 2014.

[65] L. Li and *et.al*, "Derivation and Discussion of the SAR Migration Algorithm Within Inverse Scattering Problem: Theoretical Analysis," *IEEE Transactions on Geoscience and Remote Sensing*, vol. 48, no. 1, pp. 415-422, 2010.

[66] Q. Fang, "Computational Methods for Microwave Medical Imaging," *PhD Thesis*, Dartmouth College Hanover, New Hampshire, 2004.

[67] S. V. Sree and *et.al*, "Breast imaging: A survey," *World journal of clinical oncology*, vol. 2, no. 4, pp. 171–178, 2011.

[68] D. Misra *et.al*, "Noninvasive electrical characterization of materials at microwave frequencies using an open ended coaxial line: Test of an improved calibration technique," *IEEE Transactions on Microwave Theory and Techniques*, vol. 38, pp. 8-14, 1990.

[69] A. Garton and D. V. Land, "Dielectric tissue measurements using a co-axial probe with a quarter-wave choke," *in IEE Colloquium on Application of Microwaves in Medicine*, London, UK, 28-28 Feb. 1995.

[70] G. N. Bindu and *et.al*, "Dielectric studies of corn syrup for applications in microwave breast imaging," *Progress In Electromagnetics Research*, vol. 59, pp. 175-186, 2006.

[71] C. Marchal and *et.al*, "Dielectric properties of gelatine phantoms used for simulations of biological tissues between 10 and 50 MHz ," *International journal of hyperthermia*, vol. 5, pp. 725-732, 1989.

[72] M. Robinson and *et.al*, "New materials for dielectric simulation of tissues," *Physics in medicine and biology*, vol. 36, pp. 1565, 1991.

[73] A.C. Society, "Cancer Facts & Figures," *Technical report*, 2004. Available: `http://www.pink-ribbon-pins.com/CancerRates2004.pdf`.

[74] A.C. Society, "Cancer Prevention & Early Detection Facts & Figures," *Technical report*, 2004. Available: `https://www.cancer.org/research/cancer-facts-statistics/cancer-prevention-early-detection.html`.

[75] A.C. Society, "Worldwide cancer statistics," *American Cancer Society*, 2018. Available: `https://www.cancer.org/content/dam/cancer-org/research/cancer-facts-and-statistics/breast-cancer-facts-and-figures/breast-cancer-facts-and-figures-2017-2018.pdf`.

[76] A.C. Society, "Breast Cancer What is breast cancer," *Tech. Report*, 2016. Available: `https://www.cancer.org/content/dam/CRC/PDF/Public/8577.00.pdf`.

[77] T. S. England and N. A. Sharples, "Dielectric Properties of the Human Body in the Microwave Region of the Spectrum," *Nature*, vol. 163, no. 4143, pp. 487-488, Mar. 1949.

[78] T. S. England, "Dielectric Properties of the Human Body for Wave-lengths in the 1–10 cm. Range," *Nature*, vol. 166, no. 4220, pp. 480-481, 1950.

[79] H. F. Cook, "The dielectric behaviour of some types of human tissues at microwave frequencies," *British Journal of Applied Physics*, vol. 2, no. 10, pp. 295-300, Oct 1951.

[80] L. Sha and *et.al*, "A review of dielectric properties of normal and malignant breast tissue," *Proceedings IEEE SoutheastCon*, Columbia, USA, 2002, pp. 457–462.

[81] A. J. Surowiec and *et.al*, "Dielectric Properties of Breast Carcinoma and the Surrounding Tissues," *IEEE Transactions on Biomedical Engineering*, vol. 35, no. 4, pp. 257–263, 1988.

[82] R. J. Halter and *et.al*, "The correlation of in vivo and ex vivo tissue dielectric properties to validate electromagnetic breast imaging: initial clinical experience," *Physiological Measurement*, vol. 30, no.6, 2009.

[83] A. Shahzad and *et.al*, "Investigation of the effect of dehydration on tissue dielectric properties in ex vivo measurements," *Biomedical Physics & Engineering Express*, vol. 3, no. 4, p. 045001, Jun 2017.

[84] O. Casas and *et.al*, "In vivo and in situ ischemic tissue characterization using electrical impedance spectroscopy," *Annals of the New York Academy of Sciences*, vol. 873, no. 1, pp. 51-58, 1999.

[85] D. Haemmerich and *et.al*, "Changes in electrical resistivity of swine liver after occlusion and postmortem," *Medical & Biological Engineering & Computing*, vol. 40, no. 1, pp. 29-33, 2002.

[86] P. M. Meaney and *et.al*, "Microwave open-ended coaxial dielectric probe: interpretation of the sensing volume re-visited," *BMC Medical Physics*, vol. 14, no. 1, pp. 3, 2014.

[87] T. Sugitani and *et.al*, "Complex permittivities of breast tumour tissues obtained from cancer surgeries," *Applied Physics Letters*, vol. 104, no. 25, pp. 1-6, 2014.

[88] L. E. Larsen and J. H. Jacobi, "A Microwave Phased Array System for Biological Target Interrogation," *in Medical Applications of Microwave Imaging*, New York, USA, IEEE Press, 1986.

[89] L. E. Larsen and J. H. Jacobi, "Microwave Interrogation of Dielectric Targets. Part I: By Scattering Parameters," *Medical physics*, vol. 5, no. 6, pp. 500–508, 1978.

[90] L. E. Larsen and J. H. Jacobi, "Microwave interrogation of dielectric targets. Part II: By microwave time delay spectroscopy," *Medical physics*, vol. 5, no. 6, pp. 509–513, 1978.

[91] L. E. Larsen and J. H. Jacobi, "Microwave Scattering Parameter Imagery of an Isolated Canine Kidney," *Medical physics*, vol. 6, no. 5, pp. 394, 1979.

[92] E. Fear and M. Stuchly, "Microwave detection of breast cancer," *IEEE Transactions on Microwave Theory and Techniques*, vol. 48, no. 11, pp. 1854-1863, 2000.

[93] W. C. Khor and M. E. Bialkowski, "Investigations into cylindrical and planar configurations of a microwave imaging system for breast cancer detection," *in 2006 IEEE Antennas and Propagation Society International Symposium*, Albuquerque , USA, 9-14 July, 2006, pp. 263-266.

[94] M. Bialkowski and Y. Wang, "UWB cylindrical microwave imaging system employing virtual array antenna concept for background effect removal," *Microwave and Optical Technology Letters*, vol. 53, pp. 1100-1104, 2011.

[95] A. A. Bakar and *et.al*, "Experimental Assessment of Microwave Diagnostic Tool for Ultra-Wideband Breast Cancer Detection," *Progress In Electromagnetics Research M*, vol. 23, no. DOI: 10.2528/PIERM11122102, 2012.

[96] J. Bourqui, and *et.al*, "A prototype system for measuring microwave frequency reflections from the breast," *International journal of biomedical imaging*, vol. 2012, DOI: 10.1155/2012/851234,2012.

[97] M. Omer and *et.al*, "Evaluating the impact of breast model complexity on microwave imaging signals," *in Proceedings of the 10th European Conference on Antennas and Propagation (EuCAP '16)*, Davos, Switzerland, April 2016, pp. 1-3.

[98] L. Sani and *et.al*, "Initial Clinical Validation of a Novel Microwave Apparatus for Testing Breast Integrity," *IEEE International Conference on Imaging Systems and Techniques*, Chania, Greece, 4-6 Oct. 2016. pp. 278-282.

[99] L. Sani and *et.al*, "Microwave apparatus for testing breast integrity based on Huygens principle: clinical validation on 16 subjects," *Loughborough Antennas & Propagation Conference (LAPC 2017)*, Loughborough, UK, 13-14 Nov. 2017.

[100] A.Vispa and *et.al*, "UWB device for breast microwave imaging: phantom and clinical validations," *Measurement*, vol. 146, pp. 582-589, 2019.

[101] L. Sani and *et.al*, "Novel microwave apparatus for breast lesions detection: Preliminary clinical results," *Biomedical Signal Processing and Control*, vol. 52, pp. 257-263, 2019.

[102] D. Ireland and M. Bialkowski, "Microwave head imaging for stroke detection," *Progress In Electromagnetics Research M*, vol. 21, pp. 163-175, 2011.

[103] H. Trefna and M. Persson, "Antenna array design for brain monitoring," *in 2008 IEEE Antennas and Propagation Society International Symposium*, San Diego, USA, 5-11 July, 2008.

[104] D. Ireland and M. Bialkowski, "Feasibility study on microwave stroke detection using a realistic phantom and the FDTD method," *in 2010 Asia-Pacific Microwave Conference*, Yokohama, Japan, 7-10 Dec, 2010, pp. 1-4.

[105] D. Andreuccetti and *et.al*, "Dielectric properties of body tissues in the frequency range 10 Hz–100 GHz," *Nello Carrara" Institute of Applied Physics 1*, 1997.

[106] H. Zhang and *et.al*, "A smart antenna array for brain cancer detection," *in 2011 Loughborough Antennas & Propagation Conference*, Loughborough, UK, 14-15 Nov, 2011, pp.1-4.

[107] M. Hopfer and *et.al*, "Electromagnetic tomography for detection, differentiation, and monitoring of brain stroke: A virtual data and human head phantom study," *IEEE Antennas and Propagation Magazine*, vol. 59, no.5, pp. 86-97, 2017.

[108] L. Bisio and *et.al*, "A numerical study concerning brain stroke detection by microwave imaging systems," *Multimedia Tools and Applications*, vol. 77, no. 8, pp. 9341-9363, 2018.

[109] A. T. Mobashsher and *et.al*, "On-site Rapid Diagnosis of Intracranial Hematoma using Portable Multi-slice Microwave Imaging System," *Scientific reports*, pp.37620, 2016. DOI:10.1038/srep37620.

[110] K. Chand and *et.al*, "Microwave reflectometry as a novel diagnostic method for detection of skin cancers," *in Instrumentation and Measurement*,Ottawa, Canada, 16-19 May, 2005, pp. 1425-1428.

[111] N. Ghavami and *et.al*, "Huygens Principle based UWB Microwave Imaging Method for Skin Cancer Detection," *Networks and Digital Signal Processing (CSNDSP)*, Prague , 20-22 July, 2016, pp.1-4.

[112] A. Taeb and *et.al*, "Millimetre-wave waveguide reflectometers for early detection of skin cancer," *IET Microwaves, Antennas& Propagation*, vol. 7, no. 14, pp. 1182-1186, 2013.

[113] A. Mirbeik-Sabzevari and *et.al*, "tumour Detection Using Millimeter-Wave Technology: Differentiating Between Benign Lesions and Cancer Tissues," *IEEE Microwave Magazine*, vol. 20, no. 8, pp. 30–43, 2019.

[114] S. I. Alekseev and M. C. Ziskin, "Human skin permittivity determined by millimeterwave reflection measurements," *Bioelectromagnetics*, vol. 28, no. 5, pp. 331-339, 2007.

[115] Y. Feldman and *et.al*, "The electromagnetic response of human skin in the millimetre and submillimetre wave range," *Physics in Medicine and Biology*, vol. 54, no. 11, pp. 3341-3363, 2009.

[116] J. Sierpowska and *et.al*, "Prediction of mechanical properties of human trabecular bone by electrical measurements," *Physiological measurement*, vol. 26, no. 2, p. 119, 2005.

[117] A.H.Golnabi and *et.al*, "Microwave tomography for bone imaging," *IEEE international symposium on Biomedical imaging: from nano to macro*, Chicago, IL, USA, 30 March-2 April, 2011, pp.956-959.

[118] J. Sierpowska and *et.al*, "Effect of human trabecular bone composition on its electrical properties," *Medical engineering& physics*, vol. 29, no. 8, pp. 845–852, 2007

[119] S. M. Salvador and *et.al*, "Microwave imaging of the knee: preliminary study," *Phys. Med. Biol*, 2008.

[120] S.M. Salvador and *et.al*, "Microwave imaging of the knee: On sensitivity, resolution and multiple tears detection," *2009 13th International Symposium on Antenna Technology and Applied Electromagnetics and the Canadian Radio Science Meeting. IEEE*, Toronto, ON, Canada, 15-18 Feb. 2009. DOI:10.1109/ANTEMURSI.2009.4805109

[121] S. M. Salvador and *et.al*, "Exploring joint tissues with microwave imaging," *IEEE Transactions on Microwave Theory and Techniques*, vol. 58, no. 6, pp. 2307–2313, 2010.

[122] Z. Tian, and *et.al*, "Microwave tomographic imaging for osteoporosis screening: a pilot clinical study," *In 2010 Annual International Conference of the IEEE Engineering in Medicine and Biology*, Buenos Aires, Argentina, 31 Aug.-4 Sept, 2010, pp.1218-1221.doi:10.1109/IEMBS.2010.5626442.

[123] P. M.Meaney and *et.al*, "Clinical microwave tomographic imaging of the calcaneus: A first-in-human case study of two subjects," *IEEE transactions on biomedical engineering*, vol. 59, no. 12, pp. 3304 - 3313, 2012.

[124] J. McCorkle, "Ultra wide bandwidth (UWB): gigabit wireless communications for battery operated consumer applications," *Digest of Technical Papers. 2005 Symposium on VLSI Circuits*, Kyoto, Japan, 16-18 June,2005. pp.6-9. DOI:10.1109/VLSIC.2005.1469321.

[125] K. Siwiak, "Ultra-wide band radio: introducing a new technology," *IEEE VTS 53rd Vehicular Technology Conference, Spring 2001. Proceedings (Cat. No.01CH37202)*, Rhodes, Greece, 6-9 May 2001, pp.1088-1093. DOI: 10.1109/VETECS.2001.944546

[126] N. Ghavami and *et.al*, "UWB microwave imaging of objects with canonical shape," *IEEE Transactionson Antennas and Propagation*, vol. 60, no. 1, pp. 231-239, 2012.

[127] J.Pan "Medical Applications of Ultra-Wideband (UWB)," *Medical Applications of Ultra-WideBand (UWB)*, 11 April 2018. Available: `https://www.cse.wustl.edu/~jain/cse574-08/ftp/uwb/`.

[128] S. Kwon and *et.al*, "Recent advances in microwave imaging for breast cancer detection," *International journal of biomedical imaging*, Oct. 2016. Available: `https://doi.org/10.1155/2016/5054912`.

[129] H. G. Schantz, "Bottom fed planar elliptical UWB antennas," *In IEEE Conference on Ultra Wideband Systems and Technologies*, Reston, VA, USA, 16-19 Nov. 2003, pp. 219-223. DOI: 10.1109/UWBST.2003.1267836

[130] H. G. Schantz, "Radiation efficiency of UWB antennas," *In IEEE Conference on Ultra Wideband Systems and Technologies (IEEE Cat. No. 02EX580)* , Baltimore, MD, USA, 21-23 May, 2002. pp. 351-355. DOI: 10.1109/UWBST.2002.1006392.

[131] Newsletter, "RF& Microwave Community," *EverythingRF*, Available online: `https://www.everythingrf.com/community/the-problem-of-testing-amplifiers-when-close-to-compression`.

[132] A. Vander Vorst and *et.al*,"RF/microwave interaction with biological tissues ," *New Jersey: John Wiley & Sons*, vol.181,2006, Available: `https://onlinelibrary.wiley.com/doi/book/10.1002/0471752053`.

[133] J. D. Kraus and *et.al*,"Antennas for all applications ," *In aaa. 2002*, Tata McGraw-Hill, New Delhi, 2003.

[134] C. A. Balanis,"Antenna theory: analysis and design ," *John wiley & sons*,2016 Feb 1.

[135] P. Enders, "Huygens principle as universal model of propagation," *Latin American Journal of Physics Education*, vol. 3, no. 1, pp. 19-32, Jan. 2009.

[136] G. Tiberi and *et.al*, "Ultrawideband microwave imaging of cylindrical objects with inclusions," *IET Microwaves, Antennas & Propagation*, vol. 5, no. 12, pp. 1440-1446, Sep. 2011.

[137] N. Ghavami and *et.al*, "Huygens principle based imaging of multilayered objects with inclusion," *Progress In Electromagnetics Research*, vol. 58, pp. 139-149, 2014.

[138] X. Li and *et.al*,"An overview of ultra-wideband microwave imaging viaspace-time beamforming for early-stage breast-cancer detection," *IEEE Antennas and Propagation Magazine*, vol. 47, no. 1, pp. 19-34, 2005.

[139] G. Tiberi and *et.al*, "A mode matching-Bessel functions based approach for UWB microwave imaging," *in 2010 IEEE Antennas and Propagation Society International Symposium*, Toronto, Canada, 11-17 July, 2010, pp. 1-4.

[140] Skin cancer Foundation (2020, April, 16), "Skin cancer information, Cancer Facts & Statistics," `https://www.skincancer.org/skin-cancer-information/skin-cancer-facts/`.

[141] N. Ghavami and *et.al*, "Huygens Principle-based approach for UWB medical imaging," *in 2011 8th European Radar Conference*, Manchester, UK, 12-14 Oct, 2011, pp. 369-372.

[142] E. M. Staderini, "UWB radars in medicine," *IEEE Aerospace and Electronic Systems Magazine*, vol. 17, no. 1, pp. 13-18, Jan. 2002.

[143] A. Sani and *et.al*, "Antennas and Propagation of Implanted RFIDs for Pervasive-Healthcare Applications," *Proceedings of the IEEE*, vol. 98, no. 9, pp. 1648-1655, Sep. 2010.

[144] S. Symeonidis and *et.al*, "Design and characterization of a three material anatomical bone phantom for implanted antenna applications," *in Loughborough Antennas & Propagation Conference (LAPC 2017)*, Loughborough, UK, 13-14 Nov, 2017, pp.1-5.

[145] R. E. Imhorf and P. Xiao, "Biox Epsilon - A New Permittivity Imaging System," *in Workshop Presentation, ISBS World Congress*, Copenhagen, 2012.

[146] P. M. Meaney and *et.al*, "Electrical Characterization of Glycerin: Water Mixtures: Implications for Use as a Coupling Medium in Microwave Tomography," *IEEE Transactions on Microwave Theory and Techniques*, vol. 65, no. 2, pp. 1471-1478, May 2017.

[147] A. Oryan and *et.al*, "Bone Injury and Fracture Healing Biology," *Elsevier Biomedical and environmental sciences*, vol. 28, no. 1, pp. 57-71, 2015.

[148] P. M. Meaney and *et.al*, "Microwave bone imaging," *in Proceedings of 6th European Conferenceon Antennas and Propagation (EUCAP)*, Prague, CzechRepublic, 26-30 March, 2012, pp. 1770-1771.

[149] A. Al. Nahid and *et.al*, "Hardware Implementation of Bone Fracture Detector Using Fuzzy Method Along with Local Normalization Technique," *Annals of Data Science*, vol. 4, no. 4, pp. 533–546, 2017.

[150] Z. M. Tech, "Zurich med tech," [Online]. Available: `https://zmt.swiss/validation-hw/tsm/tle5c-24-2450/` [Accessed 26 October 2019].

[151] M. A. Elahi and *et.al*, "Artifact Removal Algorithms for Microwave Imaging of the Breast," *Progress In Electromagnetics Research*, vol. 141, pp. 185-200, 2013.